THERMODYNAMIC AND TRANSPORT PROPERTIES OF SELF-ASSEMBLED MONOLAYERS FROM MOLECULAR SIMULATIONS

A Dissertation

by

TURKAN AYDOGMUS

Submitted to the Office of Graduate Studies of
Texas A&M University
in partial fulfillment of the requirements for the degree of

DOCTOR OF PHILOSOPHY

December 2004

Major Subject: Chemical Engineering

THERMODYNAMIC AND TRANSPORT PROPERTIES

OF SELF-ASSEMBLED MONOLAYERS

FROM MOLECULAR SIMULATIONS

A Dissertation

by

TURKAN AYDOGMUS

Submitted to Texas A&M University
in partial fulfillment of the requirements
for the degree of

DOCTOR OF PHILOSOPHY

Approved as to style and content by:

David M. Ford (Chair of Committee)	M. Sam Mannan (Member)
Kenneth R. Hall (Member)	Eric E. Simanek (Member)

Kenneth R. Hall
(Head of Department)

December 2004

Major Subject: Chemical Engineering

ABSTRACT

Thermodynamic and Transport Properties of Self-Assembled Monolayers from Molecular Simulations. (December 2004)

Turkan Aydogmus, B.S., Gazi University, Ankara Turkey

Chair of Advisory Committee: Dr. David M. Ford

The purpose of the work is to employ molecular simulation to further extend the understanding of Self-Assembled Monolayers (SAMs), especially as it relates to three particular applications: organic-inorganic composite membranes, surface treatments in Micro-Electro-Mechanical Systems (MEMS) and organic-surface-modified Ordered Mesoporous Materials (OMMs).

The first focus area for the work is the use of SAMS in organic-inorganic composite membranes for gas separations. These composite membranes, recently proposed in the literature, are based on the chemical derivatization of porous inorganic surfaces with organic oligomers. Our simulations achieve good qualitative agreement with experiment in several respects, including the improvement in the overall selectivity of the membrane and decrease in the permeance when increasing the chain length. The best improvement in the overall solubility selectivity is reached when the chains span throughout the pore.

The second application focus is on the use of SAMs as coatings in MEMS devices. The work focuses on the modeling of adhesion issues for SAM coatings at the

molecular level. It is shown that as the chain length is increased from 4 to 18 carbon atoms, the adhesion forces between two monolayers at the same separations decreases.

The third application focus is on the use of SAMs for tailoring surface and structural properties of OMMs, in particular, porous silicas. A molecular study of structural and surface properties of a silica material with a 5 nm pore size, modified via chemical bonding of organosilanes with a range of sizes (C4, C8 and C18) is presented. Grand canonical MC simulations are employed to obtain nitrogen adsorption isotherms for unmodified and modified MCM-41 material models. Furthermore, the density profiles of alkyl chains and nitrogen molecules are analyzed to clarify the differences in the adsorption mechanisms in unmodified and modified materials. The position of the capillary condensation steps gradually shifted to lower pressure values with the increase in size of the bonded ligands, and this shift was accompanied by a gradual disappearance of the hysteresis loop. As the length of the bonded ligands is increased, a systematic decrease in the pore diameter is observed and the multi-layer adsorption mechanism in modified model materials diminishes.

ACKNOWLEDGMENTS

I would like to express my deepest respect and gratitude to Dr. David M. Ford, my advisor, for conceiving my project. His guidance and support will always be appreciated. I would also like to thank Dr. Daniel F. Shantz, Dr. Eric E. Simanek and Dr. Kenneth R. Hall for serving as committee members. I am especially grateful to Dr. M. Sam Mannan not only for serving as a committee member but also for his advice, guidance and support during the course of my Ph.D. experience at Texas A&M University.

I am also grateful to my former colleague and mentor, Premkumar S. Rallabandi, for the technical help and discussions in the initial phase of research. Furthermore, I would like to acknowledge the departmental staff: Towanna Hubacek, Ninette Portales and Missy Newton for their kindness and all their help. Much appreciation goes to Jeff Polasek for helping me to maintain the computers.

I owe a special gratitude to my mother, husband, brother and sister who always believed in me and supported me all the way. Especially my mother, Hatice Aydogmus, who was always there for me in my tough days with her prayers, special love and care. My husband, Gabe Jan Haarsma, gave me strength with his encouragement and patience. They all have been a source of inspiration for me.

I would like to extend my gratitude to my roommate, Burak Ozturk, for his genuine friendship and support. He has been always accommodating and kind in my difficult times in College Station.

TABLE OF CONTENTS

Page

CHAPTER Page

CHAPTER Page

LIST OF FIGURES

FIGURE Page

FIGURE Page

FIGURE Page

LIST OF TABLES

CHAPTER I

INTRODUCTION

Coatings of organic molecules, especially self-assembled monolayers (SAMs), offer a means to alter and control the chemical nature of surfaces. SAMs are currently employed in organic-inorganic composite membranes for gas separations[1-3], packings for reversed-phase liquid chromatography[4-7], surfaces of micro-electro-mechanical systems (MEMS)[8-10] and Ordered Mesoporous Materials (OMMs) such as MCM-41[11-15], to list just a few examples. The novel properties conferred upon the surface arise from the nanometer-level structure, dynamics, and energetics of the tethered organic layer. Much experimental work has been carried out to gain an understanding of the link between the nanoscale characteristics of a surface film and its macroscopic behavior.[12,13,16-26]

The purpose of the work is to employ molecular simulation to further extend the understanding of SAMs, especially as it relates to three particular applications: organic-inorganic composite membranes, surface treatments of MEMS and OMMs. Molecular simulation has the advantage of following a model system in complete atomic-level detail, in addition to predicting a set of macroscopic observables that may be compared with experiments. Furthermore, the model system may be easily and systematically varied to isolate and examine certain hypotheses. The first focus area for the work is the use of SAMS in organic-inorganic composite membranes for gas separations. Javiad et al.[1] recently proposed this type of membrane for a class of separations in which a dilute

---

This dissertation follows the style of the Journal of Physical Chemistry B.

species of higher molecular weight must be removed from a light gas stream; examples include the removal of volatile organic compounds from air and the removal of higher molecular weight alkanes from natural gas. The membranes of Javaid et al.[1] were based on microporous (2-10 nm) ceramic substrates that were surface-derivatized with organic oligomers, and they provided relatively high selectivities for heavier alkane gas species. Furthermore, their separation properties could be tuned by varying the organic group and pore size employed. However, the molecular-level reasons for the observed changes in separation behavior remain unclear. We provided a molecular simulation study to advance the engineering of these organic-inorganic composite membranes.

The second application focus is on the use of SAMs as coatings in MEMS devices. MEMS principles allow the development of highly compact, smart products by augmenting the computational ability of microelectronics with the perception and control capabilities of microsensors and microactuators.[27-29] However, adhesion, friction, and wear are major problems limiting both the production yield and useful lifetime. SAM surface coatings[8-10,23-25,29-37] are typically used to ameliorate these problems, although determining the best molecular species for the SAMs is a difficult problem, due to the small length and time scales involved. In particular, our work focuses on the modeling of adhesion issues for SAM coatings at the molecular level. The results link macroscopic observations of coating performance with the molecular-level behavior of the organic layers, thus allowing for a rational design of improved SAM molecules.

The last focus area of the work is on the use of SAMs to improve the surface properties of OMMs. Porous silicas, especially the M41S family (MCM-41, MCM-48,

MCM-50 etc.) of silicas and alimunasilicas, are extensively used in many areas of science and technology as adsorbents, catalyst supports, additives, and chromatographic packings.[38-40] Including their high surface area, pore size, high mechanical, thermal and chemical stability[41], their surface reactivity toward organic ligands makes it possible to obtain a broad range of materials with improved mechanical and chemical stability; tailored particle size, pore size, and surface area; and the desired functionality and surface properties that are useful for various applications[39,40], such as the removal of heavy metal ions from water[42,43]. The characterization techniques, which provide detailed, accurate and reliable information about the structure, have great importance on the development of these materials. The aim of the work is to provide some molecular insight to the characterization of unmodified and organic-modified OMMs by using molecular simulations. Nitrogen adsorption measurements from the simulations are shown to be a convenient tool for characterization of both structural and surface properties of OMMs.

CHAPTER II

BACKGROUND

The object of this chapter is to introduce Self-Assembled Monolayers (SAMs) and their applications which are subject to our studies. The first section of this chapter contains a general introduction to SAMs, and the rest of the sections provide background on three particular applications of SAMs: Solubility-based organic-inorganic composite membranes for gas separations, SAM coatings on Micro-Electro-Mechanical System (MEMS) surfaces and organic surface-modified Ordered Mesoporous Materials (OMMs) as catalyst, adsorbents, etc., respectively.

In the first application, the effects of pore size, chain length and surface density on the membrane performance are investigated. In MEMS, the effect of self-assembled monolayer (SAM) chain length on the adhesion problems is studied. In our studies for the last application, it is aimed to gain better molecular understanding for the characterization of organic surface-modified OMMs.

2.1 Self-Assembled Monolayers (SAMs)

For our purposes, a SAM is defined as a thin layer of organic molecules on a suitable inorganic surface. Self-assembled monolayers can be prepared by using different types of molecules and different substrates. Common examples are alkylsiloxane monolayers, fatty acids on oxidic materials and alkanethiolate monolayers. Here, we will concentrate exclusively on SAMs of alkylsilanes on metal oxide surfaces,

since this type of SAMs is the focus of our studies. Common alkyl silanes used in the formation of SAMs are simple hydrocarbon, fluoroalkyl and end-group substituted silanes. Trichlorosilane, trimethoxysilane and dimethylchlorosilane are examples of reactive functionalities. Figure 2.1 and Figure 2.2 are the schematic representations of a proposed chemistry and final structure of SAMs, respectively. Silanes with one hydrolysable group maintain interphase structure after deposition by forming a single oxane bond with the substrate. Silanes with three hydrolysable groups may form siloxane (silsesquioxane) polymers after deposition, bonding both with each other as well as the substrate.

SAMs offer a means to alter and control the chemical nature of surfaces. Therefore, they hold great promise for applications in different areas, such as composite membranes for gas separations[1-3], packings for reversed-phase liquid chromatography[4-7] and surfaces of micro-electro-mechanical systems (MEMS).[8-10] The novel properties conferred upon the surface arise from the nanometer-level structure, dynamics, and energetics of the tethered organic layer. Hence, fundamental understanding of SAMs' behavior at the molecular level is the key to improved SAM performance, and thus the design of novel materials with desired properties.

Much experimental and theoretical work has been carried out to gain an understanding of the link between the nanoscale characteristics of a surface film and its macroscopic behavior[12,16-26] in various applications. For example, Klatt and Beck[5-7] and Slusher et al.[4] both used molecular simulations to study a model of the reversed-phase chromatographic system where the hydrocarbon chains were placed randomly on silica

surfaces. Various equilibrium and dynamical properties of the chains were computed including the density and solvent orientation profiles as a function of distance from the walls[4], temperature-dependent behaviors, torsional angle populations, order parameters and mean square displacements. [5-7] Another example is the studies of the effect of chain length, system size, and temperature on the preferential adsorption and phase behavior of mixed SAMs of alkanethiol on Au (111) surfaces.[44]

The ability to control and predict properties of SAMs will facilitate the efforts towards the development of biocompatible materials, biosensors, molecular electronics, MEMS and membranes. In our studies, we employed molecular simulation to further extend the understanding of SAMs and specifically focused on three particular applications of SAMs: inorganic-organic composite membranes, MEMS and OMMs surface treatments. The following main sections, 2.2, 2.3 and 2.4, give some background in each application mentioned above, respectively.

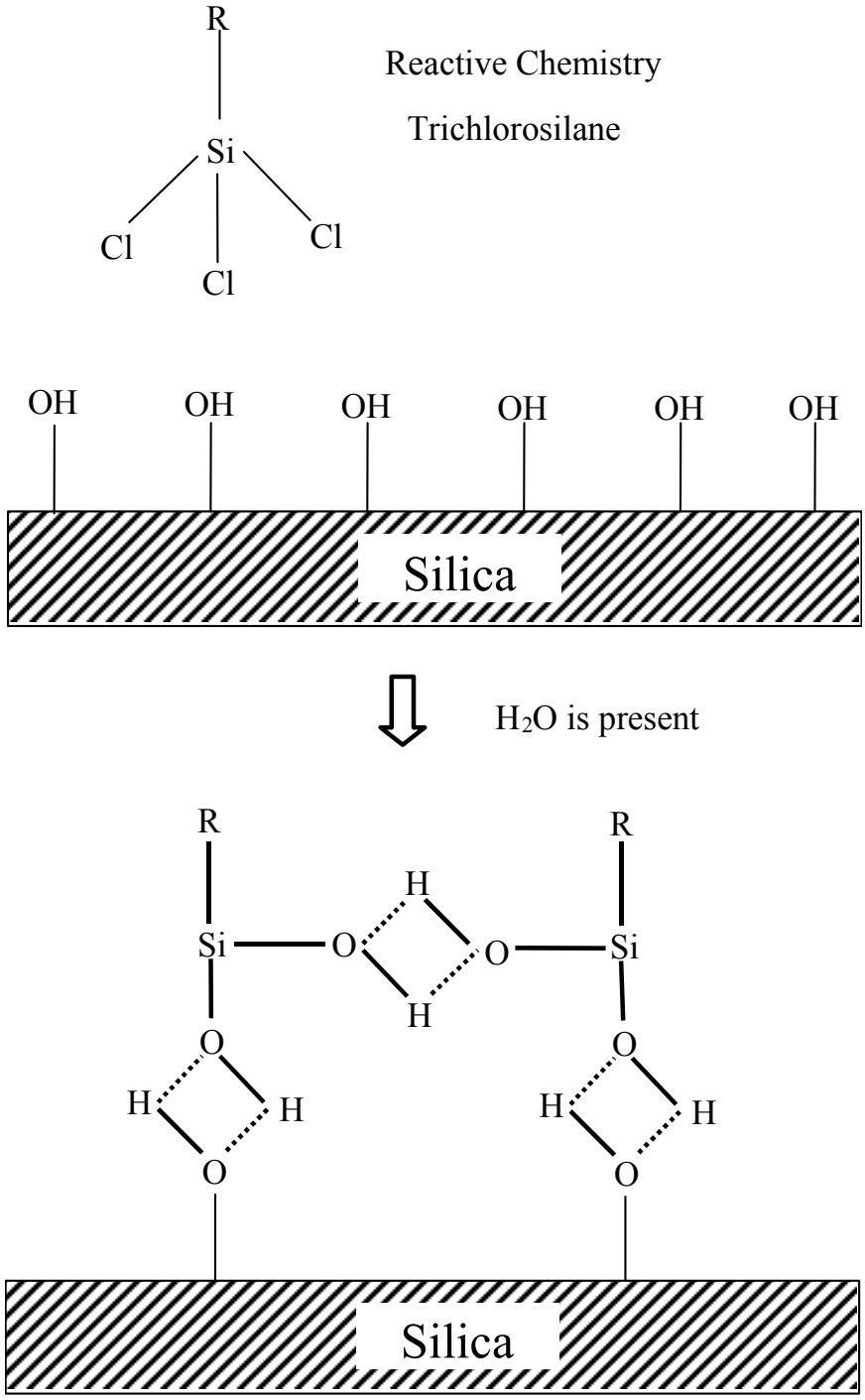

Figure 2.1 SAMs chemistry.[34]

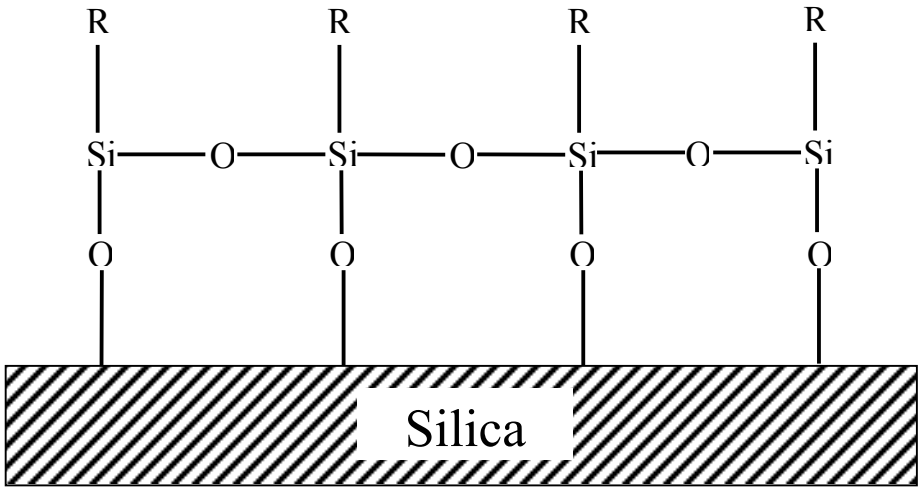

Figure 2.2 The final structure of SAM-coated surfaces.[34]

2.2 Gas Separation with Membranes

Membrane-based gas separation processes have become increasingly important in the chemical process industries, due to their relatively low capital costs and straightforward scalability.[45-48] Membranes are currently used to separate several low molecular weight gas mixtures, as well as volatile organic compound (VOC) vapors from air. A membrane-based separation is caused by differences in the permeabilities of the gas components through the membrane material. For a given pure gas *A*, its

permeability through a polymer can be thought of as the product of a thermodynamic contribution (solubility) and a kinetic contribution (diffusivity), as in Eqn. (2.1).

$$P_A = D_A S_A \tag{2.1}$$

Hence, for a binary mixture of gases *A* and *B*, the permselectivity of the membrane for *A* over *B* is given by

$$\alpha_{A/B} \equiv \frac{P_A}{P_B} = \frac{D_A}{D_B}\frac{S_A}{S_B} \equiv \alpha^D_{A/B}\alpha^S_{A/B} \tag{2.2}$$

where $\alpha^D_{A/B}$ and $\alpha^S_{A/B}$ are the diffusivity-selectivity and the solubility-selectivity, respectively. In general, all of these properties are the functions of the concentrations of all components across the membrane. However, when concentrations of penetrants are low (e.g. for light gases at low pressures), these properties become independent of concentration, and $\alpha_{A/B}$ is referred to as an ideal selectivity.

The most common gas separations are based on diffusivity selectivity, such as air separation, hydrogen recovery from a variety of chemical streams and CO_2 removal from natural-gas streams. In such separations, separation occurs due to the preferential permeation of the smaller, more mobile species. Although a majority of membrane separations are based on the diffusive component of selectivity, $\alpha^D_{A/B}$, recent reviews in the literature have pointed out that great opportunities exist for solubility-selective membranes.[47,48]

2.2.1 Solubility-Based Separations

Solubility-based separations can be thought of as the opposite of diffusivity-based separations, because the permeation through the membrane is in favor of the larger, heavier gas component. Solubility selectivity depends on the strength of interaction between the gas molecules and the separation medium as well as the molecular size. Specific energetic properties of molecules, such as hydrogen bonding capability, and dipole and quadrupole moments play important roles in solubility-based separations. However, in nonpolar systems, molecular size alone provides a basis for solubility selectivity; larger molecules will experience greater van der Waals dispersion forces and therefore greater solubility.

Recent studies showed that great opportunities exist for solubility-selective based separations.[47,48] The separation of (VOC) vapors from air[49] and higher hydrocarbons from natural gas[50] fall into this category. For such mixtures, it is more economical and efficient to use a membrane where the permeation rate of the larger, heavier gas component is greater. Solubility-based separations have two major advantages in these cases: a smaller percentage of the total gas flow crossing the membrane leads to a reduced membrane area and therefore reduced cost, and the purified light gas remains on the high-pressure side of the membrane.[48,51]

Freeman and Pinnau, in a recent article[48] discussed the ideal characteristics of a polymer for a solubility-selective membrane. Primarily, the polymer should provide a high solubility-selectivity for one component of the mixture. For nonpolar mixtures or slightly polar gases, as pointed out before, this will presumably be the heavier

component resulting from the greater van der Waals interactions. The solubility differences due to these interactions can be quite remarkable. However, diffusivity-selectivity may have a negative affect on the permselectivity. For example, the solubility of n-pentane is about 1,000 times greater than that of helium in rubbery cis-polyisopropene, yet the diffusivity of n-pentane is about 100 times smaller than that of helium in cis-polyisopropene. Consequently, the permselectivity for n-pentane over helium decreases to ~10 in that material. The ideal polymer for a solubility-based separation therefore should also have a diffusivity-selectivity fairly close to unity[48], which requires then, in most cases, a rather flexible polymer with large free volume. Poly (1-trimethylsilyl-1-propyne) (PTMSP) is a glassy polymer with an exceptional high free volume, whereas Poly (dimethylsiloxane) (PDMS) is a rubbery polymer with a very flexible backbone. Both, because of their low transport resistance, are more permeable to large hydrocarbons than to small permanent gases.

In spite of the two good examples mentioned above, polymeric materials, in most cases, do not naturally have sufficient free volume and an appropriate free-volume distribution. Routes to improved-polymeric membranes generally involve modifying the chemistry of the backbones or side chains to manipulate packing and free volume. This is certainly a reasonable approach, but it is limited. Furthermore, these polymers suffer from aging and swelling effects.[50]

An architecture in which small organic molecules are attached to the porous surfaces of an inorganic substrate is attractive for solubility-based gas separation membranes. This hybrid approach is particularly advantageous because free volume may

be adjusted independently of chain chemistry and the inorganic part of these membranes provides a resistance against undesirable swelling effects.[1,52,53] Paterson and colleagues published a series of papers on the surface modification of inorganic membranes with organic groups.[2,54-56] They used several different organic precursors, including silicone oil, octadecyltrichlorosilane (OTS), and alkyl phosphonic acids. In all cases, they changed the surface functionality of the membranes, making them hydrophobic. In one case, Randon and Paterson[2] attached C4 and C12 phosphonic acids to the surface of 5 nm alumina membranes; after repeated treatments with C12, they significantly increased propane/nitrogen selectivity, albeit with a loss in permeability. McCarley and Way[57] employed OTS on alumina membranes and found significant enhancement of selectivity for heavier gases over lighter ones. Miller and Koros[58] employed a similar material architecture, but used fluorine-substituted organosilanes to make rigid surface phases suitable for diffusivity-based separation membranes. The surface modification of ceramic membranes with alkylsilanes[59-61] and alcohols[62] has been proposed for liquid-phase separations as well. Martin and co-workers have used self-assembled monolayers in gold-coated[63-65] and silica[66] micropores to make membranes for various applications. In related work, the grafting of polymers into the pores of ceramic[67-71] and porous polymer[72-74] substrates has also been pursued as a route to highly selective and permeable membranes. The placement of small organic molecules on the walls of porous adsorbents such as MCM-41 has also been the subject of much recent interest.[12,43,75-77]

Our work in this area was inspired by and done parallel to the experimental work of Javaid et al. who have recently shown that a certain type of composite membrane,

based on the same approach, (the chemical modification of porous inorganic surfaces with organic functionality), exhibited excellent performance in solubility-based separations.[1] They modified 5 nm and 12 nm alumina membranes using different alkyl trichlorosilanes with chain lengths ranging from C4 to C28[1], and measured the permeability of these membranes to different gas species. Javaid et al.[1] demonstrated that it is possible to "tune" the gas separation properties of the material for particular applications by changing the pore size and hydrocarbon chains.

However, the molecular-level reasons for the performance changes are not known, which makes further rational design and improvement of these materials difficult. For example, it is not clear whether the enhancements in solubility-selectivity were due to the formation of a dense organic phase that spanned the pores (or at least pore mouths), or simply by the reduction in effective pore size due to the formation of thin organic layers at the pore walls. (It is well known that fluids confined to microporous solids exhibit vapor-liquid transitions at pressures below the bulk vapor pressure, and that this capillary condensation effect occurs earlier in smaller pores.[78-81]) Furthermore, the extent to which the pore size, organic chain length, or chain surface density will affect the importance of such capillary condensation is unknown. In our work, we use molecular dynamics (MD) simulation to gain further understanding of the relationship between microstructure of this type of composite membranes and separation performance.

2.3 Micro-Electro-Mechanical Systems (MEMS)

Micro-electro-mechanical systems (MEMS) are the basis of a relatively new technology that exploits the existing microelectronics infrastructure to create complex machines with micron-size features. Most of the MEMS devices explored and designed to date are based on silicon. These machines can have many functions, including sensing, communication and actuation.[27-29] Extensive potential applications for these devices exist in commercial, medical and defense systems, accelerometers in smart airbags, micro-mirror MEMS in new projection TVs, micro nozzles that direct the ink in inkjet printers, lab-on-chips: bio analyzer for DNA, RNA and protein analysis, to list a few examples.[82] However, MEMS suffer from friction, adhesion and wear problems during their fabrication and also during use. In a typical polysilicon-based integrated MEMS device, surface microstructures range from 0.1 to several μm in thickness with lateral dimensions of 10-500 μm, and lateral and vertical gaps to other structures or to the substrate of around 1 μm.[8,9] The large surface area and small offset from adjacent surfaces make these microstructures especially susceptible to adhesion upon contact. In addition to adhesion, peeling (friction) phenomena are important in many microdevices. This problem is more generally called *stiction*. Stiction is present during the release process when the surface tension of the draining rinse liquid draws the microstructure into contact with the underlying substrate (release stiction). Stiction also occurs later in use, when intentionally or accidentally parts come into contact (in-use stiction). Strong adhesion is generally caused by capillary, electrostatic and van der Waals forces, and in some cases by “chemical” forces such as hydrogen bonding and solid bridging.

Treatments are needed that render the surfaces hydrophobic to eliminate the capillary forces, stable both under ambient and elevated temperatures, hard and wear resistant, and electrically conductive to minimize charge trapping.

Several approaches have been investigated to alleviate release and in-use stiction. These methods have been more extensively discussed in the literature.[9,83-87] One solution to the above problems involves coating of the microstructural surfaces with organic self-assembled monolayers (SAMs). Hornbeck used SAMs as lubricants for digital micromirror devices as early as 1987.[10] A recent review concludes that SAM coatings are effective at reducing adhesion during microstructure release and thus can be used as anti-stiction coatings for micro-electro-mechanical systems (MEMS) devices.[9] SAMs have a number of remarkable properties, which make them an attractive option for antistiction coatings in microstructures. First of all, these films are very stable after formation and are resistant to acidic media, boiling water and hot organic solvents. Moreover, they possess long-term stability in various environments, low surface energy, a hydrophobic nature, and a densely packed structure.

In the past decade, there have been tremendous amount of experimental studies of SAM-coated surfaces related to adhesion and friction problems. Alkylsilanes on silicon oxide and alkanethiols on gold are the primarily studied systems. However, because of the small (nanometer) length scales associated with SAM coatings and MEMS devices, there is a lack of understanding about why SAMs are effective and how to improve them. The fundamental problem is that friction at these small scales cannot be treated with empirical, continuum models as in the case of macroscopic devices. For

example, when a simple liquid is confined between two solid surfaces with a molecular-scale separation distance, it displays much different behavior than for larger separations. In such cases, the liquids often show solid-like behavior (even under normal pressures), locking the surfaces together until the shear force is strong enough to yield them. The macroscopically observable effect is a stick-slip type motion of the surfaces.[9] New molecular-scale approaches are necessary to provide a theoretical framework for modeling these problems. Molecular simulations can play a role by acting as "experiments" in which the atomic-level details may be observed.[36,37]

There are several issue associated with SAMs in particular that would benefit from study by molecular modeling and simulation. For example, it is not known why friction decreases with increasing chain length in the SAM. There is much speculation on this issue, but hard evidence from experiment is lacking. The molecular dynamics simulations of Leng and Jiang[32] predicted that longer chains have higher lateral stiffness than shorter chains, leading to lower friction. On the other hand, longer chain SAMs have more cohesive energy and therefore are more tightly packed; from this perspective, one might expect longer chain SAMs to be more solid-like and exhibit higher friction. Another important aspect is that of domain dynamics; real SAMs will have defects in packing structure arising, for example, from randomness in the underlying substrate or distributions of chain lengths. For a close-packed SAM, a gauche defect in one chain most likely requires gauche defects in a large set of neighboring chains, just due to steric effects.[34] The size of these packing domains, and the nature of the boundaries between them, will affect the dissipation of energy during operation. Lio et al.[88] measured the

chain length dependence of friction between two SAMs using an atomic force microscope (AFM) for n=6, 8, 12 and 18 carbon atoms for both alkylsilanes on mica and alkanethiols on gold. These authors concluded that the disorder is the cause of the larger friction for smaller chain lengths where the SAM structure was more disordered and had lower coverage.

Another counter-intuitive observation is that SAMs with terminal fluorocarbon end groups have significantly larger friction coefficients than completely hydrocarbon SAMs. Since the van der Waals interaction strength is weaker in fluorocarbons than in hydrocarbons, one might expect weaker adhesion in fluorocarbon SAMs, as is seen for fluorinated polymer surfaces.[26] By extension, one might also expect these "less-sticky" fluorinated SAMs to exhibit less friction than hydrocarbon SAMs. Since this expectation (based on static energetics) is not accurate, there must be other molecular characteristics (most likely related to the SAM dynamics) that lead to the observed behavior. For example, fluorine is larger than hydrogen, which should reduce the range of motion in the SAMs. Also, the torsional barrier is higher in fluorocarbon chains. Either of these two reasons could cause fluorocarbon SAMs to dissipate more energy than hydrocarbon SAMs. Presently, the importance of either factor is unknown and could be examined by molecular simulations.

In this work, the adhesion between two ordered SAMs of alkylsilane chains on a silicon dioxide surface at full coverage are studied using molecular dynamics simulations as a function of chain length.

2.4 Adsorption in Surface-Modified Porous Materials

Surface-modified porous materials play significant roles for the separation of mixtures (high performance liquid chromatography, ion-exchange chromatography, size exclusion chromatography, gas chromatography and solubility-based membranes), catalysis, and biochemical applications due to their tailored surface properties.[1,39-43] Particularly, porous solids with hydrophobic surfaces, for example organo-silane-modified silicas, represent an important group of adsorbents used in chromatography and solid-phase extraction.[89] Modification of a proper silica support with an organosilane provides an opportunity to obtain materials with high mechanical and chemical stability; tailored particle size, pore size and surface area; and the desired functionality and surface properties.

Characterization techniques are crucial to the successful synthesis and application of porous materials.[11-19,90-92] Gas adsorption is one of the valuable tools for characterization of a wide range of porous materials.[93] It provides detailed, accurate, and reliable information about the structure, such as the specific surface area, pore size and shape, pore size distribution, surface functionality. Of all the many gases and vapors, which are readily available and could be used as absorptives, nitrogen has remained pre-eminent. Nitrogen adsorption technique is well-established, simple, and informative. It allows one to determine the specific surface area and pore-size distribution, and to investigate surface properties of unmodified and modified porous materials. Primarily, nitrogen adsorption at 77 K is a standard and widely used method for characterizations

of mesoporous adsorbents. This technique also commonly applied to determine microporosity.[13, 93]

Adsorption of a gas by a porous material is described quantitatively by an adsorption isotherm, which is the amount of gas adsorbed by the material at a fixed temperature as a function of pressure.[94] Adsorption isotherms were classified into six types by IUPAC Commission on Colloidal and Surface Chemistry (1985). These six types are shown schematically in Figure 2.3. A brief description of each class was given in terms of pore size.[13,14,93-96] Each type reflects the relationship between porosity and adsorption.

Type I (the Langmuir isotherm) was qualified to microporous solids (pore widths below 2 nm). However, Type I isotherms may also be observed for mesoporous materials with pore sizes close to the micropore range. As relative pressures approaches unity, the curve may reach a limiting value or rise if large pores are also present. Type I isotherms are quite common for the ordered mesoporous materials (OMMs) with organic groups bonded to a silica framework.

Types II and III are representatives of nonporous materials with strong (type II) or weak (type III) fluid-wall attractive forces. There is no adsorption-desorption hysteresis. Nitrogen adsorption isotherms similar to Type II were reported for several as-synthesized (surfactant-containing) OMMs. Type III adsorption isotherms were reported for water adsorption on certain ordered organic-inorganic nanocomposites with hydrophobic surfaces.

Types IV and V occur for strong and weak fluid-wall forces, respectively, when the material is mesoporous (pore widths between 2 and 50nm) and capillary condensation occurs with pronounced hysteresis loops (capillary condensation and capillary evaporation do not take place at the same pressure). Capillary condensation is the phenomenon whereby a fluid whose chemical potential, or pressure, is less than its value at saturation and is, therefore, a gas in *bulk*, condenses to form a dense liquid-like state inside a narrow capillary or in the pores of a solid[97] (it indicates a shift of the bulk gas-liquid equilibrium caused by confinement). Experimentally, capillary condensation is characterized by a typical step in adsorption isotherms. It was suggested and clearly confirmed after the discovery of OMMs that capillary condensation in mesoporous may also be reversible, meaning it may occur without an appearance of the hysteresis loops (this behavior will be denoted as Type IVc and shown in Figure 2.3).

Type VI occurs for some materials with relatively strong fluid-wall forces, usually when the temperature is near the melting point for the adsorb gas. It represents adsorption on nonporous or macroporous solid where stepwise multilayer adsorption occurs.

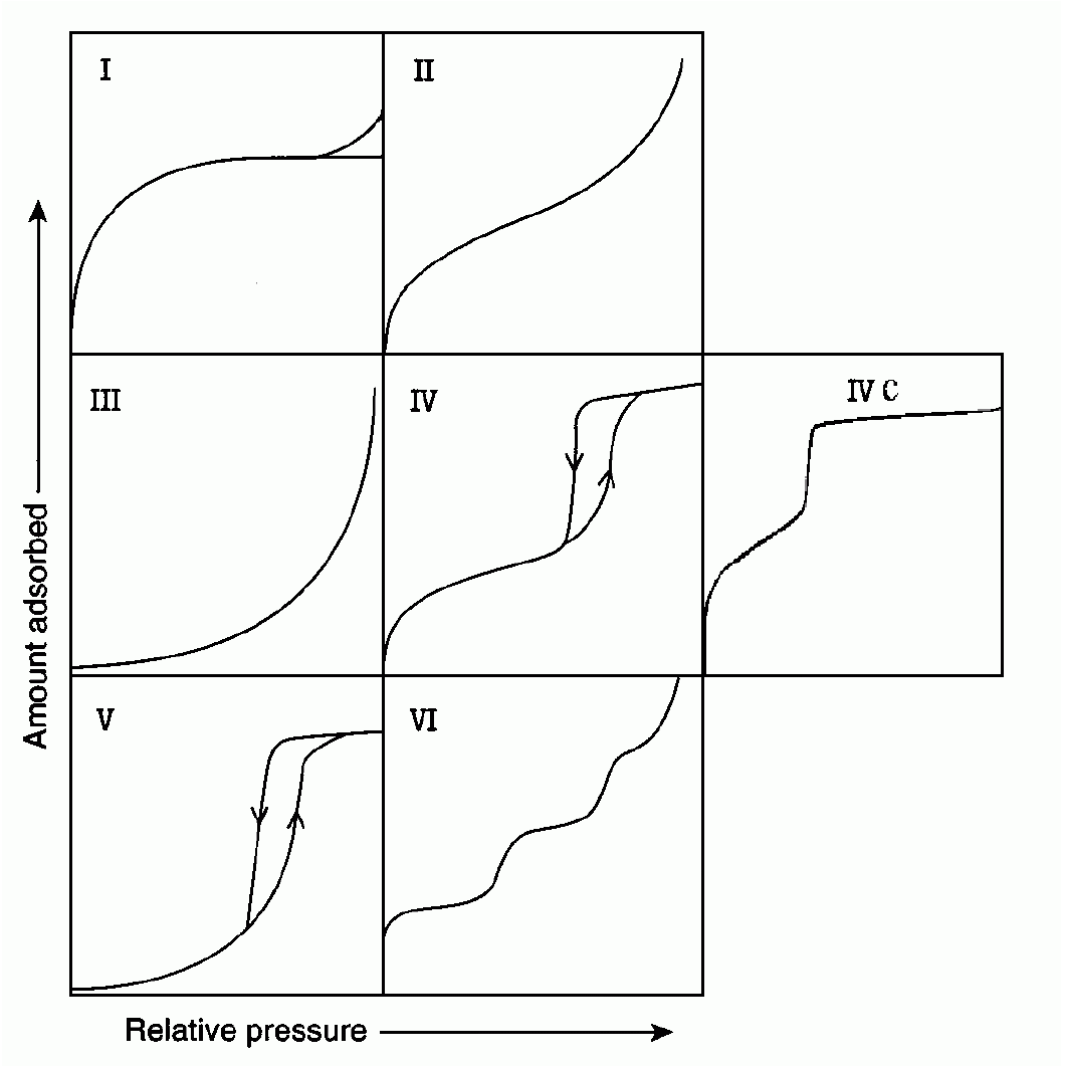

Figure 2.3 IUPAC classifications of gas adsorption isotherms.[13, 94]

The phenomenon of adsorption-desorption hysteresis was subject to various investigations, however, the main reason or reasons behind it are not fully understood. There are several thoughts about the origin of this phenomenon. The hysteresis is usually attributed to thermodynamic or network effects or the combination of the two effects.

Thermodynamic effects are associated to the metastability of the branches (adsorption or desorption or both) in the adsorption isotherms. In other words, the capillary condensation or evaporation may be delayed and take place at higher or lower pressures, respectively, in comparison to the pressure of coexistence between the gas-like and liquid-like phases in the pore.[13,14,96] The hysteresis may also be caused by pore connectivity (network) effects: If the larger pores are connected to the surroundings via narrower pores, the narrower pores may be still filled with condense adsorbate when the larger pores are supposed to be emptied. As a result, the capillary evaporation in the larger pores may occur at the relative pressure corresponding to the capillary evaporation in the smaller pores, as supposed to the relative pressure corresponding to their own capillary evaporation.[13,14]

The hysteresis loops are classified into four types by IUPAC Commission.[14] All the types are illustrated in Figure 2.4. The Type H1 loop exhibits parallel and nearly vertical branches. This type generally represents its relatively high pore size uniformity and simplistic pore connectivity. The Type H2 has a triangular shape and a steep desorption branch. This behavior was observed many porous inorganic oxides and associated with the pore connectivity effects, which were often considered to be a result of the presence of pores with narrow mouths (ink-bottle pores). However, Kruk et al.[13] suggested that the appearance of a H2 hysteresis loop in the proximity of the lower pressure limit of adsorption-desorption hysteresis should not be regarded as evidence of poor pore connectivity or ink-bottle pore shape. In fact, novel materials having uniform cage-like pores, and thus suitable as model solids with ink-bottle pores, exhibited

adsorption isotherms with broad hysteresis loops but without any dramatic differences in steepness of adsorption and desorption branches. These hysteresis loops seemed to be intermediate between types H1 and H2, rather than being H2.[13,14]

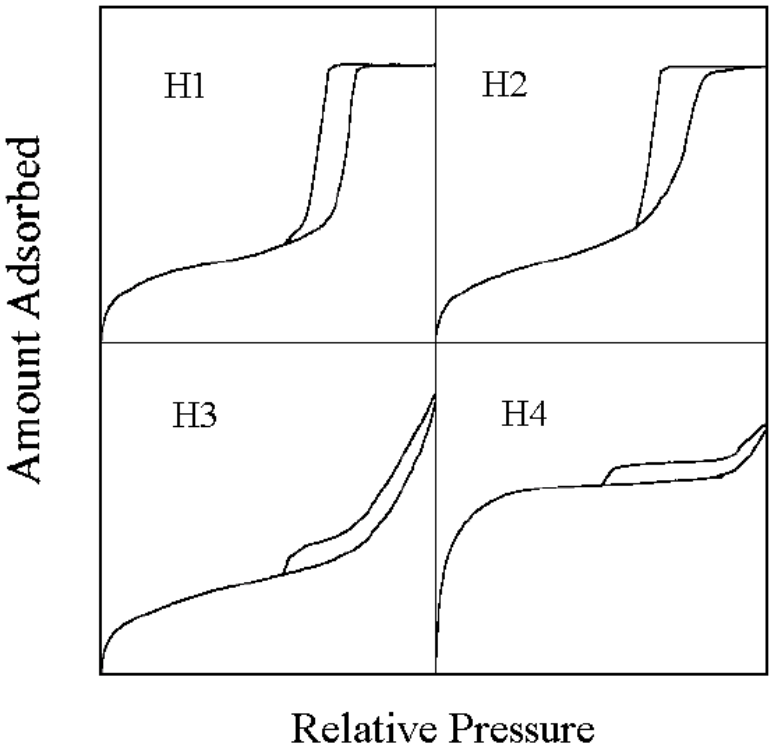

Figure 2.4 IUPAC classifications of adsorption-desorption hysteresis.[14]

Type H3 loops do not level off at the relative pressures close to the saturation vapor pressure. They were reported for materials consist of aggregates (loose assemblages) of plate-like particles forming slit-like pores. Type H4 exhibits parallel and almost horizontal branches and their appearance has been connected to adsorption-desorption narrow slit-like pores.

2.4.1 Unmodified Ordered Mesoporous Materials

Porous materials of well-defined geometry have been of great interest, since such materials are desirable as catalysts, catalyst supports, and shape/size selective adsorbents. Although the synthesis and application of ordered microporous solids, such as zeolites, have been well established, extensive efforts have been made to develop geometrically well-ordered mesoporous materials. Ordered mesoporous materials (OMMs) were reported for the first time in 1990 by Kuroda and coworkers[38], however, it was the discovery of scientists from Mobil Oil published in 1992[38] that attracted much attention and pioneered a significant and still rapidly growing research in the direction of synthesis, application, and characterization of ordered mesoporous materials.[11-19,38-43,90-94] These novel materials, a large family of mesoporous silicates and aluminosilicates, are currently known as the M41S molecular sieves.[94]

One of the members of the M41S family, namely MCM-41, has been subject to a wide-range of studies, because of their remarkable properties. MCM-41 molecular sieves exhibit hexagonal arrays of long, unconnected cylindrical pore channels whose diameter can be varied from 1.5 to 10 nm, depending on the preparation method.[92,94] Their pore

sizes can be tailored with in a wide range, primarily by changing the alkyl chain length of the templating surfactants used in the synthesis processes.[94] They are easy to synthesize, and due to their well-ordered structures, MCM-41 could be used to test our understanding of adsorption at the molecular level and to evaluate methods for the prediction of adsorption equilibrium. Moreover, surface properties of MCM-41 can be easily modified due to the presence of silanol groups on the surface, which actually makes them suitable for chemical bonding of organic ligands or anchoring inorganic species. This aspect of the materials promises a wide range of application of MCM-41 molecular sieves in the field of catalysis.

2.4.2 Surface-Modified Ordered Mesoporous Materials

Recently, the synthesis and application of surface-modified silica based ordered mesoporous materials (OMMs) have become an area of rapid growth in research. There are several reasons to expect this attention. First of all, this type of inorganic-organic porous composite materials has been extensively studied in the past[11-19] and found applications, as catalysts or adsorbents, in many areas of science and technology, such as in chromatographic separations or removal of heavy metal ions from water.[38-43] In addition, nearly unlimited possible structures of organic ligands that can be bonded to the silica surface allow one to obtain materials that are suitable for desired applications. Furthermore, using OMMs as supports for bonded organic layer offers an opportunity to adjust both pore structure and surface properties of inorganic-organic composite materials. These materials have improved hydrothermal and mechanical stability,

therefore, organic-modified OMMs promise to be highly stable materials with engineered properties and attractive for advanced applications.

There have been numerous experimental studies[11-19], that address the issues of both synthesis and characterization of organic-modified OMMs. Earlier, the applicability of a physical coating procedure for surface modification of conventional[19] and ordered mesoporous silicas[17] was studied by using nitrogen adsorption. The study indicated that the introduction of physically coated species did not alter the mesoporous structure of the silica support. However, it resulted in a shift of pore size distribution toward smaller pore sizes and also in a depletion of smaller pores.[19] Another interesting study focused on investigating the effects of the structure of organic surface groups on low-pressures nitrogen adsorption. For this purpose, several silica gels were modified by chemically bonded octyldimethylsilyl ligands. It was found that low-pressure nitrogen isotherms were greatly decreased by organic modification of the silica gels.[98] Recently, Jaroniec et al.[12] also investigated the surface modification of a good quality large-pore MCM-41 material via chemical bonding of trimethylsilyl(TMS), butyldimethylsilyl (BDMS), and octyldimethylsilyl (ODMS) monomeric ligands and polymeric 3-aminopropyl (APS-P), hexanoyl-3-aminopropyl (HAPS-P), and octyl (OS-P) phases. It was shown that the increase in the size of bonded ligands led to a systematic shift of the step of capillary condensation in primary mesoporous toward low pressures. In addition, the increase in the size of bonded ligands resulted in a gradual decrease in the pore size.[12] Although, they presented a detailed study of structural and surface properties of organic-modified MCM-41 with wide range of sizes and functionalities, there are still some molecular

level details that remained to be investigated. For example, MCM-41-based octyl-bonded stationary phases (ODMS and OS-P) showed an interesting behavior, as their nitrogen adsorption were not reversible at relative pressures below 0.4, giving rise to a low-pressure hysteresis. A few possible explanations for the observed result were speculated by the authors, yet the underlying molecular reasons remained uncertain. Our work is stimulated by the need for the further studies to gain more molecular insight to the problems in organic-modified OMMs. In this direction, we employed grand-canonical Monte Carlo simulations to obtain the nitrogen adsorption isotherms for unmodified and modified porous material models. Although the focus in this work is more on the ordered mesoporous materials, we believe that the results from our studies could apply and be beneficial to any porous materials consist of silica surfaces modified with organosilanes. The main objective of this study is to contribute to the fundamental understanding and the modeling of this type of materials.

CHAPTER III

MOLECULAR SIMULATION METHODS

The purpose of this chapter is to explain the tools and the methods that have been employed in our studies. The first section describes general features of the molecular modeling. Sections 3.2 and 3.3 give brief introductions to the two main molecular modeling methods: molecular dynamics and Monte Carlo. Subsections 3.3.1, 3.3.2 and 3.3.3 focus on canonical Monte Carlo, grand canonical Monte Carlo and coupled-decoupled configurational-bias Monte Carlo techniques, respectively. Section 3.4 explains the molecular model builders.

3.1 Molecular Modeling

The main ingredients of a molecular simulation are the molecular model and the simulation algorithm. The molecular model is comprised of atoms, or atom groups, that interact with potentials (or "force-fields") described by empirical mathematical expressions. A force-field may consist of site-site type interactions, such as van der Waals and Coulombic forces, as well as intramolecular forces such as chemical bonds, angle bending and dihedral torsional barriers. Assuming that the simulation algorithm is executed correctly, the accuracy of the force-field is one of the important properties that determine how well the predicted properties agree with experimental ones. A typical simulation box will include anywhere from 10^2–10^6 atoms/molecules and employ periodic boundary conditions to emulate a bulk system. With periodic boundary conditions, the simulation box is infinitely replicated in three dimensions; in case of

systems with surfaces or other boundary constraints, the periodicity is not employed in the constraint directions. Macroscopic properties, such as solubility and diffusivity, can be predicted as averages over the simulation trajectory, and molecular-level information about the local environment and dynamics of the atoms can also be obtained. The main power of molecular simulation lies in the fact that the observed macroscopic properties, or trends therein, can often be explained by the molecular-level behavior.[99]

In order to calculate macroscopic properties in terms of molecular properties, molecular simulations use a general approach, the ensemble method of Gibbs, which is based on postulates connecting the desired time average of a mechanical variable with the ensemble average of the same variable. An "ensemble" is simply a (mental or virtual) collection of a very large number of systems, say *A*, each constructed to be a replica on a thermodynamic (macroscopic) level of the particular thermodynamic system of interest. [99-101] For example, suppose the system of interest has a volume *V*, contains *N* molecules of a single component, and is immersed in a large heat bath at temperature *T*. The assigned values of *N*, *V* and *T* are sufficient to determine the thermodynamic state of the system. In this case, the ensemble would consist of *A* systems, all of which are constructed to duplicate the thermodynamic state (*N*, *V, T*) and environment (closed system immersed in a heat bath) of the original system. This particular example, Constant-*NVT* ensemble, is also called the canonical ensemble. The other common statistical ensembles are constant-*NVE*, the microcanonical ensemble; constant-*NPT*, the isothermal-isobaric ensemble and constant- μVT, the grand canonical ensemble. Depending on what properties are fixed, other properties (the conjugate variables) can be

measured over a simulation. For example, in the case of the canonical, constant-*NVT* ensemble, properties *E*, *P* and with more effort μ, can be calculated by using molecular simulations. Another ensemble that we applied in our studies is the grand canonical ensemble. Since the chemical potential, volume and temperature are held constant, and the number of atoms in the simulation box allowed to vary, the grand canonical ensemble is particularly useful for studying the adsorption of molecules in a porous medium, including capillary condensation phenomena[81,102-106] which was the focus of our application of grand canonical Monte Carlo simulations in our studies for adsorption in surface-modified porous materials. Since, the chemical potentials of the bulk and the pore phases are equal at equilibrium, fixing the chemical potentials fixes the state of the bulk phase. Thus, we can obtain the pressure of this phase from an equation of state or a separate (bulk) simulation.

The average of any property over a simulation can be predicted by

$$\langle B \rangle \approx \frac{1}{n} \sum_{\alpha=1}^{n} B\left[p_\alpha^N, r_\alpha^N \right] \tag{3.1}$$

where p_α^N is the momenta and r_α^N, positions of all particles in microstate α; n is a set of microstates that should be generated according to the appropriate weighting function for the ensemble of interest. It is the task of a simulation algorithm to generate these microstates in an ensemble, in proportion to their statistical weights (probabilities).

Molecular simulation algorithms can be deterministic or probabilistic. Next, two main molecular simulation techniques: molecular dynamics (MD) and Monte Carlo (MC) will be discussed in more detail.

3.2 Molecular Dynamics (MD)

Molecular dynamics simulation is a deterministic method based on computing the motion of each atom in the simulation box by integrating Newton's equation of motion ($f = m \cdot a$) over time. Each of the N atoms or molecules in the simulation is treated as a point mass and given an initial velocity chosen from the Maxwell-Boltzman distribution. The physics of the model is contained in the force-fields (potentials) acting between the atoms. These force fields provide the potential energy associated with a given arrangement of the atoms within a system. The force on each atom is given as the gradient of this potential energy. A variety of useful microscopic and macroscopic information can be obtained by using MD simulations, such as transport coefficients, phase diagrams, and structural or conformational properties.[99]

MD simulations might become computationally "large" depending on the number of atoms and number of timesteps. Since the length scale for atomic coordinates is Angstroms, in order to approach even the sub-micron scale, many thousands or millions of atoms must be simulated. The timestep size should be selected as large as possible, because the increased timestep size provides more "real time" per MD step, thus more "real time" per CPU time. However, the timestep size is limited by the highest frequency motion of the atoms, which needs to be accurately tracked. For example, if

there are bonds involved with the system, the timestep should be chosen based on the vibrational motion of the atoms. This limits timesteps to the femtosecond scale, thereby tens or hundreds of thousands of timesteps are necessary to simulate even picoseconds of "real" time.[107] Therefore, especially when the system is densely packed, this method might suffer from timescale limitations. In that case, since it will take relatively longer time for atoms to sample configurations, one might not be able to observe the phenomena of interest on the time scale of the simulation.

MD simulation was used as the main tool for predicting diffusivity and infinite-dilution solubility in the composite material study, and it was used for all simulations in the MEMS study. All MD simulations in this work were done in constant-*NVT*, the canonical ensemble.

3.3 Monte Carlo (MC)

Monte Carlo (MC) simulation is a probabilistic technique in which atomic configurations are sampled according to their probabilistic weight. There is no "time" in an MC simulation, but according to the ergodicity principle, a properly weighted average over the configurations is equivalent to a time average. Therefore, conventional MC techniques can not be used to predict dynamic phenomena. In contrast to molecular dynamics, Monte Carlo seeks to determine only the equilibrium properties of a system. Although the MC method can be used for all equilibrium property calculations for which MD can be used, it is most commonly used for the calculation of free energies and phase equilibria.[78-81]

In MC, an initial state is constructed, often stochastically, that is preferably one of high probability. Then, a "Markov chain" is started by attempting to move a particle to a new position or orientation. If we define π_{ij} as probability of going to state j given that you are in state i, states in the Markov chain must satisfy the important condition of microscopic reversibility,

$$P_i\pi_{ij} = P_j\pi_{ji} \tag{3.2}$$

in order to sample the correct limiting distribution. Furthermore, the set of moves selected must allow an access to the all possible configuration space for the systems of interest. Acceptance of new states is performed probabilistically, most commonly according to the Metropolis criterion which is explained in the next section in more detail.[99,108]

Because a Monte Carlo simulation is not required to evolve a system through time according to Newton's Laws, it can often be made much more efficient in sampling molecular configurations than molecular dynamics. A Monte Carlo simulation is allowed to make highly unphysical moves that would never occur in the natural dynamics. In fact, if one knows some properties of the system to be simulated, one can incorporate this information into the design of highly efficient, biased moves.[99] Technically, all that is required is that the proposed biased move (1) lead to a Markov process, (2) lead to ergodic and regular sampling, and (3) satisfy balance or detailed balance.[109]

The number of steps in Monte Carlo simulation depends on the complexity of the intermolecular potentials and the desired accuracy of the results. 10^4-10^5 MC steps per

particle are usually sufficient in order to determine thermodynamic properties of a fluid interacting with a Lennard-Jones potential.[110]

3.3.1 Canonical Monte Carlo

A classical Monte Carlo simulation for a system with a constant total number of particles, temperature, and volume (canonical ensemble), would sample the Boltzmann distribution

$$P(r_1,...,r_N) = Z^{-1} \exp\left[-U(r^N)/(k_B T)\right] \tag{3.3}$$

where k_B is Boltzmann's constant, and Z is the configurational partition function that normalizes the probability distribution:

$$Z = \int dr^N \exp\left[-U\left(r^N\right)/\left(k_B T\right)\right] \tag{3.4}$$

Here U is the configurational potential energy of the system, which is calculated from a force field; k_B is the Boltzmann constant and T is the temperature. Averages of any molecular property, say B, are given by averages over this distribution:

$$\langle B \rangle = \frac{\int dr^N G(r^N) \exp\left[-U\left(r^N\right)/\left(k_B T\right)\right]}{\int dr^N \exp\left[-U\left(r^N\right)/\left(k_B T\right)\right]} \tag{3.5}$$

A Monte Carlo simulation accomplishes this task by producing a series of molecular configurations $r^N(1), r^N(2),...$ Each particular configuration occurs with the Boltzman probability, and so molecular averages can be computed as simple averages over the configurations produced in the Monte Carlo run, as in Eqn. (3.1).[99,108]

It is in general not possible to evaluate Z, however, as previously mentioned, it is possible to compute the averages of any molecular property, B, without explicitly evaluating the value of the configurational partition function. One can devise an efficient Monte Carlo scheme to sample such a ratio. Here we discuss only the Metropolis scheme for a simple monatomic fluid, because it is simple and generally applicable. In the Metropolis scheme, the following steps are taken:[99,108]

1) Select an atom at random, and calculate its energy $U(r^N)$.

2) Consider a cubic region (length δ per side) centered on this atom. Attempt a move by displacing the atom, with uniform probability, within this cube and calculate its new energy $U(r'^N)$.

3) Accept the move from r^N to r'^N with probability

$$P_{acc} = \min\left(1, \frac{P_{new}}{P_{old}}\right) = \min\left(1, \frac{\exp\left[-\beta U(r'^N)\right]}{\exp\left[-\beta U(r^N)\right]}\right) = \min\left(1, \exp\left[-\beta \Delta U\right]\right) \tag{3.6}$$

where $\beta = 1/k_B T$.

In other words:

If $U_{new} \le U_{old}$, accept it.

If $U_{new} > U_{old}$, accept it with probability $\exp\left[-\beta \Delta U\right]$.

Any constant value of δ satisfies detail balance. However, small value of δ provides high percentage in acceptance and small change/step, while large δ provides low percentage in acceptance and large change/step. Since we are free to choose δ, we should choose it to produce the smallest statistical error (variance) in the estimates of our properties of interest, in a given amount of CPU time. In general, it is common to choose δ such that 20-50% of attempted moves are accepted.

3.3.2 Coupled-Decoupled Configurational-Bias Monte Carlo (CD-CBMC)

The sampling of equilibrium conformations of complex fluids such as polymers is usually time consuming, because these systems include bonds and other "intramolecular" potential features. The natural dynamics of polymers are dominated by topological constraints; for example chains can not cross. Therefore, the tremendous flexibility of the Monte Carlo method (capability of unphysical moves) for particle simulations has been exploited for the design of many efficient sampling schemes for systems composed of chain molecules.[111] The starting point for the improvements in sampling efficiency for such systems is the introduction of the configurational-bias Monte Carlo (CBMC) technique by Rosenbluth and Rosenbluth in 1955.[112] In this section, we first introduce the CBMC scheme and next we present the Coupled-Decoupled Configurational-bias Monte Carlo (CD-CBMC) method which is a new generalization of the CBMC method.

A CBMC move consists of selecting a chain molecule randomly and cutting it at a random position, then regrowing it segment by segment in a different position in a

biased way. If the entire molecule is regrown, then the first site of the "regrown" molecule is placed at a random point in the system. The CBMC method generates conformations according to the probability

$$P_{gen} = \prod_{n=1}^{n_{STEP}} \left[\frac{\exp(-\beta U_{LJ}(i))}{W(n)} \right] \exp(-\beta U_{tors}(i)) \exp(-\beta U_{bend}(i)) \tag{3.7}$$

$$W(n) = \sum_{i=1}^{n_{choice}} \exp(-\beta U_{LJ}(i)) \tag{3.8}$$

where n is the growth step, n_{STEP} is the total number of growth steps, i is a particular trial, n_{choice} is the number of trials for which the Lennard-Jones interactions (U_{LJ}) are computed and $W(n)$ is the Rosenbluth weight for growth step n.

This method requires the generation of bond vectors which sample the proper distribution of bond bending and torsional angles for use as trial sites in the Lennard-Jones biased selection. This is usually accomplished by choosing a vector uniformly on a unit sphere, computing its bond bending (U_{bend}) and torsional energy (U_{tors}), and accepting the vector if a random number uniform on (0,1) is less than the Boltzmann weight. This Boltzmann rejection process is repeated until n_{choice} vectors are accepted. Next, for all n_{choice} trial vectors, the external (nonbonded interactions) Boltzmann factors $\exp(-\beta U_{LJ}(i))$ are computed and out of these, one is selected with a probability

$$P_i = \frac{\exp(-\beta U_{LJ}(i))}{W(n)} \tag{3.9}$$

The selected segment becomes the ith segment of the trial conformation of the chain. When the total number of growth steps (n_{STEP}) is completed, the Rosenbluth factor for the new trial conformations of the chain is calculated. A similar procedure is followed to calculate the Rosenbluth factor for the old conformations, except, the calculation of the Rosenbluth weights of the old configuration uses the original conformation to compute the Boltzmann weight for $i = 1$ and selects $n_{choice} - 1$ new trials randomly. A move is accepted with probability:

$$P_{acc} = Min\left[1, \frac{\prod_{n=1}^{n_{STEP}} W(n)_{new}}{\prod_{n=1}^{n_{STEP}} W(n)_{old}}\right] \tag{3.10}$$

where $\prod_{n=1}^{n_{STEP}} W(n)_{new}$ and $\prod_{n=1}^{n_{STEP}} W(n)_{old}$ are the Rosenbluth factor of the new and old configurations of the chain, respectively.

We employed a specific implementation of CBMC, the coupled-decoupled configurational-bias Monte Carlo (CD-CBMC), to move the alkane chains in our adsorption studies. This technique is based on generating conformations in a CBMC growth by coupling the non-bonded (Lennard-Jones) and torsional selections while splitting the angle bending into several decoupled selections. A combination of the coupled and decoupled biased selections allows a great deal of flexibility when designing a CBMC scheme for a molecule.[113] This method is described in more detail in

the paper by Martin and Siepmann.[113] Here, we will present only its "coupling" and "decoupling" features and their advantages.

The general form of the probability of generating and accepting configurations is given in the following equations below:

$$P_{gen} = \prod_{n=1}^{n_{STEP}} \left[\frac{\exp(-\beta U_{LJ}(i)) W_T(i)}{W_L(n)} \right] \left[\frac{\exp(-\beta U_{tors}(j)}{W_T(i)} \right] B(n) \tag{3.11}$$

$$B(n) = \left(\prod_{a=st(n)}^{n_{grow}(n)} \left[\frac{\exp(-\beta U_{bend}^{[a]}(k))}{W_P^{[a]}(n)} \right] \right) \times \left(\prod_{b=st(n)+1}^{n_{grow}(n)} \left[\frac{\exp(-\beta U_{bend}^{[b]}(k))}{W_P^{[b]}(n)} \right] \right) \tag{3.12}$$

$$W_L(n) = \sum_{i=1}^{n_{chLJ}} \exp(-\beta U_{LJ}(i)) W_T(i) \tag{3.13}$$

$$W_T(i) = \sum_{j=1}^{n_{chtor}} \exp(-\beta U_{tors}(j)) \tag{3.14}$$

$$W_P^{[x]}(n) = \sum_{k=1}^{n_{nchbend}} \exp(-\beta U_{bend}^{[x]}(k)) \tag{3.15}$$

$$W_B(n) = \left(\prod_{a=st(n)}^{ngrow(n)} W_P^{[a]}(n) \right) \left(\prod_{b=st(n)+1}^{ngrow(n)} W_P^{[b]}(n) \right) \tag{3.16}$$

$$P_{acc} = Min \left[1, \frac{\prod_{n=1}^{n_{STEP}} W_L(n)_{new} W_B(n)_{new}}{\prod_{n=1}^{n_{STEP}} W_L(n)_{old} W_B(n)_{old}} \right] \tag{3.17}$$

where n_{chLJ}, n_{chtor} and n_{chbend} are the number of trial sites for the Lennard-Jones, torsional, and bond bending interactions respectively. The Rosenbluth weight for torsional energy

calculations is W_T, for bond bending is $W_P^{[x]}$, and for Lennard-Jones interactions is W_L. The value of $st(n)$ is set to 1 or 2 depending on which neighboring sites are being grown. If this is the first growth step and we are growing all of the neighboring sites, then choose one of these sites at random, designate it as the "previous" site, and set $st(n) = 2$. Otherwise, the one neighboring site which we are not regrowing this step is labeled the "previous" site and $st(n) = 1$. Let $n_{grow}(n)$ be the number of sites bonded to the current growth site which need to be grown this step. One can determine the bending angles via decoupled biased selections based on $U_{bend}^{[a]}$ and $U_{bend}^{[b]}$. This decoupled selection has the advantage that a large number of trial sites can be chosen for the less expensive bond angle selection without increasing the cost of performing the other biased selections.

Once all of the bond-bending angles have been determined, for each of the n_{chLJ} selections, n_{chtor} random orientations are chosen randomly, and the torsional energy for all of the beads grown this step is computed and used to select one torsional angle in a biased fashion. Next, the nonbonded interaction energy for each of the n_{chLJ} orientations that were chosen during the torsional selections is computed, and one site is selected in a coupled biased fashion based upon U_{LJ} and the torsional Rosenbluth weights. Coupling the biased selections provides the advantage of that each biased selection sends multiple possible conformations to the next selection step.

3.3.3 Grand Canonical Monte Carlo (GCMC)

In the GCMC, the chemical potential, volume and temperature are held constant. The GCMC is an extension of the same concept in the canonical Monte Carlo. In addition to particle displacements, each GCMC step involves randomly attempted creations and destructions of particles. They are performed and accepted with the following probabilities:[108]

Creation:

$$acc(N \to N+1) = \min\left[1, \frac{V}{\Lambda^3 (N+1)} \exp\{\beta[\mu - U(N+1) + U(N)]\}\right] \qquad (3.18)$$

Destruction:

$$acc(N \to N-1) = \min\left[1, \frac{\Lambda^3 N}{V} \exp\{-\beta[\mu + U(N-1) - U(N)]\}\right] \qquad (3.19)$$

where $\Lambda = \sqrt{h^2/(2\pi m k_B T)}$ is the thermal de Broglie wavelength, V is the volume, N is the number of atoms and μ is the chemical potential.

The probability of attempting a creation must be equal to the probability of attempting a destruction; however, there is some freedom in choosing the relative probabilities of creation/destruction and displacement. Past experiences showed that if the three moves are chosen with equal probabilities, it converges faster.[99]

One disadvantage of the GCMC is that as the density increases, it becomes very difficult to have successful exchanges. For insertions, attempts to create a molecule

frequently fails due to high probability of overlaps (all ΔU_{ins} will be very high), and for deletions, ΔU_{del} will be high as well due to many favorable contacts. As a result, it takes remarkably long time to converge. This problem can be overcome with some type of biased algorithm for selecting the insertion location. The biasing of the underlying stochastic matrix is often done by choosing from among several possible insertion points, with more favorable (energetically) positions weighted more heavily. The biasing is corrected in the acceptance factor for the move.[99] This issue was not a concern in our studies, since our systems are typically dilute.

All the runs in our studies for adsorption in surface-modified porous materials were done with the GCMC. It is used to obtain the adsorption isotherms (plots of adsorb amount (N) vs. chemical potential (μ) or relative pressure).

3.4 Molecular Model Builders

The initial configurations of the alkane-chains were generated by using a modified Markov process, based on Rotational Isomeric State (RIS) method that was introduced by Flory[114] in both studies: composite materials and surface-modified porous materials. To do this, we followed the similar scheme in Theodorou et al.[115] The chains in the simulation box were generated in a bond-by-bond fashion, applying periodic boundary conditions in the directions parallel to the surfaces. The chemical formation of each chain and graphical definition of the generalized coordinates are shown in Figure 3.1. The set of generalized coordinates are chosen to specify the position, orientation,

and configuration of each chain. Definitions of these coordinates are taken from Theodorou.[115] The generalized coordinates defined as follows:

r_0: The mass weighted, three dimensional location of the chain start in the simulation box. Since the chains in our systems are attached to the surfaces, these points are near the surfaces.

l: The C-C bond lengths for consecutive atoms i and j in the chain.

ψ: Eulerian angles that define the rotational orientation of the first three atoms, relative to the laboratory xyz coordinate frame. (Ψ_1: the angle between the x-direction and the projection of bond 1 on the xy plane; Ψ_2: the angle between the z-direction and bond 1; Ψ_3: the dihedral angle between the planes (z-direction, bond 1) and (bond 1, bond 2)).

θ: Supplements of the bond angles between the C-C bonds leading into and out of segment i.

$$\cos\theta_i = \frac{(r_i - r_{i-1})\cdot(r_{i+1} - r_i)}{l_i l_{i+1}} \tag{3.20}$$

φ: Torsion angle of rotation around backbone bonds, with the sign and magnitude defined by Flory's convention.

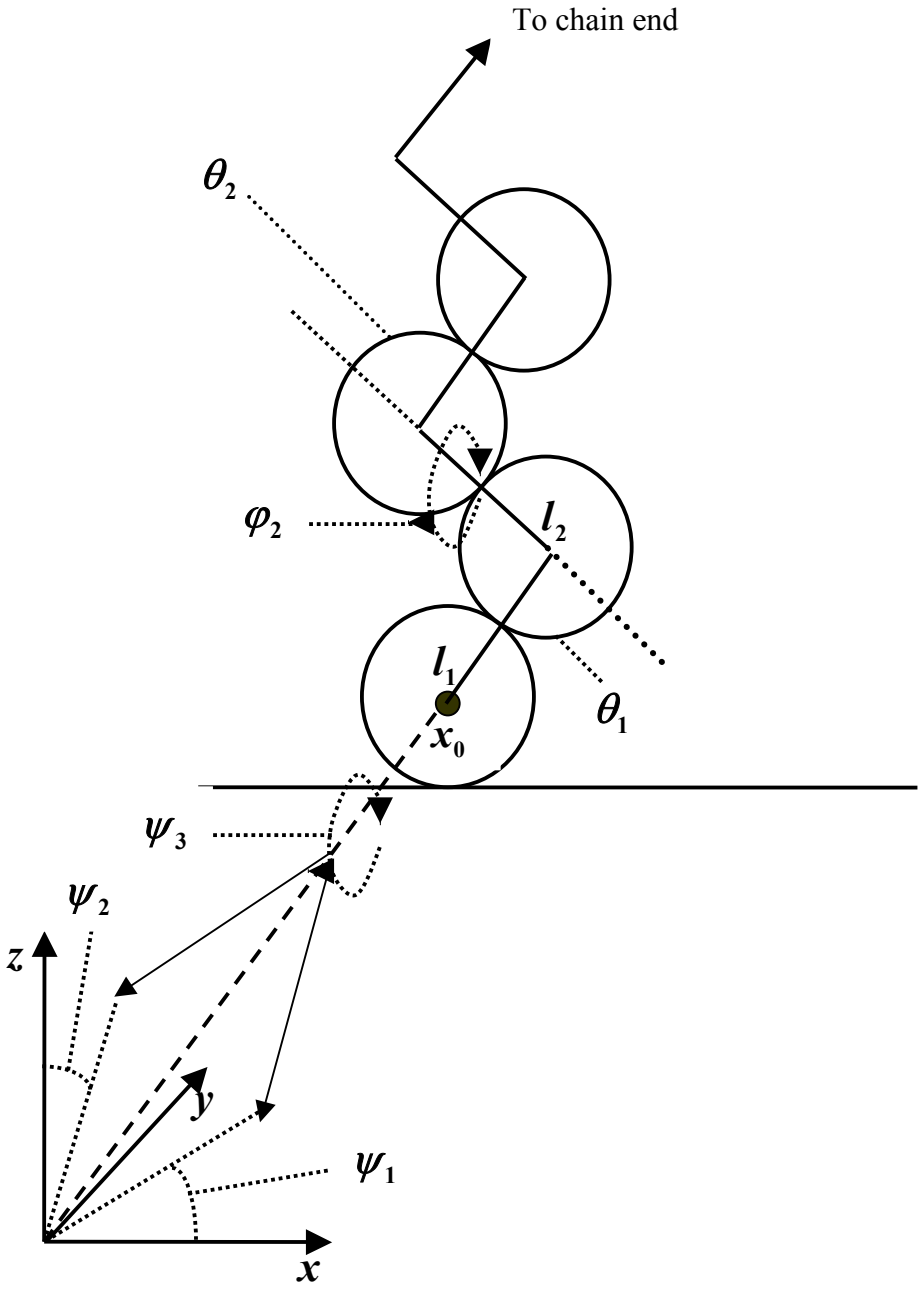

Figure 3.1 2D-graphical representation of a chain. φ is the torsional angle, θ is supplement of the bending angle, l is the bond length, x_0 is the start point and ψ represents the Eulerian angles.

A local coordinate system is defined for each skeletal bond following the conventions of Flory: the *x*-direction is chosen as the next backbone bond, the *y*-direction is defined such that the previous bond lies in the *xy* plane (with its *y* projection signifying the positive direction), and the *z*-direction is chosen such that the coordinate system is "right-handed".[114]

First, the chain start positions, r_0, are placed randomly in the vicinity of the walls. Then, the bond vector $b_i = l_i(1 \quad 0 \quad 0)^T$ directed into the next backbone atom i is written in the local coordinates defined above.

Next, the bond vector is transformed from the local coordinate (internal) frame to the lab (external) frame using an orthogonal transformation matrix, T_0 that depends on the Eulerian angles, Ψ.[115]

$$T_0 = \begin{pmatrix} \cos\Psi_1 \sin\Psi_2 & -\cos\Psi_1 \cos\Psi_2 \cos\Psi_3 - \sin\Psi_1 \sin\Psi_3 & -\cos\Psi_1 \cos\Psi_2 \sin\Psi_3 + \sin\Psi_1 \cos\Psi_3 \\ \sin\Psi_1 \sin\Psi_2 & -\sin\Psi_1 \cos\Psi_2 \cos\Psi_3 + \cos\Psi_1 \sin\Psi_3 & -\sin\Psi_1 \cos\Psi_2 \sin\Psi_3 - \cos\Psi_1 \cos\Psi_3 \\ \cos\Psi_2 & \sin\Psi_2 \cos\Psi_3 & \sin\Psi_2 \sin\Psi_3 \end{pmatrix} \tag{3.21}$$

Another orthogonal transformation matrix, T_i (from the local frame of segment i to the local frame of segment $i-1$), which is a function of θ_i and φ_i, is used to generate subsequent backbone bond vectors.[115]

$$T_i = \begin{pmatrix} \cos\theta_i & \sin\theta_i & 0 \\ \sin\theta_i \cos\varphi_i & -\cos\theta_i \cos\varphi_i & \sin\varphi_i \\ \sin\theta_i \sin\varphi_i & -\cos\theta_i \sin\varphi_i & -\cos\varphi_i \end{pmatrix} \tag{3.22}$$

$$(i = 1,2,...,2x-1)$$

The Eulerian angles (Ψ_1, Ψ_2 and Ψ_3) in T_0 are chosen arbitrarily. The bond length (l), and supplements of the bond angles (θ) are fixed by the structure, and the torsional angles (φ) are chosen uniformly on $(0,2\pi)$ by arbitrary assignment. In order to define φ_1, an imaginary zeroth bond is supplied, and it is taken parallel to the bond 2, so, by definition $\varphi_1 = 0$.

Finally, this subsequent bond vector is added to that of previous backbone segments to find the new atom's position vector (r_i) in the simulation box,

$$r_i = \left(\frac{m_i}{m_0}\right)^{1/2} x_0 + m_i^{1/2} \sum_{j=1}^{i} \left[T_0 \left(\prod_{k=0}^{j-1} T_k \right) b_j \right] \tag{3.23}$$

CHAPTER IV

ORGANIC- INORGANIC COMPOSITE MATERIALS

This chapter contains five sections. Sections 4.1 and 4.2 describe our objectives and models for the study of organic-inorganic composite membranes, respectively. Justification for the model choices are discussed in section 4.3. Section 4.4 explains the property calculations. The results are discussed in section 4.5, and the conclusions are given in the last section.

4.1 Organic- Inorganic Composite Materials for Gas Separation

Our main objective in this work is to use molecular simulations to examine the effects of pore size, organic group size, and organic surface density on the performance of an organic- inorganic composite membrane in a prototype solubility-based separation. This work corresponds to experimental work previously in the literature.[1]

Javaid et al.[1] have performed an extensive set of experimental work for this type of membrane with different chain lengths, pore sizes, and the surface coverages. They carried out surface modification of alumina membranes with 5 and 10 nm pore sizes, using different alkyl trichlorosilanes with chain lengths ranging from C4 to C28. All of these chains were straight except for C28, which had a geminal branched structure. The purpose was to evaluate the roles of pore size and alkyl group length on the separation. Next, they employed C18 trichlorosilane on 5 nm alumina membranes prepared under different conditions of surface hydration. The purpose of these experiments was to

explore the ability to modify the surface coverage of the alkyl Self-assembled Monolayers and monitor its consequences on membrane permselectivity.

Propane, methane, and nitrogen were chosen as test gases for the experiments and employed at ambient conditions of temperature, with pressures up to 5 bar. Permselectivity for a higher molecular weight species over a lower, such as propane over nitrogen, was used as an indicator of solubility selectivity.

In our work, model systems for the experimentally realized nanocomposite membranes of Javaid et al.[1] were simulated. In particular, canonical MD was used to predict the diffusivity and solubility of propane and nitrogen in the model composite materials; the permeability, which is a direct point of contact with the experiments, was obtained as the product of diffusivity and solubility. The model systems are described further below. The focus of the study was on finding the effects of pore size, chain length and surface density for these composite gas separation materials, and comparing them with experiment. For this purpose, we generated density profiles for chains, and solubility profiles for penetrants across the model pores. The diffusivity of penetrants was determined by measuring their mean-squared displacements as a function of time [116], and the solubility of penetrants at infinitely dilute loadings (Henry's law regime) was obtained using Widom insertion method.[117,118] All property calculations are discussed in detail later in this chapter.

The experimental results from Javaid et al.'s[1] work are compared to our simulation results. While the molecular models are a reasonable first-order approximation to the experimental materials, they do not provide exact quantitative

predictions of membrane performance. Rather, we observed that the simulations provide semi-quantitative and qualitative guidance to help us interpret the experimental results, especially the effects of alkyl chain length, pore size, and surface density.

4.2 Molecular Models

The primary variables of interest are chain type (chemical functionality and chain length), surface density of bound chains, and pore size. Figure 4.1 shows a schematic of the basic simulation model that was employed for the composite material. The system under study was periodic in the *x* and *y* directions but bounded by two walls in the *z*-direction. These walls represent the alumina surface of the pore. We treated the walls as flat, featureless surfaces using an interaction potential proposed by Steele.[119]

$$U_{wall}(z) = 2\pi\varepsilon_{gs}\left(\frac{\sigma_{gs}}{\sigma_{ss}}\right)^2\left[\frac{2}{5}\left(\frac{\sigma_{gs}}{z}\right)^{10} - \left(\frac{\sigma_{gs}}{z}\right)^4 - \frac{\left(\sigma_{gs}/\sigma_{ss}\right)^4}{\frac{3}{\sqrt{2}}\left(\frac{z}{\sigma_{ss}} + \frac{0.61}{\sqrt{2}}\right)^3}\right] \tag{4.1}$$

where *z* is the distance in z-direction between the wall and the center of an atom, σ_{gs} and ε_{gs} are the size and energy parameters, respectively, for the pair-wise potential between solid and gas molecules. These parameters were estimated using the venerable Lorentz-Berthelot mixing rules, i.e., a geometric mean for ε_{gs} and an arithmetic mean for σ_{gs} .

$$\sigma_{gs} = \frac{1}{2}\left[\sigma_{gg} + \sigma_{ss}\right] \tag{4.2}$$

$$\varepsilon_{gs} = \left[\varepsilon_{gg}\varepsilon_{ss}\right]^{1/2} \tag{4.3}$$

σ_{gg}, ε_{gg} and σ_{ss}, ε_{ss} represent the size and energy parameters for gas molecules and solid, respectively.

The pores of the alumina membranes are known to be slit-shaped[120], so in terms of geometry this is an accurate model.

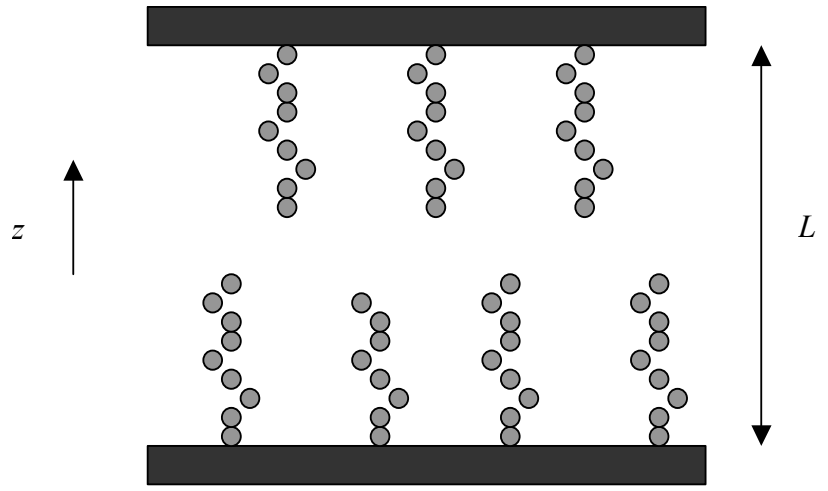

Figure 4.1 Two-dimensional representation of a model slit pore (actual model was three-dimensional). The pore contains a set of deposited alkylsilane molecules tethered to the alumina surface at a fixed coverage. Periodic boundary conditions are employed in the *x* and *y* directions (parallel to the pore walls).

Our choice of pore size *L* was informed by an experimental characterization of the alumina membranes in the literature.[120] The membranes investigated in this study were the commercially available, asymmetric γ-Al_2O_3 membranes used by Javaid et al.[1] These membranes as often referred to as "5 nm cutoff" because they reject (sieve) particles greater than that size.

In the literature, a flow-weighted pore size distribution for the aforementioned membranes was provided. The flow-weighted pore analyzing technique is based on the principal of condensation of a vapor in a capillary as described by the Kelvin equation.[120] The pore size distribution from the literature is shown in Figure 4.2. It can be seen from Figure 4.2 that the distribution for these membranes actually contain a significant fraction of pores smaller than 5 nm (ranged from ~20 Å minimum to ~55 Å).[120] Therefore, we considered values of the pore size *L* (the distance between the walls in *z*-direction) of 30, 50, and100 Å to capture the whole pore size distribution as indicated by the experimental information. The typical box length used in *x* and *y* directions was 30.077 Å.

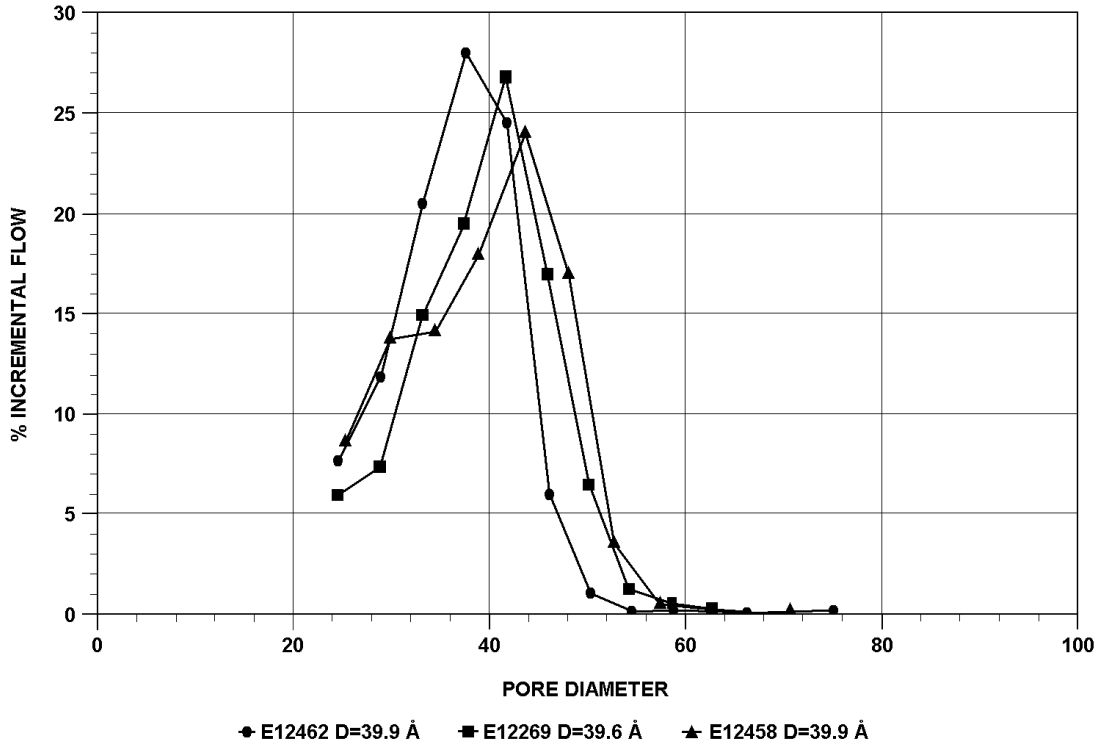

Figure 4.2 Pore size distribution of membranes as-received from manufacturer.[120]

The chains were fixed to the walls with simple harmonic springs. The first monomer of a chain was randomly tethered to the wall within the distance of 3 ± 1.5 Å to capture surface roughness effects. Initial configurations were created with a stochastic builder based on the rotational isomeric states (RIS) method which is explained in detail in section 3.4.[114] For simplicity, we modeled the alkyl segments using the united-atom approach[121] where (-CH_2-) and (-CH_3-) segments were considered as one single site. The non-bonded potential parameters (ε and σ) for the chain segments are taken from Krishna Pant et al.[121] Bond-stretching[121], angle-bending[122], and torsional potentials[122] were

applied to the chain segments. These potentials and their constants are obtained from the literature.[121],[122] Specifically, we modeled octyl (C8), dodecyl (C12) and octadecyl (C18) chains in the 5 nm membrane models to study the chain-length effects, and only octadecyl (C18) chains in the 3 and 10 nm membrane models to study the pore-size effects. Since, in practice, the maximum bonded phase density obtainable is 4 μmol/m^2, unless it is a closed-packed structure[34,123], this surface density was chosen for all the alkylsilane chains throughout these investigations. In addition, the initial surface density was reduced by half to 2 μmol/m^2 for octadecyl (C18) chains in the 3 and 5 nm membrane models to examine the surface coverage effects. The model penetrants were nitrogen and propane, as used in the experiments; they were also modeled by using the united-atom approach. The non-bonded interactions were modeled by the 12-6 Lennard Jones (LJ) potential: [99]

$$U^{LJ}(r) = 4\varepsilon_{ij}\left[\left(\frac{\sigma_{ij}}{r}\right)^{12} - \left(\frac{\sigma_{ij}}{r}\right)^{6}\right] \tag{4.4}$$

where r is the distance between the center of two molecules; ε_{ij} and σ_{ij} are the size and energy parameters for either gas-gas, gas-chain or chain-chain nonbonded interactions. Potential models for nitrogen[118], propane[124] and oxygen (wall potentials)[4] were taken from different sources in the literature.

Canonical MD is the main simulation tool, as implemented through the Large-scale Atomic/Molecular Massively Parallel Simulator (LAMMPS) code licensed from Sandia National Laboratories. LAMMPS has already been developed with many useful

features. One example used for this work is the ability to fix atoms at desired locations with harmonic springs. Although the simulations themselves can be done without further code development, all the codes for the property calculations and analysis were developed internally. Integration was performed with 5 fs timestep. Non-bonded potentials were truncated with the cutoff distance of 9 Å. The temperature of interest was 298 K, corresponding to the experimental temperatures, and constrained via the Nosé-Hoover thermostat [99],[108] with a time constant of 1.271414×10^{-5} $fmsec^{-1}$.

4.3 Justification of the Model Choices

4.3.1 Diffuse Boundary Conditions (DBC) Effects

The use of smooth, rigid walls to model the alumina surfaces is an approximation that must be considered further. Without further modification, this model will produce purely specular reflections. In reality, a penetrant (gas) molecule hitting the wall exchanges momentum and energy with the atoms of the surface. As a result, the velocity vector of a gas molecule leaving the surface after a collision may be de-correlated with the incident velocity vector. Under dense conditions (with respect to chain surface density), the particular boundary conditions will not be important, because collisions with the chains will dominate. However, in dilute conditions, they may be important. Therefore, we employed diffuse boundary conditions (DBCs)[125] to two of the model systems that are dilute in chains: bare membranes and octadecyl (C18)-modified membranes with the surface density of $2\mu mol/m^2$ (C18_sd2). The diffuse boundary conditions were implemented as follows. After each molecular dynamics timestep we

check to see if the following two conditions are satisfied: (1) The center-of-mass momentum (in the laboratory frame) of a given penetrant molecule in the z-direction has reversed in sign. (2) The center-of-mass of that same molecule is within the repulsive region of the Steele 10-4-3 potential. If, and only if, both of these conditions are satisfied, we reselect the center-of-mass momentum of that molecule in the directions parallel to the confining surface from a Maxwell-Boltzmann distribution at the appropriate temperature.[125]

The results and the standard deviations (σ) from these simulations are shown in Table 4.1 for comparison of the two boundary conditions.

Table 4.1 Comparison of the propane and nitrogen diffusivity in the presence and absence of DBC in bare and C18-modified (2μmol/m^2) membranes. These results were obtained at density of 6.33x10^{-5} σ^3 (10 molecules in 100σx100σx15.793σ volume). Dp and Dn represent the diffusivity of propane and nitrogen respectively.

	Dp (cm^2sec^{-1})* 10^{-2}	σ*10^{-2}	Dn (cm^2sec^{-1})* 10^{-2}	σ*10^{-2}
Bare without DBC	9.75	3.7	20.1	1.63
Bare with DBC	0.813	0.2003	1.06	0.0515
C18_sd2 without DBC	0.132	0.0134	0.323	0.0177
C18_sd2 with DBC	0.121	0.00914	0.324	0.0171

In the bare membranes, applying the diffuse boundary conditions (randomly altering the molecules' velocities in *x* and *y* directions upon surface collisions) resulted in significant decreases in the diffusivities of the both penetrants.

In porous membranes, if a system is in dilute conditions, the transport mechanism in that system is driven by the Knudsen diffusion, the mean free path may become comparable with or even greater than the pore diameter so that collisions between a molecule and the pore wall occur more frequently than intermolecular collisions.[126] In the case of Knudsen diffusion, selectivity of the membrane can be determined by the inverse ratio of the square root of molecular weights:

$$\alpha_{i/j} = \sqrt{\frac{M_j}{M_i}} \tag{4.5}$$

which is

$$\alpha_{P/N} = \sqrt{\frac{M_N}{M_P}} = \sqrt{\frac{28}{44}} = 0.8 \tag{4.6}$$

for our system, where M_N and M_P are the molecular weights for nitrogen and propane, respectively. The Knudsen selectivity values that are calculated from the simulation results $\left(\alpha_{P/N} = D_P \big/ D_N\right)$ are 0.485 for the specular boundary condition, and 0.77 for the diffuse boundary condition case. This result demonstrates that the diffuse boundary conditions for the bare membrane models are necessary. Therefore, for all the calculations in the bare membrane models, the diffuse boundary conditions were applied.

On the other hand, in the C18-modified low-density (2μmol/m^2) system, the diffusivities of both species statistically were not much different than the case of regular specular boundary conditions. We conclude that the C18-modified (2μmol/m^2) system was dense enough so that collisions with chains were more. Therefore, the diffuse boundary conditions were not included in the calculations for the systems that contain chains.

4.3.2 Density Effects

Since we are reporting diffusivities in the Henry's Law regime, it is important to ensure that all the model systems are behaving as infinitely dilute with respect to penetrant densities, i.e., that the penetrants do not interact with each other. We now demonstrate that we are operating in such a regime. The diffusivity of ten propane molecules in 5 nm-bare membrane is calculated at different densities by varying only the box lengths, L_x,L_y (in x and y directions). The pore size (box length in z-direction) was kept constant. The propane molecules are chosen, because a propane molecule is a lot larger than a nitrogen molecule, and at the same density, nitrogen molecules would have weaker interactions with each other in comparison to propane molecules. If we find the density that satisfies the dilute conditions for propane, that density is also applicable for the systems with nitrogen molecules.

The results are illustrated in Figure 4.3. After examining the plot, it was observed that if the box length is greater than 50 σ(sigma), the data reach a plateau where the propane diffusivity remains constant within statistical error as the box lengths increase.

Therefore, the diffusivity calculations in all the bare membrane models were computed in the presence of 10 penetrants with the box lengths of 100 σ in *x* and *y* directions.

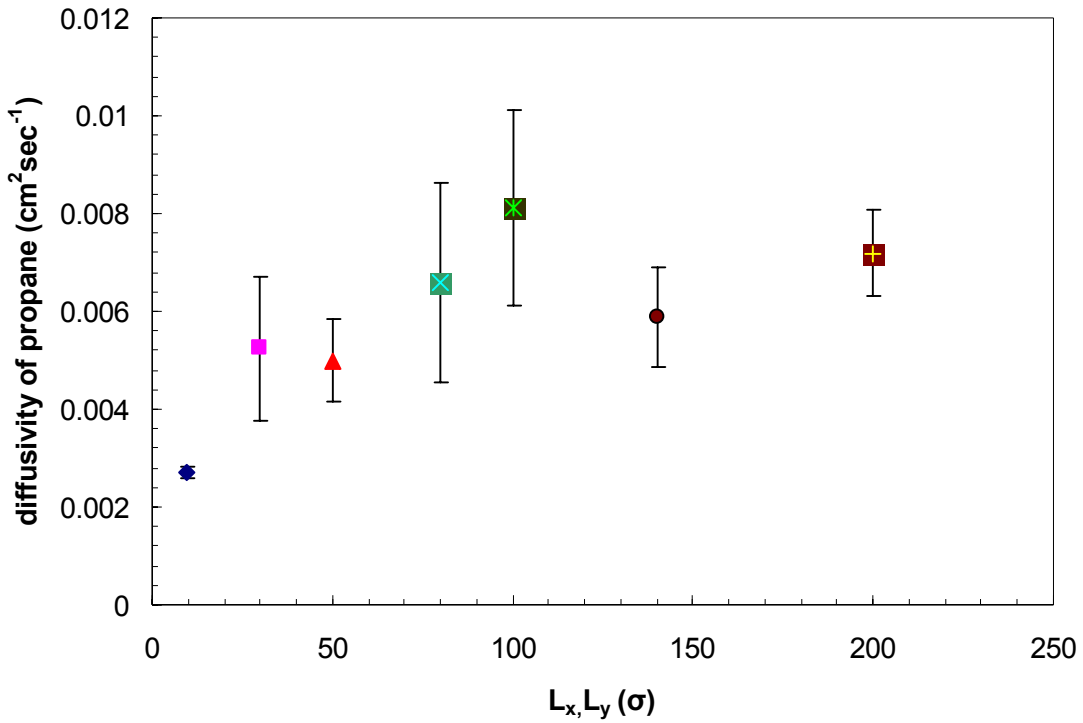

Figure 4.3 Propane diffusivity as a function of the box lengths (Lx,Ly(σ)).

In the case of the model systems that contain chains, this condition is satisfied for each penetrant differently. In order to make model choices for the calculations that involve nitrogen penetrants in the chain systems, the diffusivity of one versus ten

nitrogen molecules in the same membrane model are compared. In addition to the diffusivity calculations in section 4.4.2, the diffusivity of one nitrogen penetrant (no DBC present) in the C18-modified membrane model (2μmol/m2) is obtained. The box size remained constant which is mentioned in section 4.2, *Lx,Ly*=30.077 Å (9.5 σ). The both results and the standard deviations (σ) are given in Table 4.2.

Table 4.2 Comparison of the nitrogen diffusivity in the C18-modified (2μmol.m^{-2}) membranes.

	Dp (cm^2sec^{-1})* 10^{-2}	σ*10^{-2}
1 Nitrogen	0.358	0.0797
10 Nitrogen	0.323	0.0177

Examining the two results, we conclude that the system with ten nitrogen molecules is still in the Henry's Law limits. The solubility profiles of these systems (discussed later) supported the same conclusion. As a result, for all the calculations regarding nitrogen in a modified-membrane, this model was used.

For the calculations of propane diffusivity, a different approach was followed. Since the density was found to be an issue for this penetrant even at very low values, only one propane molecule was used for all the calculations in modified-membrane systems. The box size was set to the same size as in the calculations for nitrogen

(*Lx,Ly*=30.077 Å). This approach not only ensures that there are no penetrant-penetrant interactions, but also it makes it easier to build the initial configurations for the chain systems. However, in the diffusivity calculations, in order to obtain a good statistics, the total time of the simulations for the propane molecules was extended ten times more than for the nitrogen.

4.4 Property Predictions

4.4.1 Solubility Calculations and Segmental Solubility Profiles

The Henry's Law solubility of each penetrant was calculated in different organic-inorganic composite materials (bare, C8, C12 and C18). In very low concentration limits (assumption of "ideal gas" and "ideal sorbed" phase), the solubility constant *S* can be defined in units $cm^3(STP)cm^{-3}bar^{-1}$ as:

$$S = \frac{T_s}{P_s T}\left\langle \exp\left(-\beta \Delta U\right)\right\rangle_{NVT} \tag{4.7}$$

where T_s and P_s denote the standard temperature and the pressure (273.15 K and 1.013 bar, respectively), ΔU is the change in the potential energy when a penetrant is being inserted to the system. The quantity $\left\langle \exp\left(-\beta \Delta U\right)\right\rangle_{NVT}$ is evaluated by using the Widom insertion technique.[117] In the Widom insertion technique, "test" particles are inserted at random places in the matrix and the interactions of these particles with the pore walls and the organic substrate are calculated. No other penetrant molecules were present during these insertion processes, so the conditions were consistent with Henry's Law.

Since the system was confined in the *z*-direction, it was divided into bins parallel to the walls to produce solubility "profiles" across the pore. The macroscopic Henry constant was the average value over this profile. We carried out at least 2.56 10^9 insertions at 298 K temperature throughout the simulations and averaged the solubility results over the bins and the number of insertions.

4.4.2 Diffusivity Calculations

In order to evaluate the diffusion coefficients, the mean square displacement (MSD) of the penetrants was calculated. MSD is related to the diffusivity coefficient in *d* dimensions as follows:

$$D = \frac{1}{2d} \lim_{t \to \infty} \frac{d \left\langle r(t) - r(0) \right\rangle^2}{dt} \tag{4.8}$$

For every penetrant molecule, the MSD was measured as a function of time. In order to improve the statistical accuracy, two features were included in the simulations. First, instead of taking one time origin, multiple time origins were created. For this purpose, the configurations of the particles were saved every 1.0 ps at 298 K along the trajectory as time origins. Second, in some cases multiple molecules (nitrogen) were used, and an arithmetic average over multiple particles was taken. Of course, to remain in the Henry's Law regime, as discussed in detail in section 4.3.2, it was verified that the multiple particles do not affect each other. The length of the total runs for the systems with nitrogen molecules was about 5 ns and the systems with propane molecules was about 50 ns. The MSD of each penetrant was plotted as a function of time *t*. *D* is

calculated from the slope of the curve in the linear regime. In the case of composite materials (confined systems), since the presence of the walls prevents the motion in the *z*-direction, the MSD curve for motion in this direction was observed to "flatten out" (attain a slope of zero) on a time scale that was significantly shorter than was required to reach the linear regime in the other two directions. Therefore, the displacements were calculated only in the non-confining (*x* and *y*) directions and a value of *d*=2 was used in Eqn. (4.8) to reflect the fact that the long-ranged diffusivity occurs in two dimensions.

4.4.3 Permeance and Selectivity Calculations

The diffusivity and solubility results were used to compute the permeance, the diffusivity, solubility and the overall selectivity of nitrogen and propane. As pointed out earlier in section 2.2, the permeance of a penetrant A can be expressed as a product of solubility and diffusivity of the penetrant:

$$P_A = D_A S_A \tag{4.9}$$

then the overall selectivity of penetrant A over penetrant B is:

$$\alpha_{A/B} = \frac{P_A}{P_B} = \frac{D_A S_A}{D_B S_B} \tag{4.10}$$

The overall selectivity expression can be considered as a combination of the solubility and diffusivity selectivity. Hence, we can obtain the diffusivity and the solubility selectivity of A over B, respectively, by

$$\alpha_{A/B}^{D} = \frac{D_A}{D_B} \tag{4.11}$$

$$\alpha_{A/B}^{S} = \frac{S_A}{S_B} \tag{4.12}$$

4.4.4 Segmental Density Profiles

The permeation of the molecules in the polymer (organic) matrix is affected by the local packing of the matrix. Therefore, the density profiles for the organic layers (chains) that were attached on the inorganic surface were measured. The segmental density profile provides useful information about the packing of the organic layer across the pore and it was measured by the following approach, the pore was again divided into bins in the *z*-direction and the number of organic segments in each bin was measured throughout the simulation. Furthermore, to gain a better insight, we evaluated the population of the each chain segment separately. The bin widths were taken as 0.2 Å for 30; 0.33 Å for 50 and 100 Å pore sizes.

4.5 Results

4.5.1 Effects of Alkyl Chain Length and Pore Size

Selectivity and permeance are two important factors in measuring membrane performance. Therefore, selectivity-permeance plots for propane/nitrogen separation on different size of surface-modified membranes are obtained from both the experimental (5 and 10 nm) and simulation (3, 5 and 10 nm) results. First, the experimental results are presented in Figure 4.4 to show the effect of chain length on the propane/nitrogen

selectivity in 5 nm surface-modified membranes (all of the experimental results are for normally hydrated substrates treated with alkyltrichlorosilanes).

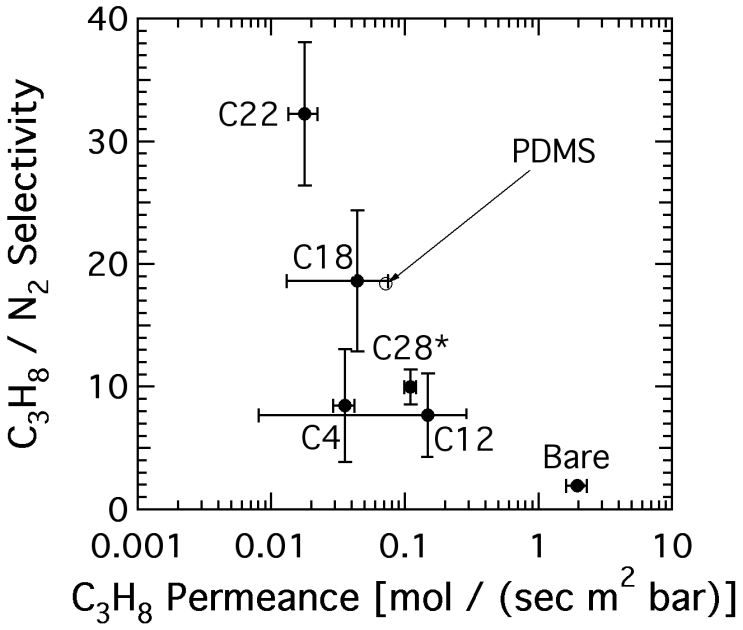

Figure 4.4 Propane/nitrogen selectivity as a function of propane permeance in 5 nm membranes from Javaid et al.[1]

The plot shows that propane permeance decreased by as much as 2 orders of magnitude upon surface modification, while selectivity increased significantly.

Furthermore, the permeance and selectivity were correlated with the chain length used. Although the results for the shorter (C4 and C12) chains were statistically indistinguishable, the longer (C18 and C22) chains exhibited significantly better performance. It is quite evident that increasing the chain length increases the propane/nitrogen selectivity. In fact, increasing the chain length beyond C12 appears to greatly increase selectivity without much loss in permeability; this is of course a very desirable situation. Although it appears that the results for C28 are anomalous, they are consistent with its branched structure. C28 alkyl group was a geminal branched chain with the longest branch being C14; a selectivity somewhere between that of the C12 and C18 membranes is therefore not surprising. A data point from the literature[127] for a polydimethylsiloxane (PDMS) membrane is shown for comparison.

Figure 4.5 summarizes the effects of pore size by comparing the performance of the 5 nm and 10 nm membranes for three different treatments (untreated, C12, and C18). The 5 nm substrates produce more selective and less permeable membranes than the 10 nm substrates for any given treatment, with the effects becoming more pronounced for the larger chain lengths.

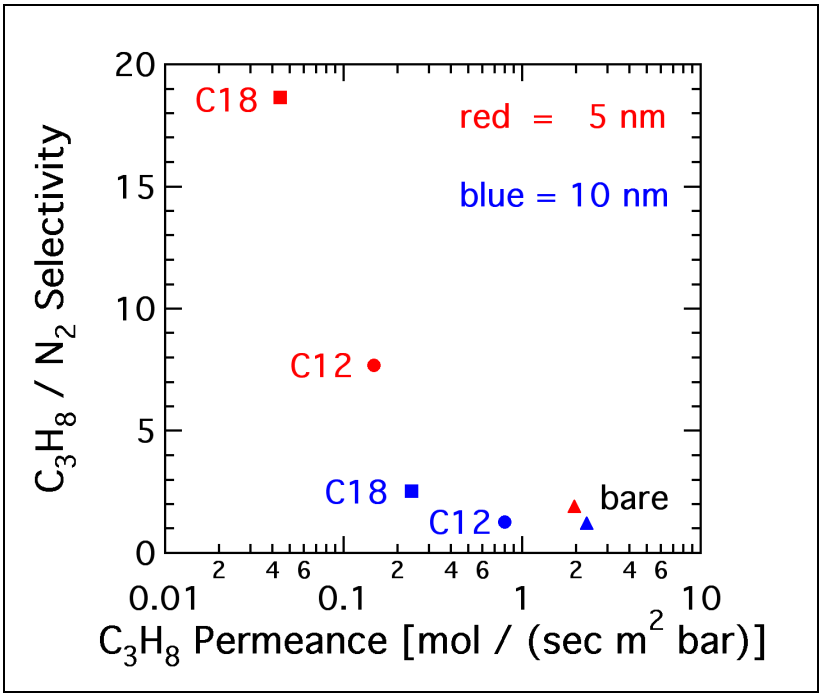

Figure 4.5 Comparison of performance in 5 nm and 10 nm membranes. Circles represent bare membranes, squares represent membranes treated with C12 chains and diamonds represent membranes treated with C18 chains from Javaid et al.[1]

The simulation results for the propane/nitrogen selectivity versus propane permeance for different chain lengths in 5 nm membranes are shown in Figure 4.6. All the simulation results in this section were for one surface density (4μmol/m^2). This plot may be compared with the experimental plots in Figure 4.4. Because of the approximations in our model system, we do not see perfect quantitative agreement. However, we do have qualitative agreement with the experimentally observed trends.

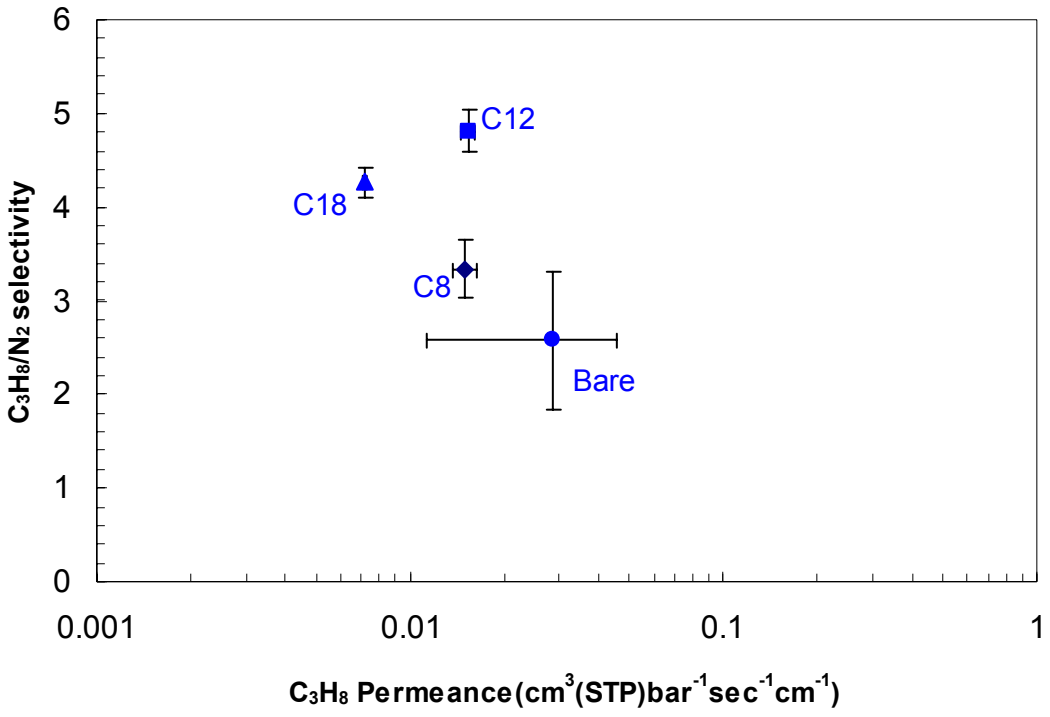

Figure 4.6 Propane/nitrogen selectivity as a function of propane permeance in 5 nm membranes (the simulation results).

The most obvious common feature between the experimental and simulation data is that the introduction of attached chains results in increased selectivity and decreased permeability. Furthermore, if we focus on the chain length effect, we see that the selectivity is enhanced as the chain length is increased. However, in the simulation results, the differences in the overall selectivities for the chains (C8, C12, and C18) that we used are not as pronounced as in the experimental results. We believe that is a consequence of the fact that the C18 alkyl-chains are not long enough to span the 5 nm-

pore completely. However, in the case of 3 nm-membrane models, the C18 chains were able to span throughout the pore. As a result, as it is seen in Figure 4.7, the selectivity is increased more than twice as much as in the 5 nm pore sizes. The comparison of these simulation results obtained from C18-modified, different pore sized (3, 5 and 10 nm) membranes are presented in Figure 4.7.

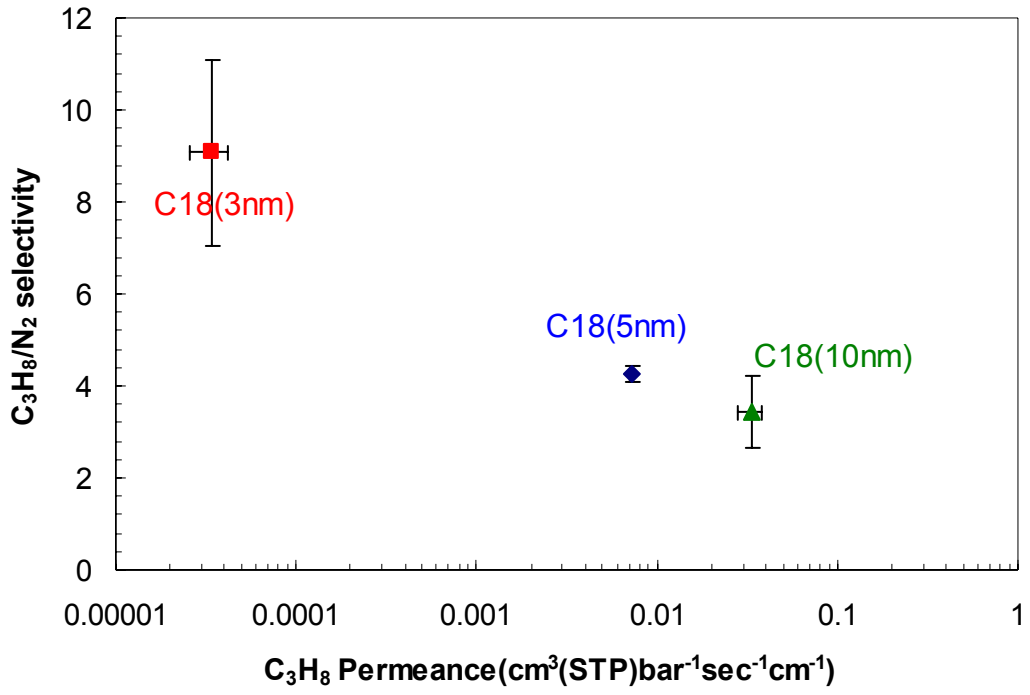

Figure 4.7 The simulation results for C18-modified membranes in different pore sizes (3, 5 and 10 nm).

These results suggest that if the chain length is long enough to span the pore (or the pore is small enough to be filled with the particular chain lengths), the selectivity increases in the favor of the larger species.

It is also interesting to see the parallel between experiment and simulation in the effects of pore size. The simulation results in Figure 4.8, including bare and C18-modified membranes in 3 different pore sizes (3, 5 and 10 nm), may be compared to the experimental results in Figure 4.5.

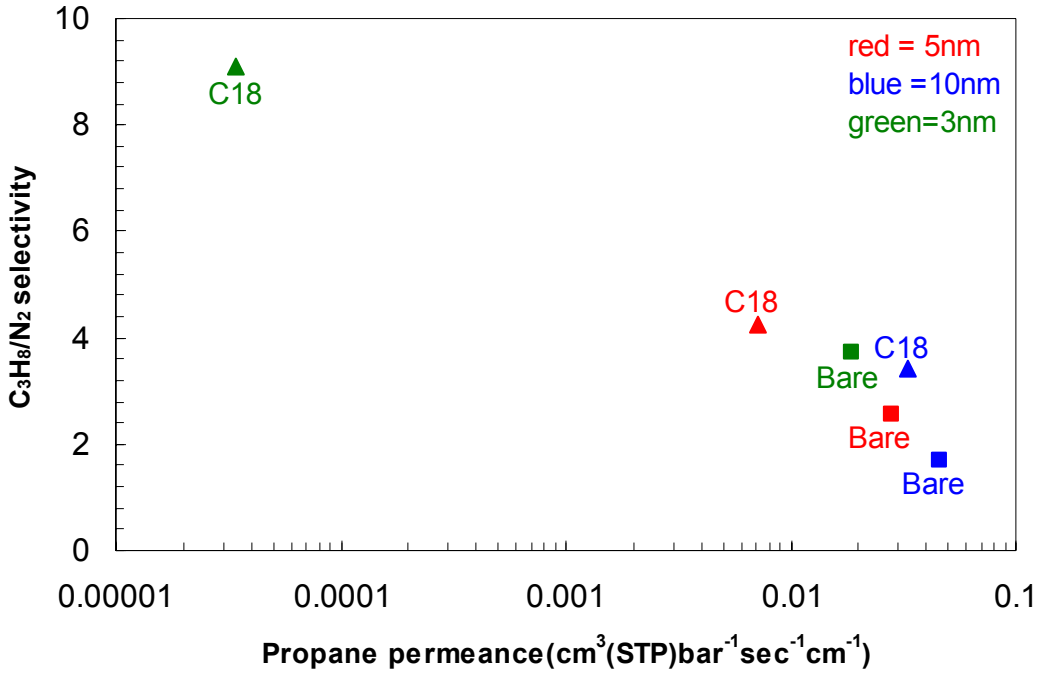

Figure 4.8 Comparison of the performance of 3, 5 and 10 nm, treated (C18) and untreated (bare) membranes from molecular simulations.

In the simulations, the larger (5 and 10 nm) pores have generally lower selectivities and less sensitivity to chain length than the smaller (3 nm) pore. This is also true for the experimental results in Figure 4.4 and Figure 4.5, although the "large" and "small" pore sizes were 10 nm and 5 nm, respectively. This quantitative discrepancy may be due to inaccuracies in the experimental pore size estimation, which is discussed in section 4.2. Another possible explanation is the ability of the trifunctional chlorosilanes to form polymeric networks and bridge across pores even larger than 5 nm (a phenomenon that was not captured in the molecular models).

4.5.2 Effects of Surface Density

Another parameter of interest is the surface coverage. In the experiments, different surface coverages are obtained by varying the hydration state of the alumina substrate prior to treatment. All of the experiments were done with the C18 trichlorosilane, OTS. Propane and nitrogen permeance, ideal selectivity, and XPS elemental analysis data (from surface scan, not depth profiling) for the bare and OTS modified membranes are given in Table 4.3. The XPS data are reported in terms of molar percentage of carbon and silicon; the remainder of the XPS signal was from Al and O in the expected ratio.

Table 4.3 Propane and nitrogen permeance, ideal selectivity, and molar percentage of elements as detected by XPS, for bare and OTS-treated membranes. For the OTS-treated membranes, data are given for three different pretreatment hydration states. Standard deviations are given in parentheses.[1]

Degree of Hydration	Permeance (mol sec^{-1} m^{-2} bar^{-1}) C_3H_8	N_2	Selectivity C_3H_8/N_2	Carbon mol%	Silicon mol%
Bare	1.04 (0.18)	0.62 (0.087)	1.68 (0.12)	12.6 (2.7)	0.0
Normally hydrated	0.016 (0.0047)	0.0008 (0.0002)	19.9 (4.3)	73.4 (8.2)	5.1 (0.39)
Dehydrated	0.0097 (0.0056)	0.0023 (0.0016)	4.36 (0.45)	47.0 (9.3)	4.3 (1.3)
Superhydrated	0.68 (0.40)	0.52 (0.28)	1.23 (0.21)	68.0 (6.5)	6.5 (1.2)

The normally hydrated (NH) membranes exhibited the highest propane/nitrogen selectivity and also the highest carbon content. The selectivity for the dehydrated (DH) membranes was significantly lower than the selectivity shown by the NH membranes, due to a combination of factors; the propane permeance for the DH membranes was about 40% smaller than that for the NH, while the nitrogen permeance was a factor of 3 higher.

The simulation results that summarize the surface coverage effects are given in Figure 4.9. In the plot, “4” and “2” symbolize 4 and 2 $\mu mol.m^{-2}$ surface coverage (chain density), respectively.

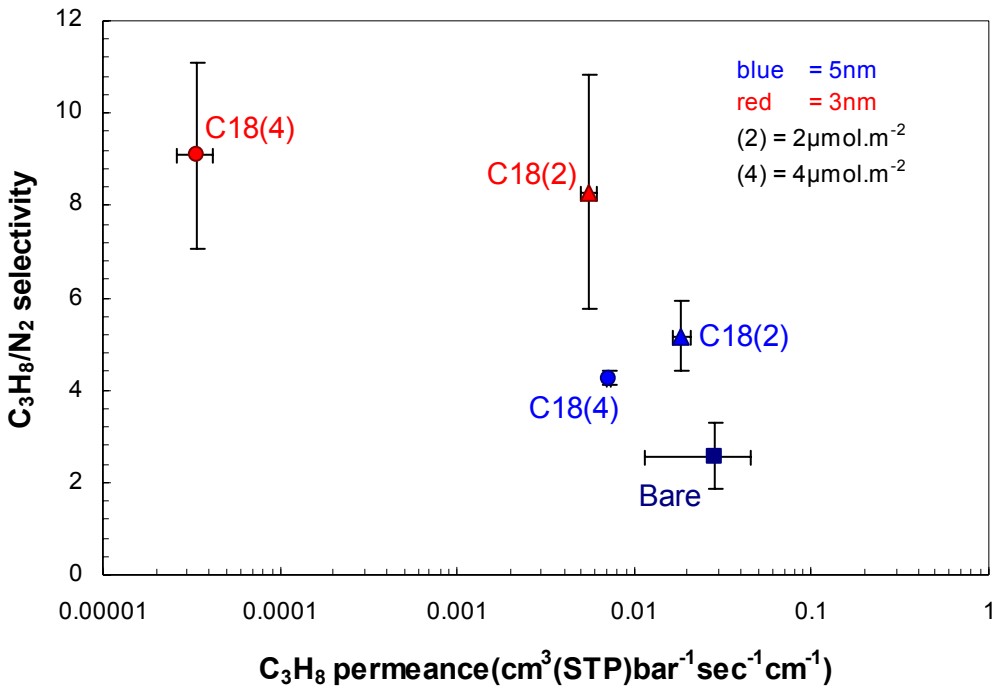

Figure 4.9 The simulation results for comparison of the surface coverage effects in 5 and 3 nm, C18-modified membranes.

The result from the experimental data was not reflected in any of the simulation results. In contrast, in the simulations, decreasing the surface coverage resulted in a significant increase of propane permeance, and either a small increase or statistically very similar results in the selectivity. The lower surface coverage allowed both penetrants to diffuse faster in the pore, to roughly the same degree.

A lower surface coverage could be expected to result in both an increased diffusivity (higher free volume) and a decreased solubility (fewer van der Waals

interactions); the former effect would tend to increase the permeance while the latter would tend to decrease it. Furthermore, the relative importance of these two effects would depend on the gas species; one might expect a lighter molecule to be more affected by the increased diffusivity, while a heavier molecule would be more affected by the decreased solubility. Based on this rationale, knowing exact surface coverage becomes more important for comparison of the experimental and simulation results regarding the surface coverage effects. Since we do not have the exact experimental value for the surface coverage at present, the comparison of the experimental and simulation results, and drawing a conclusion becomes harder. Therefore, studying the performance of the membranes in a wide range of surface coverages may be a practical step to elucidate why the two results are in disagreement. They may be the results of two different surface coverages. Furthermore, in reality, the possibility of the trifunctional chlorosilanes to form polymeric networks may cause differences between the two results, since the molecular simulations do not capture this phenomenon.

4.5.3 Further Analysis

All the simulation data is summarized in Figure 4.10 for the further analysis. We can also examine the individual components, diffusivity and solubility, that contribute to the permeability. Table 4.4 gives detailed data for the solubility and diffusivity of each penetrant in the various models as well as the permeance and selectivity results for each model material. The permeance and selectivity results are calculated as described in section 4.4.3.

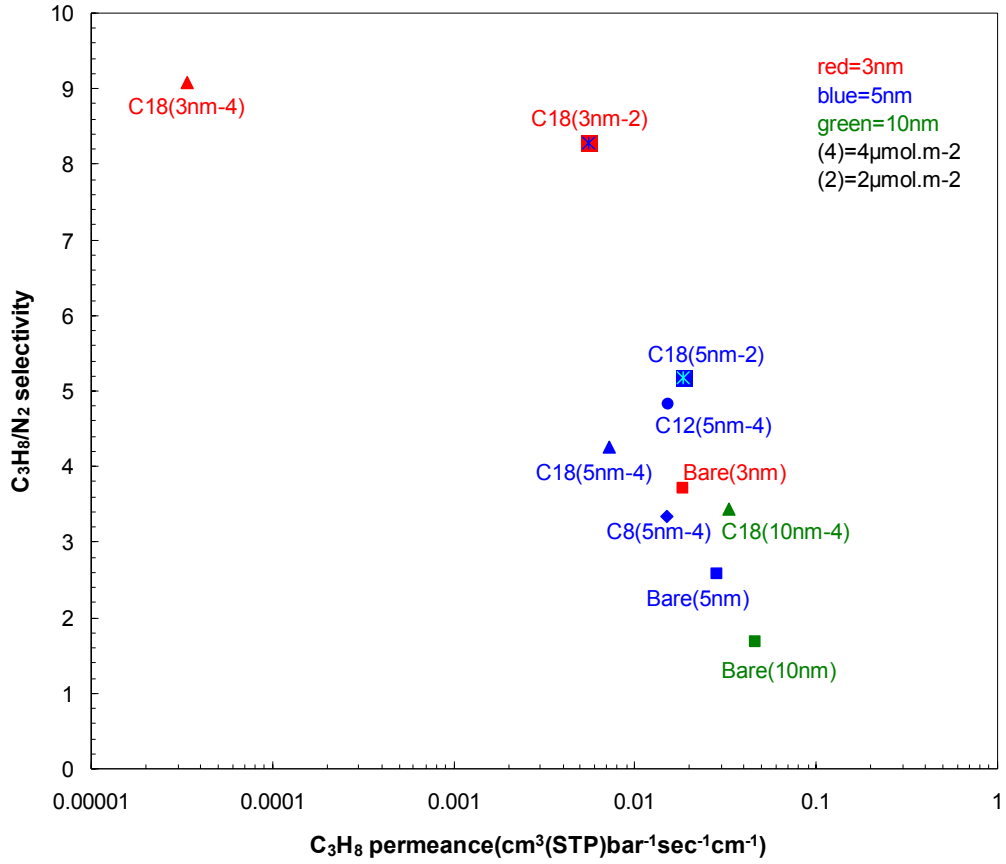

Figure 4.10 Summary of all simulation results.

Table 4.4 Summary of diffusivity, solubility, and permeability data from the simulations. D and S represent the diffusivity and solubility, α_D, α_S and α_P are the diffusivity, solubility and overall selectivity, respectively.

Chain Length	Pore Size (nm)	Surface Density ($\mu mol/m^2$)	Gas Species	D (x 10^2) ($cm^2 sec^{-1}$)	α_D (D_P/D_N)	S [cm^3(STP) cm^{-3} bar^{-1}]	α_S (S_P/S_N)	P [cm^3 (STP) cm^{-1} bar^{-1} sec^{-1}]	α_P
bare	5	-	Propane	1.27	0.7110	3.4927	3.3565	0.0442	2.3866
			Nitrogen	1.78		1.0406			
C8	5	4	Propane	0.204	0.4339	7.3655	7.6792	0.0150	3.3321
			Nitrogen	0.469		0.9591			
C12	5	4	Propane	0.155	0.4492	9.8899	10.747	0.0154	4.8280
			Nitrogen	0.346		0.9202			
C18	5	4	Propane	0.0762	0.3654	9.4104	11.685	0.0072	4.2697
			Nitrogen	0.209		0.8053			
C18	5	2	Propane	0.1320	0.4114	13.995	12.643	0.0184	5.2014
			Nitrogen	0.320		1.1069			
C18	3	4	Propane	0.00043	0.2782	7.797	32.639	0.0000338	9.0798
			Nitrogen	0.00156		0.2388			
C18	3	2	Propane	0.0199	0.3778	27.869	21.896	0.0055421	8.2717
			Nitrogen	0.0526		1.2728			
C18	10	4	Propane	0.5919	0.52373	5.6070	6.553	0.033188	3.4318
			Nitrogen	1.1302		0.8557			

Both Table 4.4 and Figure 4.10 support the idea that we increased the solubility of the propane and decreased the diffusivity of both penetrants, upon adding chains as compared to bare membranes. In the 5 nm pore, the reduction of the diffusivity of the propane is much higher than that for nitrogen, which leads to a lower diffusivity selectivity. This counterbalances the effect of increasing the solubility of the propane and results in little improvement in the overall selectivity. On the other hand, in the smaller pore (3 nm), the increase in the solubility selectivity was much higher and more than enough to compensate for the decrease in the diffusivity selectivity. Lowering the surface density moved the selectivity in the favorable direction by not only increasing the diffusion of the propane molecules (with that also permeances), but also maintaining the diffusivity selectivity around the same value as in the 4 $\mu mol.m^{-2}$ case. By looking at the overall data, we conclude that, in the 3 nm pore membrane, we filled the pore or closed the pore mouths by attaching the C18 alkyl chains. Hence, we helped the separation process to change in the favor of the more soluble molecule, which is the propane in this case.

In order to get a further molecular level understanding, we analyzed the density profiles of the chains along the pore and the corresponding solubility profiles of the penetrants (see Figures 4.11 through 4.14). The density profiles for the different chain lengths and pore sizes (Figure 4.11 and Figure 4.13) supported the conclusion that the chains spanned the entire pore width only in the case of the longest chains (C18) and the smallest pore (3 nm). This is also reflected in the solubility profiles shown in Figure 4.12 and Figure 4.14. The profiles indicate why the solubility-selectivity was so high for the

C18 chains in 3 nm pores (Table 4.4). Snapshots from the simulations in Figure 4.15 and Figure 4.16 also visually confirm the same conclusion.

4.6 Conclusions

We achieved good qualitative agreement with experiment in several respects, including the improvement in the overall selectivity of the membrane and decrease in the permeance when increasing the chain length. Conditions under which chains span the pore yield the best improvement in the overall solubility selectivity.

However, if the system is filled at too high a surface density with the alkyl chains, the permeance of the penetrants will drop significantly. In order to avoid that, one can find the best surface coverage by calculating the selectivity vs. surface coverage profiles.

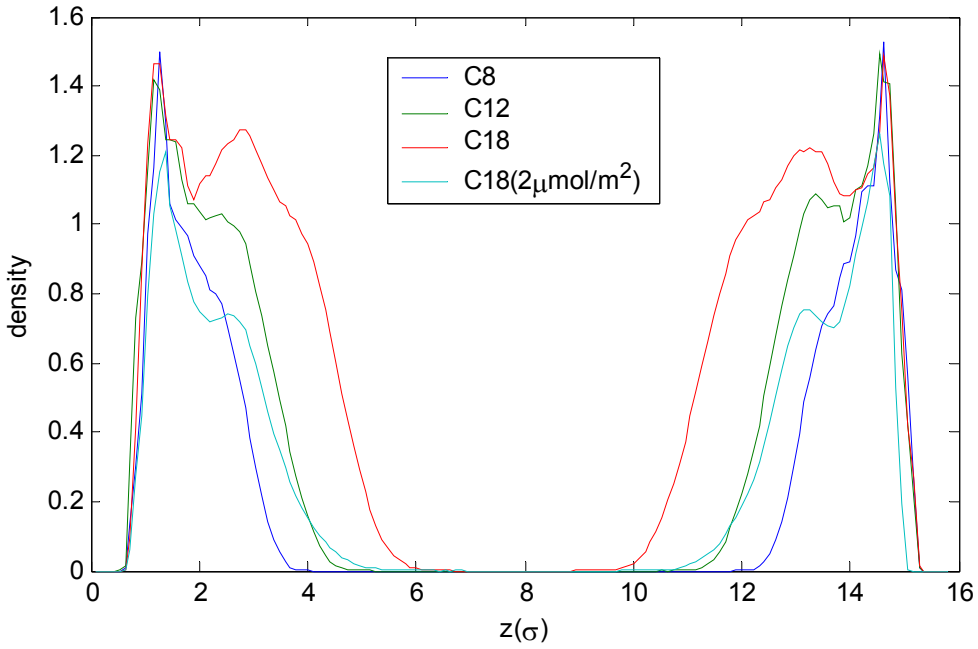

Figure 4.11 Density profiles of chains for different chain lengths in 5 nm pore (in the presence of propane).

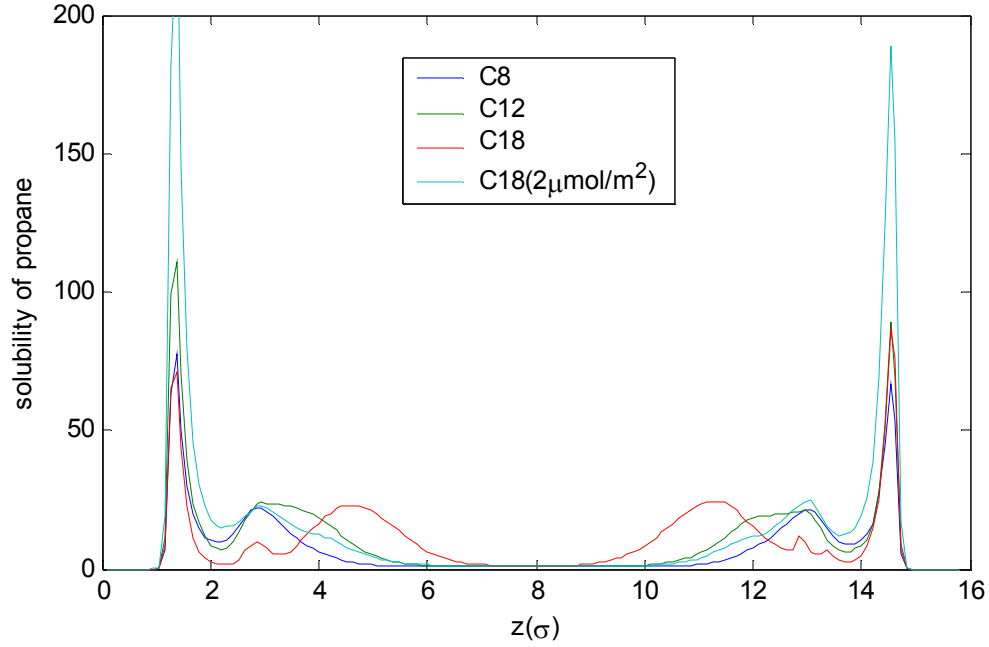

Figure 4.12 Solubility profiles of propane for different chain lengths in 5 nm pore.

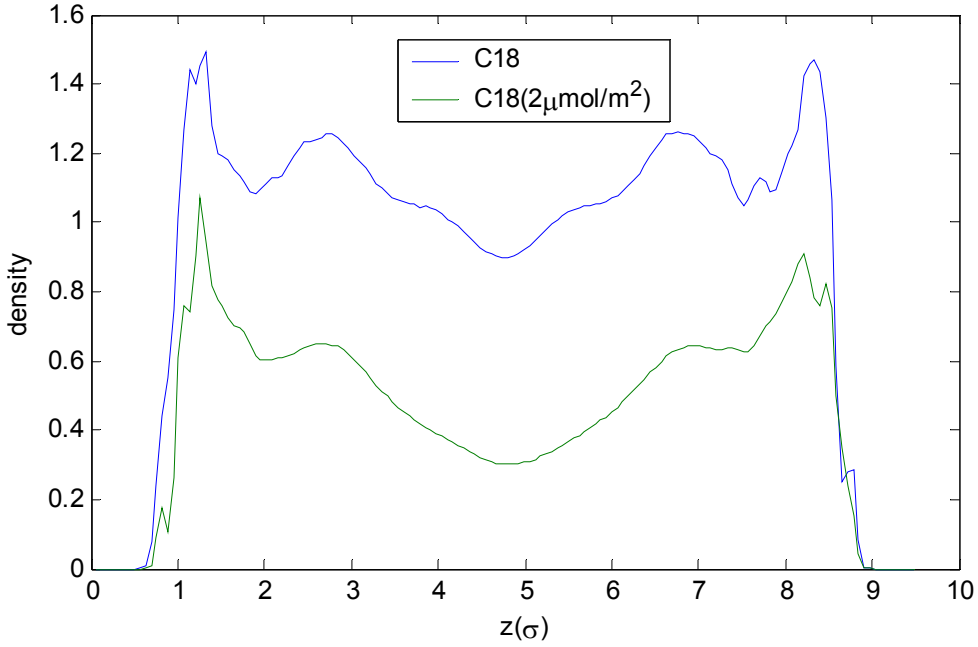

Figure 4.13 Density profiles of chains for different chain lengths in 3 nm pore (in the presence of propane).

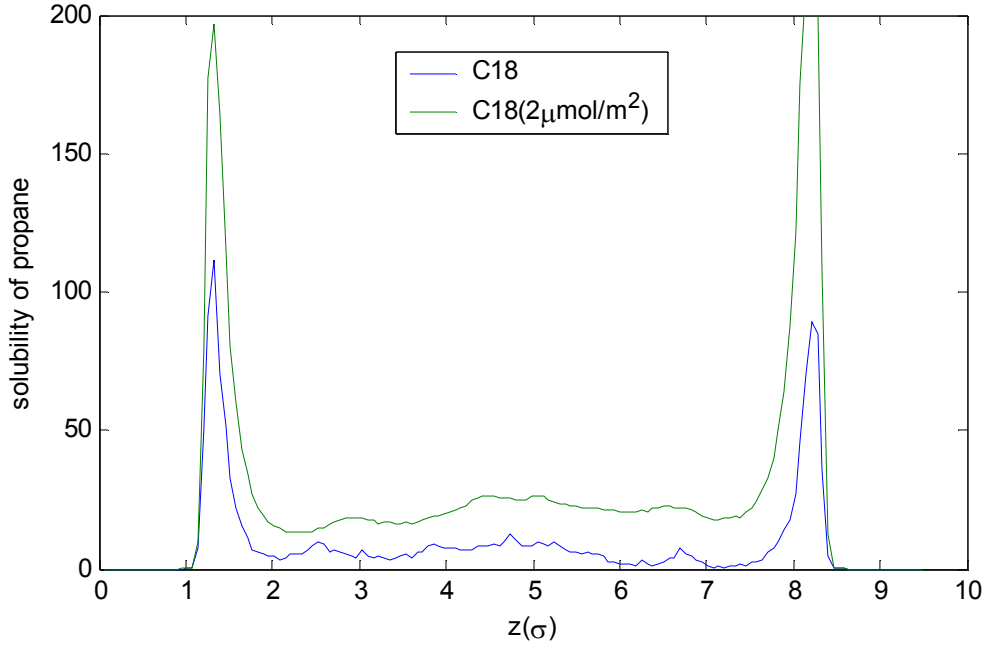

Figure 4.14 Solubility profiles of propane for different chain lengths in 3 nm pore.

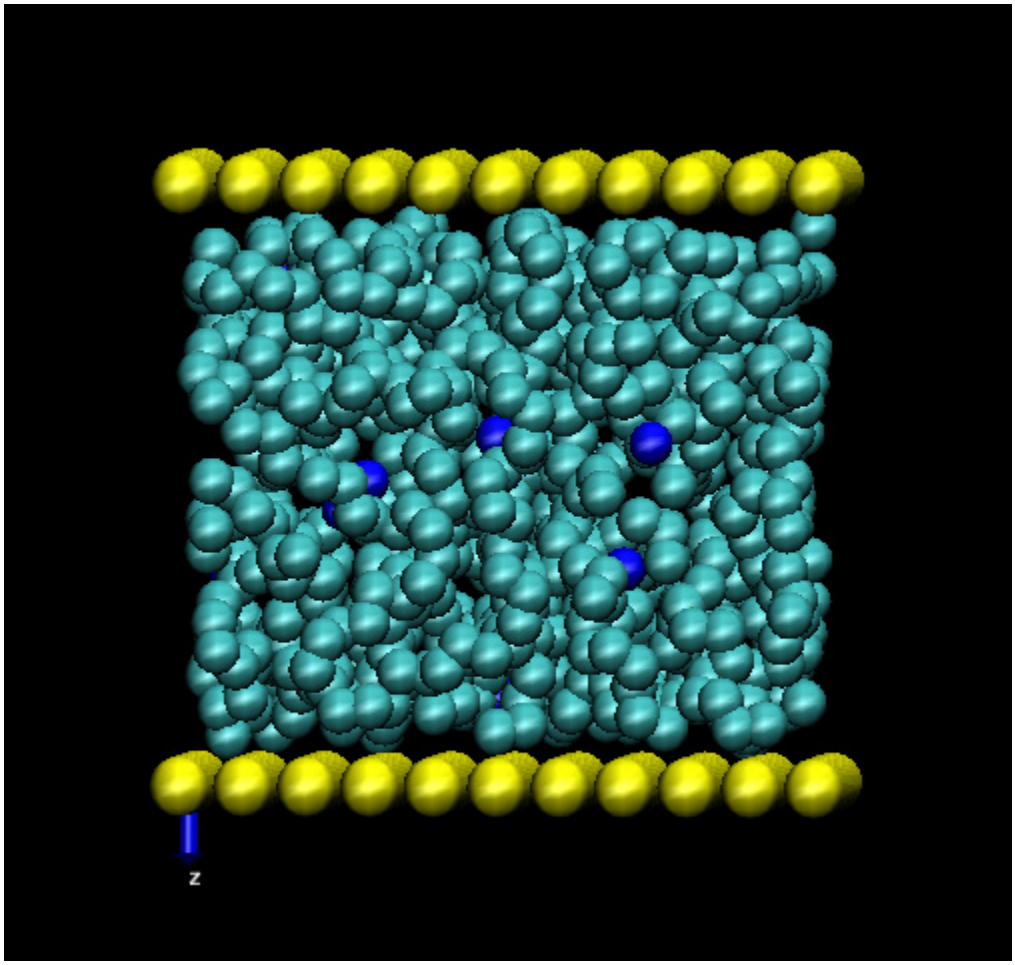

Figure 4.15 Snapshots from the simulations of nitrogen molecules in the C18-modified, 3 nm model pore.

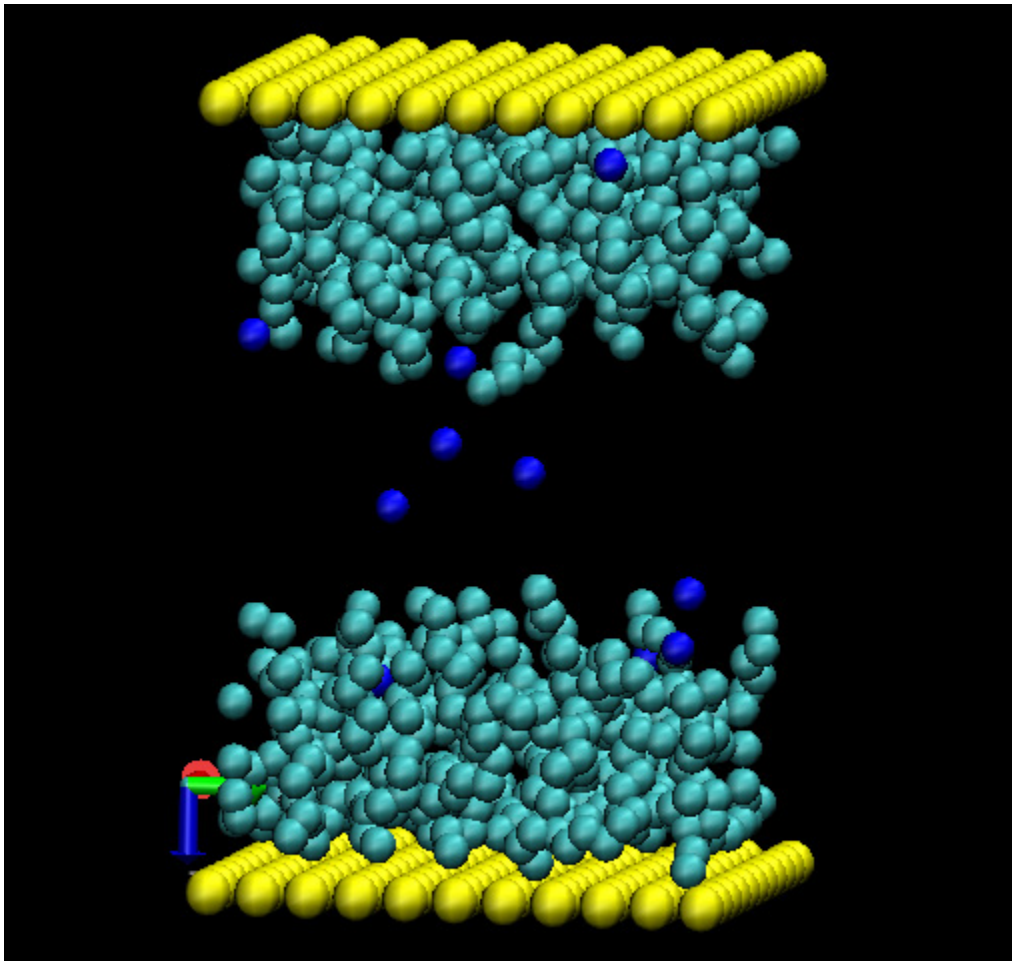

Figure 4.16 Snapshots from the simulations of nitrogen molecules in the C18-modified, 5 nm model pore.

CHAPTER V

MICRO ELECTRO MECHANICAL SYSTEMS

This chapter focuses on the study of Self-assembled Monolayers (SAMs) as coatings in Micro Electro Mechanical System (MEMS) devices. Sections 5.1 and 5.2 describe the objectives and the model systems of the study, respectively. The property calculations are explained in section 5.3. The results are discussed in section 5.4, and the conclusion is given in section 5.5.

5.1 Adhesion in MEMS

As pointed out in section 2.3, one of the novel applications of alkylsilane-SAMs is coatings for Si-based MEMs, to reduce adhesion and friction problems. Scanning force probes such as the Interfacial Force Microscope (IFM) or Atomic Force Microscope (AFM) have been used to measure the atomic scale adhesion and friction forces of SAM-coated surfaces.[8,88,128-130] However, they do not produce the more complete structural characterization that can be obtained from molecular scale simulations. Here, we present the results of extensive MD simulations of adhesion between two ordered alkylsilane SAMs at full coverage on planar SiO_2 surfaces. The main objective is to predict the extent of adhesion as a function of alkyl chain length and explain the trends in terms of molecular behavior. Furthermore, the chain structure of SAMs was investigated. The dynamics of gauche defects was particular interest. These results are compared with experimental atomic force microscope (AFM) measurements.

5.2 Molecular Models

The studied system is a model system of two opposing, silicon-based MEMS surfaces coated with alkylsiloxane SAMs. It is similar in structure to the system described for the organic-inorganic composite membranes; it is infinite in the *x* and *y* directions but constrained by two walls in the *z*-direction. However, a fully atomic model was applied here, rather than the united-atom model used in the membrane studies. Full atomic detail is important for this model because maximum-density close-packed (well-ordered) monolayers were assumed throughout the study.

A typical example of our simulation cell is shown in Figure 5.1. The models were built using a code, LAMMPS, provided by Sandia National Laboratories to make alkylsiloxane monolayers chemically bonded to atomically flat silicon oxide surfaces that is four oxygen layers thick.

For these simulations, we used the structure of the trichloroalkylsilane SAMs on SiO_2 discussed in a recent article.[34] It is assumed that two of the Cl atoms have reacted to become OH groups, and the remaining Cl atom has reacted with the SiO_2 surface forming a chemical bond (see Figure 2.1). The SiO_2 surface used is the crystalline tridymite form which is a layered hexagonal lattice composed of SiO_4 tetrahedra alternatingly pointing up and down. The lattice is cut just above the O atoms at the top of the upward tetrahedra to obtain the underlying surface, and the alkylsilane chains are bonded to these sites; the Si atom of the alkylsilane is bonded to the O atom of the SiO_2 surface.

Instead of the alkylsilane chains, the addition of H atoms to the O sites would yield a hydroxylated surface (see Figure 5.2). The lattice constant of bulk tridymite is a=5.03 Å, which gives an area per chain of 21.9 Å^2. The full coverage density (the area per chain) for the experimental studies is in the range 22-25 Å^2 [86], but full coverage is experimentally rarely achieved, particularly for short chains. Using the crystalline substrate in our simulations allows us to obtain tighter packing comparing the amorphous experimental surfaces. As a result, we can take advantage of the ability to build completely ordered structures without deposition issues and the opportunity to determine both the structure and mechanical properties simultaneously.

Because well-ordered monolayer structures are simulated, it is not expected to produce the behavior typically observed experimentally. The surfaces probed experimentally are not well ordered and contain many defects. The mechanisms are likely to be quite different than those for well-ordered systems. However, the well-defined structure we use provides a basis for understanding more complex structures containing defects, more typical of experimental systems. In addition, The AFM tips are typically large (radius ~500 Å) compared to the area of the simulated SAMs (maximum cell length ~30 Å), but contact is generally dominated by small asperities on the tip, and thus the simulated contact area is directly relevant.

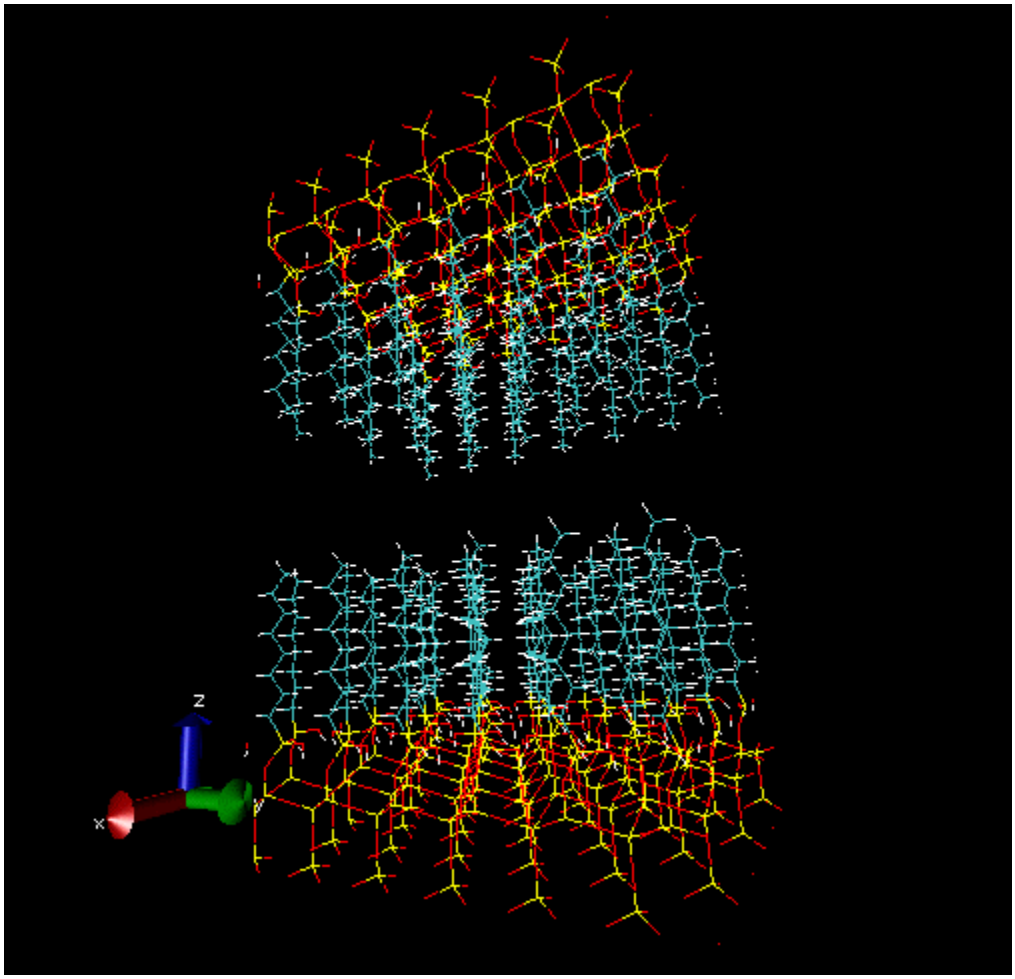

Figure 5.1 Snapshot of n=8 SAM at separations of d=10 Å (initial configurations). Silicon atoms are yellow, oxygen is red, carbon is cyan, and hydrogen is white.

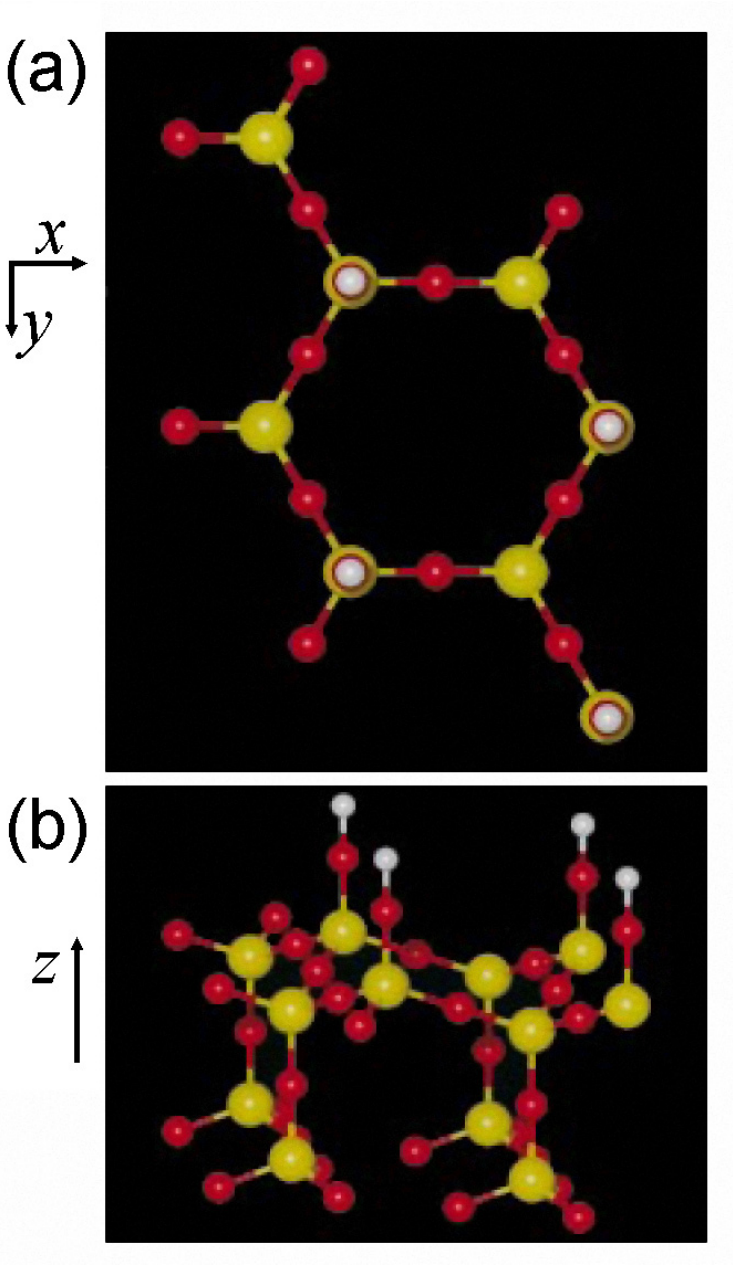

Figure 5.2 A 3D representation of tridymite showing four (2x2) cells. The colorization is as follows: O is red, Si is yellow, and H is white. (a) Projection perpendicular to surface showing hexagonal lattice. The hydroxyls form a triangular sublattice. (b) A side view. The spheres have radii a fraction of the vdW radius to facilitate visibility.[34]

The chains are initially oriented perpendicular to the oxide surface in all-trans configuration, and characterized by the number of carbon atoms in the alkyl tail, n=4, 8, and 18. The separation distance *d* between two SAMs is defined as the distance between the closest H atoms of the terminal methyl groups for chains in the all-trans configuration. At *d*=0, these H atoms would just overlap if the chains remained perpendicular to the surface in the all-trans configuration.

The published version of the MSI force field is used.[131,132] It is one of the few force fields that treats all the atom and topology types that occur in the system. This force field uses Lennard-Jones and Coulomb interactions between nonbonded atoms, class II potentials for intramolecular interactions including the bonds, bending angles, and dihedral angles, and the cross terms such as bond-angle, angle-angle. To maintain a fixed separation distance, the outermost oxygen atoms of each SiO_2 surface are constrained. To calculate the adhesion forces between two SAM-coated surfaces as a function of separation, the separation distance between the constrained oxygens is varied, and the force is calculated at each separation. The temperature in the simulations is constrained via the Nose-Hoover thermostat [99,108] at 300 K. Integration is performed using rRESPA[133] dynamics with a 1.5 fs timestep for the bond forces, a 1.5 fs timestep for the other intramolecular forces, and 0.75 fs timestep for the nonbond forces. All simulations were run by using the LAMMPS molecular dynamics code by Sandia National Laboratories.

5.3 Property Calculations

The adhesion as a function of separation, *d*, for the different chain lengths is a basic calculation of interaction between van der Waals surfaces. Figure 5.3 shows the cartoon representation of the calculation process. We moved the two surfaces towards each other; equilibrated the system at that separation, and computed the perpendicular components of the force on the upper and lower layers of constrained oxygen atoms. From these forces, we calculated the pressures at specified separations. Here, the area over which the force is applied is simply the area of the simulation cell (788.804 $Å^2$). The pressure-separation curves were obtained for various chain lengths (n=4, 8 and 18).

It should be noted that the pressures we studied are well below the hardness of the silica substrate (~ 10 GPa), implying that the substrate has no effect on the pressure measurements. Also, the simulation pressures were calculated for a system with periodic boundary conditions, which means that the chains cannot splay away from the opposite surface as can occur when an AFM is used. Thus, the experimental pressure with a tip geometry may be different.

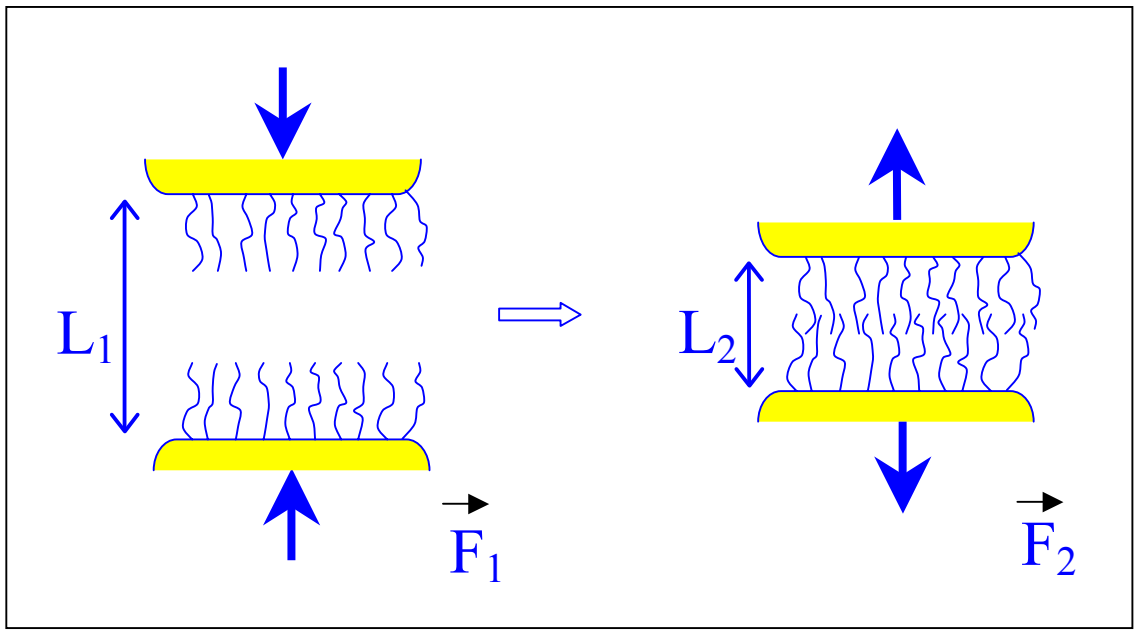

Figure 5.3 Schematic of the adhesion force calculations. *L* is fixed at each stage, with forces being calculated from the interaction parameters.

5.4 Results

The pressure-separation curves for n=4, 8 and 18 are shown in Figure 5.4. Because the pressures for all systems are very low for separations beyond 6 Å, it is not shown in the plot. The cutoff in the van der Waals interaction in our simulation is d=12 Å, hence after this point the pressure is zero. For d>0, there is a small region of attraction due to the van der Waals interaction, with a minimum of about 185 MPa, 163 MPa, and 24.5 MPa for n=18, 8 and 4, respectively. For comparison, the experimental value, calculated from the adhesive force between an OH-terminated glass IFM tip and

an alkanethiol-coated gold surface, is 230±95 MPa[134], with a large uncertainty because of the small magnitude (calculated by converting from a sphere-plane geometry to a plane-plane geometry as in the simulations). The simulation results for longer chain lengths are within this uncertainty, except the one for n=4. However, the simulation results would likely increase if we considered the van der Waals interactions beyond our interaction cutoff. Near d=0, the pressure becomes positive. As the surfaces compressed closer, further decrease in d, causes high values of the pressure since the interactions become strongly repulsive.

The pressure increases for shorter chains dramatically as the separation is decreased. Shorter chains are stiffer and have a larger repulsion for d<0 as compared to longer chains. On the other hand, in the attractive regime, the pressures are similar for all chain lengths, because the substrate and chain geometry are identical for all chain lengths. Moreover, in this region, the relationship between the wall separation and the interaction cutoff is such that the effect of chain lengths is small. Even for the shortest chains, the distance between headgroups on opposing monolayers is large enough that the contribution from the van der Waals interaction is very small, and interactions beyond this are weak long-range contributions.

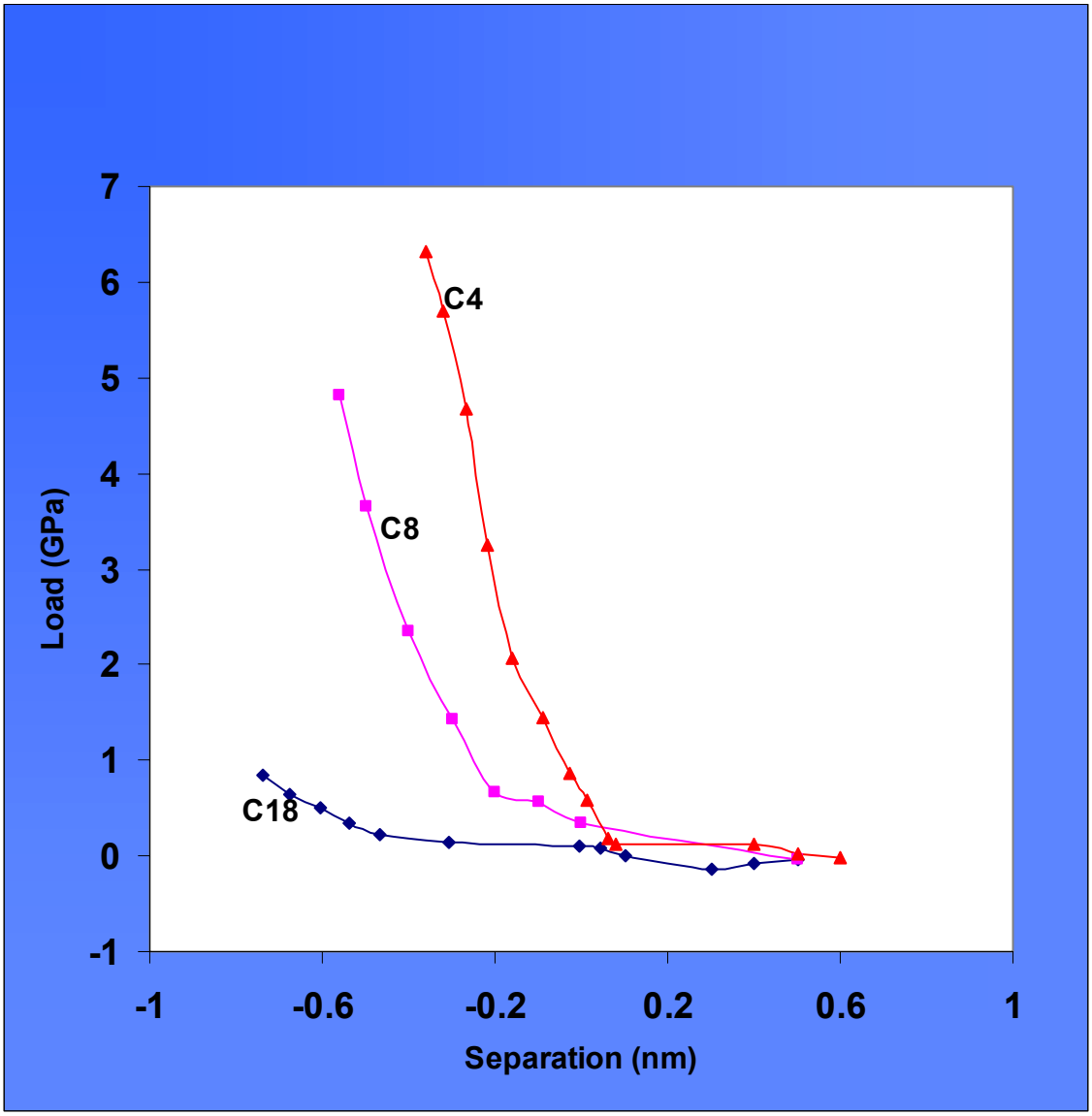

Figure 5.4 Pressure-separation as a function of chain length: *n*=4 (red triangle), *n*=8 (cyan square), *n*=18 (blue diamond).

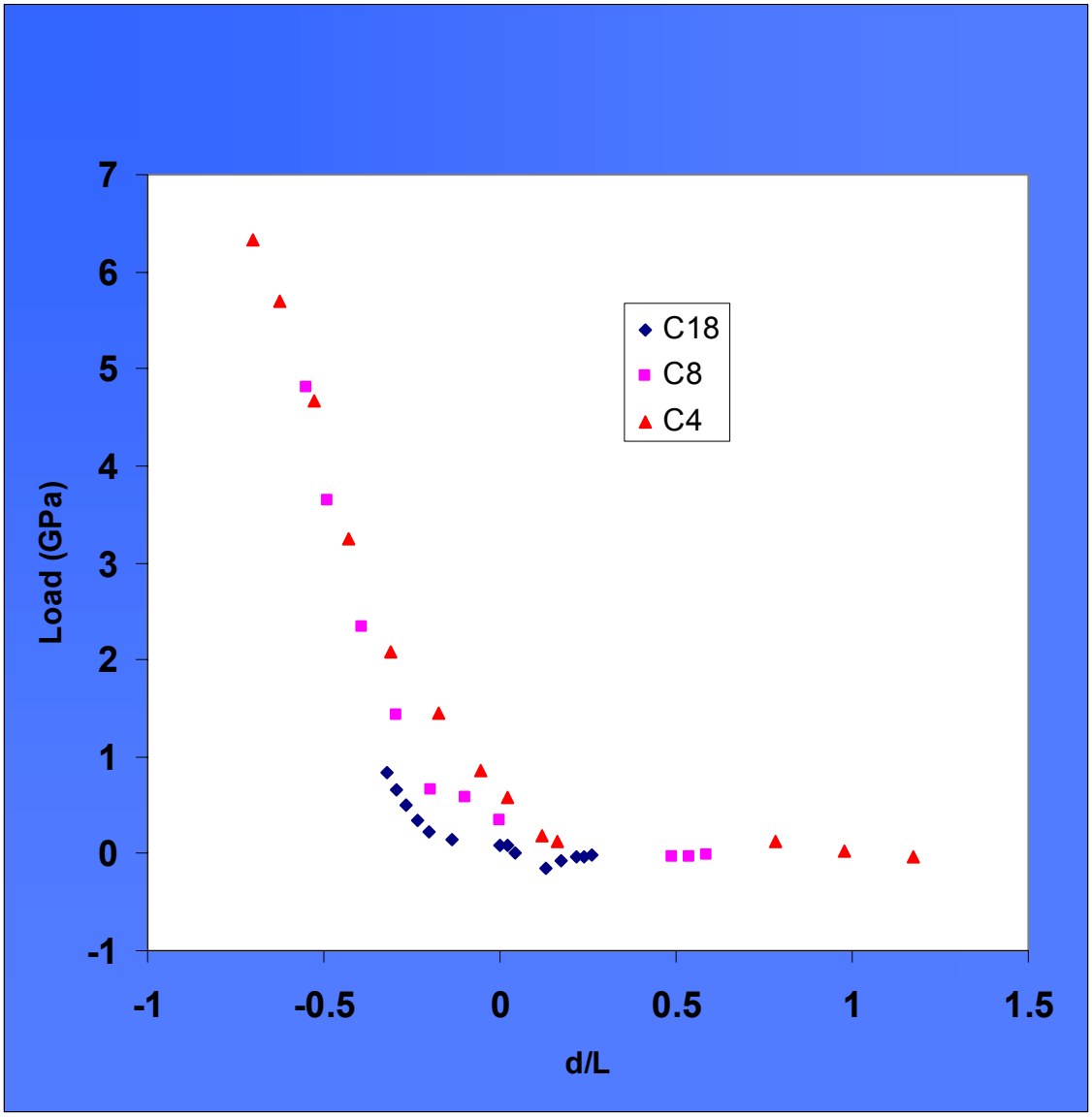

Figure 5.5 Scaled pressure-separation curves as a function of chain length, L=1.275n Å. Symbols are same as in Figure 5.4.

In order to understand the difference between the various chain lengths, the pressure-separation plots are scaled by normalizing d by the all-trans length of the hydrocarbon tail, L=1.275n (Å) (Figure 5.5)

The data is nearly overlapping at high pressures. However, at lower pressures, the curves differ for different chain lengths. For example, the longest chain length that was studied, n=18, has a relatively flat regime between d=-4.5 Å (d/L=-0.2) and 0.0 Å in comparison to the shorter chain lengths.

Images of the SAMs at d=1 Å (low pressure) and d=-6 Å (high pressure) separations are shown in Figure 5.6 and Figure 5.7. The evaluations of these images show that the chains tilt in order to compress beyond the all-trans contact configuration. Tilting allows smaller separation distances between two opposing surfaces without introducing significant overlaps and large van der Waals repulsions. Furthermore, the chains bend due to the presence of gauche defects. It was found that the longer chains tend to form gauche defects near the tail and more readily than shorter chains. In fact, this result is expected considering the relative stiffness of long and short chains. Since the longer chains have more degrees of freedom, the overall system can adopt new disturbances faster (easier) than the shorter chains. For n=18 SAMs, we do not see a sharp increase in pressure until $d\cong$5.36 Å (d/L=-0.23 Å), because the chains can initially bend as well as tilt. Nevertheless, for shorter chains the pressure increases sharply near $d\cong$0.0 Å.

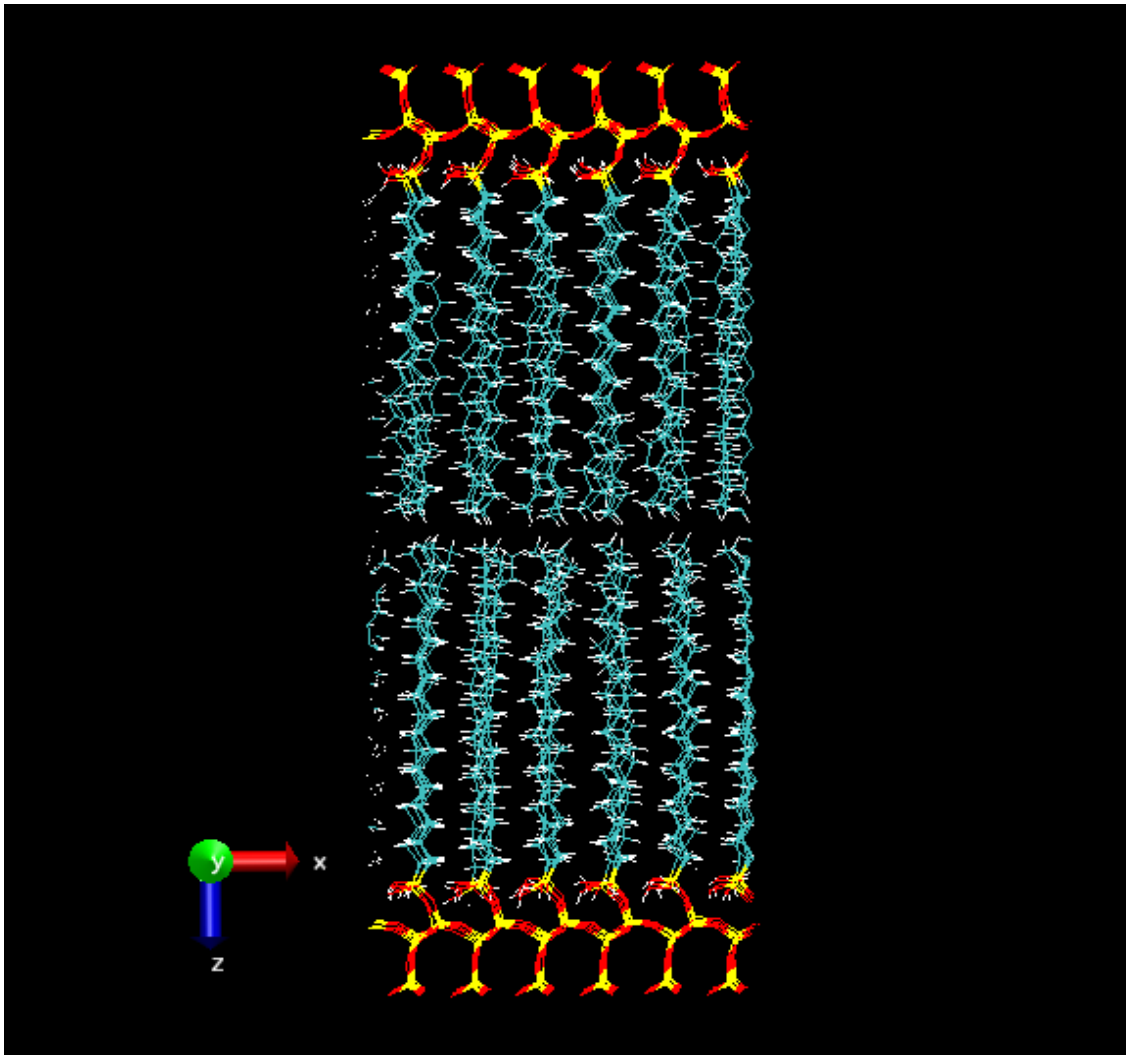

Figure 5.6 Images of *n*=18 SAMs at fixed separation of *d*=1 Å.

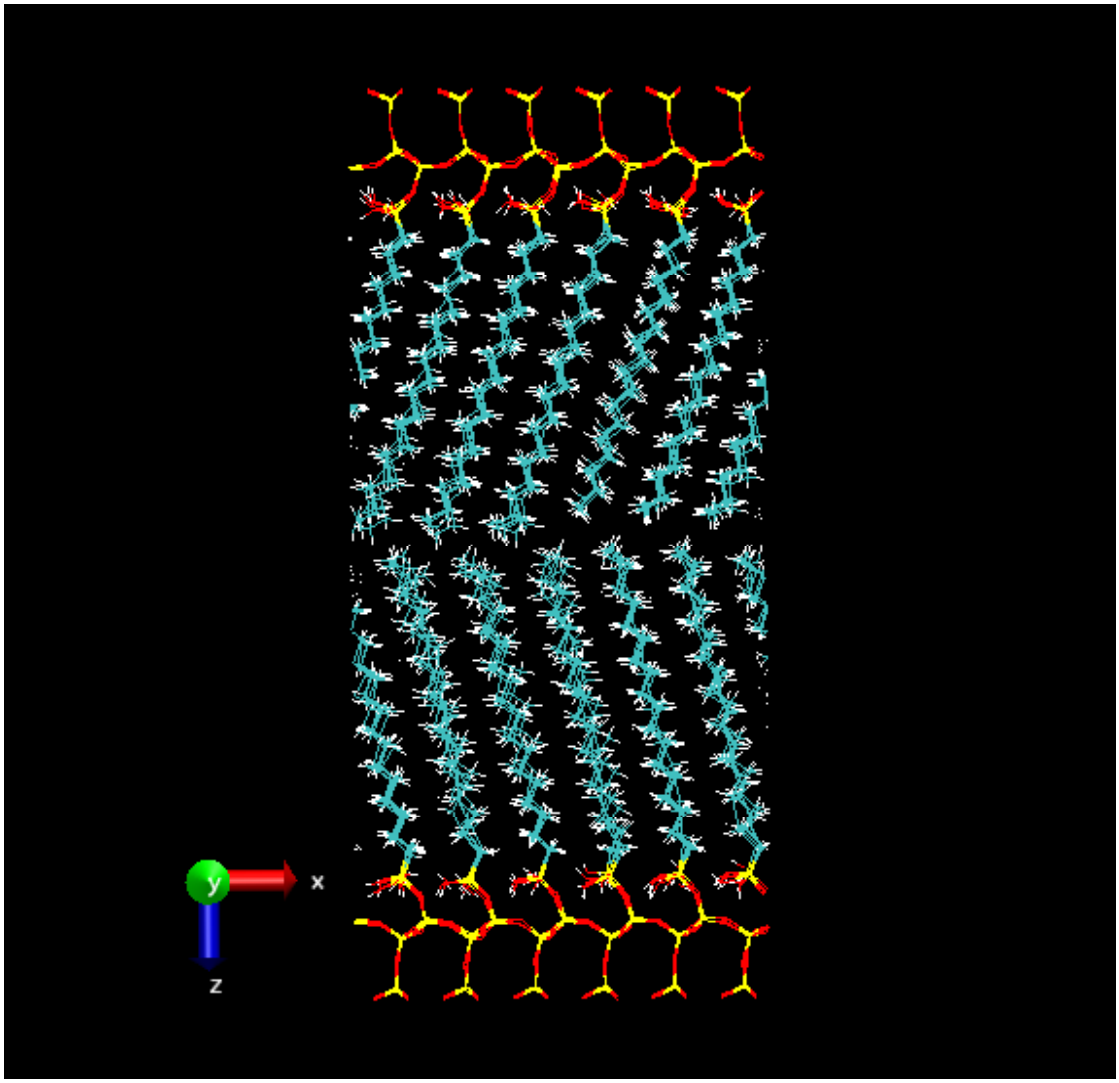

Figure 5.7 Images of *n*=18 SAMs at fixed separation of *d*=-6 Å.

5.5 Conclusion

We have studied the adhesion between ordered alkylsilane SAMs on SiO_2 substrates by performing molecular simulation. It was shown that as the chain length is increased from 4 to 18 carbon atoms, the adhesion forces between two monolayers at the same separations decreases. For n=18 SAMs, tilting and gauche defects were observed in molecular images, and these structural changes of monolayers were related to the reason for the sharp increase in pressure at lower d values in contrast with the smaller chain lengths. The results are in agreement with the similar study in the literature.[135]

CHAPTER VI

SURFACE-MODIFIED ORDERED MESOPOROUS MATERIALS

This chapter focuses on the study of the surface-modified mesoporous adsorption materials. The first section introduces our objectives for the study. Section 6.2 and 6.3 describe the molecular models and the property calculations, respectively. The results are presented and discussed in section 6.4, followed by the conclusion in section 6.5.

6.1 Adsorption in Surface-Modified Ordered Mesoporous Materials

The main objective of this study is to contribute to the fundamental understanding and the modeling of organic-modified Ordered Mesoporous Materials (OMMs). In particular, the work focuses on the issue of the adsorption based characterization of these materials. For this purpose, a molecular modeling study of structural and surface properties of a silica material modified via chemical bonding of organosilanes with a range of sizes (C4, C8 and C18) is presented. Although there are some simplifications in the models, the materials parallel those used in a recent experimental work in the literature.[12]

In the experimental work of Jaroniec et al.[12], MCM-41 silica with a pore diameter of 5.0 nm was chemically modified by bonding monomeric-type ligands, such as trimethylsilyl (C3) (TMS), butyldimethylsilyl (C4) (BDMS), and octyldimethylsilyl (C8) (ODMS), as well as polymeric-type 3-aminopropylsilyl (APS-P), (hexanoyl-3-aminopropyl)silyl (APS-P), and octylsilyl ligands (OS-P). The composite materials were

characterized using elemental analysis, high-resolution thermogravimetry (TGA), and nitrogen adsorption at 77 K in a wide range of pressures. Surface coverages of bonded ligands were between 2.5 and 3.0 μmol/m^2. The adsorption measurements showed that pore diameters of the samples decreased systematically with the increase in size of ligands. Changes in the shape of the adsorption isotherms indicated possible changes in structure of the adsorbed nitrogen and the organic phase.

In our work, model systems similar to the experimental systems described above were simulated. For simplicity, the pores of the MCM-41 inorganic materials were modeled as slit-shaped pores, instead of cylindrical pores. Grand canonical MC (GCMC) simulations were used to obtain the nitrogen adsorption isotherms for unmodified and modified porous material models. The adsorption isotherms are utilized for characterization of the materials. In addition, the density profiles of nitrogen and the organic layer (chains) are generated to gain more molecular insight to the problems in organic-modified OMMs. The pore size is estimated for each organic-modified OMMs, and compared with the experimental results.

Although the focus in this work is more on the ordered mesoporous materials, we believe that the results from our studies could apply and be beneficial to any porous materials consisting of silica surfaces modified with organosilanes.

6.2 Molecular Models

The system under study was very similar to the one in the organic-inorganic composite materials, with some simplifications. Although the pores of the MCM-41

silica materials are known to be cylindrical[14], in this study, we employ a slit-shaped model. The slit width was set at 5.0 nm, which corresponds to the pore diameter in the experiments. It was shown that there is an important quantitative difference in the adsorption isotherms in cylindrical and slitlike pores of the same material.[136,137] The equilibrium transition in a slitlike pore of the same size as a cylindrical one occurs at substantially higher relative pressure. Also, the thermodynamic adsorption hysteresis in a slitlike pore is wider than that in the corresponding cylindrical pore. Therefore, the shape of adsorption isotherms for our model systems is expected to be different than the ones for cylindrical pores in the experiments. The system was periodic in the *x* and *y* directions but bounded by two walls in the *z*-direction. The walls were treated as flat, featureless surfaces as in the organic-inorganic composite membranes using an interaction potential proposed by Steele.[119] The potential is given in Eqn (4.1), and the wall potential parameters for MCM-41 were taken from Gelb et al.[138]

Surface coverage for the alkylsilane chains was 4 μmol/m^2, which is slightly higher than that found in the experiments. In simulation work from Joseph et al.[4], the roughness of the silica surface is assumed to be between 3 ± 1.5 Å, and it is modeled by attaching the first monomers within this range. Since our silica model surface is more ordered, the first monomer of each chain was tethered to the wall at the same distance, 2.2 Å, which is the lower bound of the value in the literature.[4] The first monomer of the chains remained fixed at their original positions, but the rest of the monomers sampled different configurations according to the Coupled-Decoupled Configurational-Bias Monte Carlo method described in detail in section 3.3.2. Initial configurations were

created with a stochastic builder based on the Rotational Isomeric States (RIS) method which is explained in detail in section 3.4.[114] For simplicity, the alkyl segments and the nitrogen molecules were modeled by using the united-atom approach[121] where (-CH_2-) and (-CH_3-) segments, and (N_2) molecules were considered as one single site. Bond-stretching, angle-bending, and torsional potentials were applied to the chain segments. These potentials and their constants are obtained from the literature.[121,122] Specifically, monomeric-type, butyl (C4), octyl (C8), and octadecyl (C18) chains were modeled. The materials that are modified with polymeric-type ligands were not studied in this work. The non-bonded interactions were modeled by the 12-6 Lennard Jones (LJ) potential which is given in Eqn (4.4). The non-bonded potential parameters (ε and σ) for the chain segments[121] and nitrogen[138] were taken from sources in the literature.

GCMC is the main simulation tool. The main code, the subroutines that move the chains and all the analysis codes were written internally. Some subroutines for the main GCMC code were provided by Allen and Tildesley.[99] Non-bonded potentials were truncated with the cutoff distance of 15 Å. The temperature of the system was 77 K, corresponding to the experimental temperature[12] at which the nitrogen adsorption isotherms were obtained.

6.3 Property Calculations

6.3.1 Adsorption Isotherms

Adsorption isotherms for nitrogen in modified and unmodified OMMs were determined by GCMC simulations. First, the chemical potentials that correspond to the

pressures of interest were calculated from the modified Benedict-Webb-Rubin (MBWR) equation of state.[139] Next, GCMC simulations were performed to find the adsorbed number of molecules at different, fixed values of the chemical potentials; in this way, the amount of gas absorbed by the system at different pressures was obtained. The results were normalized by the total surface area of the two walls (*N/2A*). Then, they were plotted as adsorbed surface density of molecules ($\mu mol/m^2$) vs. relative pressure (P/P_{sat}), where P_{sat} is the saturation pressure at 77 K temperature which is also obtained by using the same equation of state (P_{sat}=1.2817 bar).

In low concentration limits (at very low pressures), we calculated the Henry's constants for the four different systems in our adsorption studies: unmodified and modified MCM-41 materials with different alkane-chains (C4, C8, C18). In order to find the Henry's constant, one needs to calculate the limiting slope of the adsorption isotherm at zero pressure. One of the limitations of the GCMC algorithm that we employed is that at least 2 adsorbate molecules must be present in the system during the simulation. Therefore, performing GCMC simulations at these conditions (very low pressures) requires very large simulation box sizes, and consequently excessive CPU time. As a result, the simulations, especially the ones for the systems with the alkane-chains attached, become practically very difficult to perform. To avoid this technical problem, we pursued the Widom[117] approach, as in the solubility calculations, as an alternative method to calculate the Henry's constant. In very low concentration limits (ideal sorbed phase), the equilibrium concentration of the gaseous species in the polymer matrix can be written as:

$$\frac{N}{V} = \beta \left\langle \exp\left(-\beta \Delta E\right) \right\rangle_{NVT} P \tag{6.1}$$

where N/V denotes the number density of adsorbed molecules.[118] The average, $\left\langle \exp\left(-\beta \Delta E\right) \right\rangle_{NVT}$, was again calculated by performing random insertions of a nitrogen "test molecule" in the system. Eqn. (6.1) can also be expressed as the amount of adsorbed molecules per surface area. The nitrogen adsorption isotherms from the simulation results are presented in this form.

$$\frac{N}{A} = P_{sat} \beta L \left\langle \exp\left(-\beta \Delta E\right) \right\rangle_{NVT} \left(\frac{P}{P_{sat}} \right) \tag{6.2}$$

If one plots $\frac{N}{A}$ vs. $\frac{P}{P_{sat}}$, the slope gives the Henry's constant which is equal to the value of $P_{sat} \beta L \left\langle \exp\left(-\beta \Delta E\right) \right\rangle_{NVT}$. Here L is the pore width and it was taken as 50 Å for our studies. In order to verify the accuracy of the alternative method, the Henry's constants from both methods, by slope from the simulation data and by Widom insertion calculations, for the two simpler models, unmodified and C4-modified porous materials, were compared. The Henry's constants for these two models are given in Table 6.1 for comparison. In addition, the simulation data and the slopes that are calculated from Widom approach are shown in Figure 6.1. The dots (.) and dashes (-) represent the simulation data and the slopes (Henry's constants) from Widom calculations, respectively. By examining the results, it was concluded that both methods yield the same results (within statistical error), and the results obtained by Widom approach are

adequate for the calculation of the Henry's constants. The results for the lower pressure region are discussed later in this chapter.

Table 6.1 The Henry's constants for unmodified and C4-modified porous model materials by two different methods (slope of the simulation data and Widom approach).

	Slope x 10^4	Widom approach x 10^4	STDV x 10^4
Unmodified	1.2105	1.37	0.379
C4-modified	15.894	17.8	2.2964

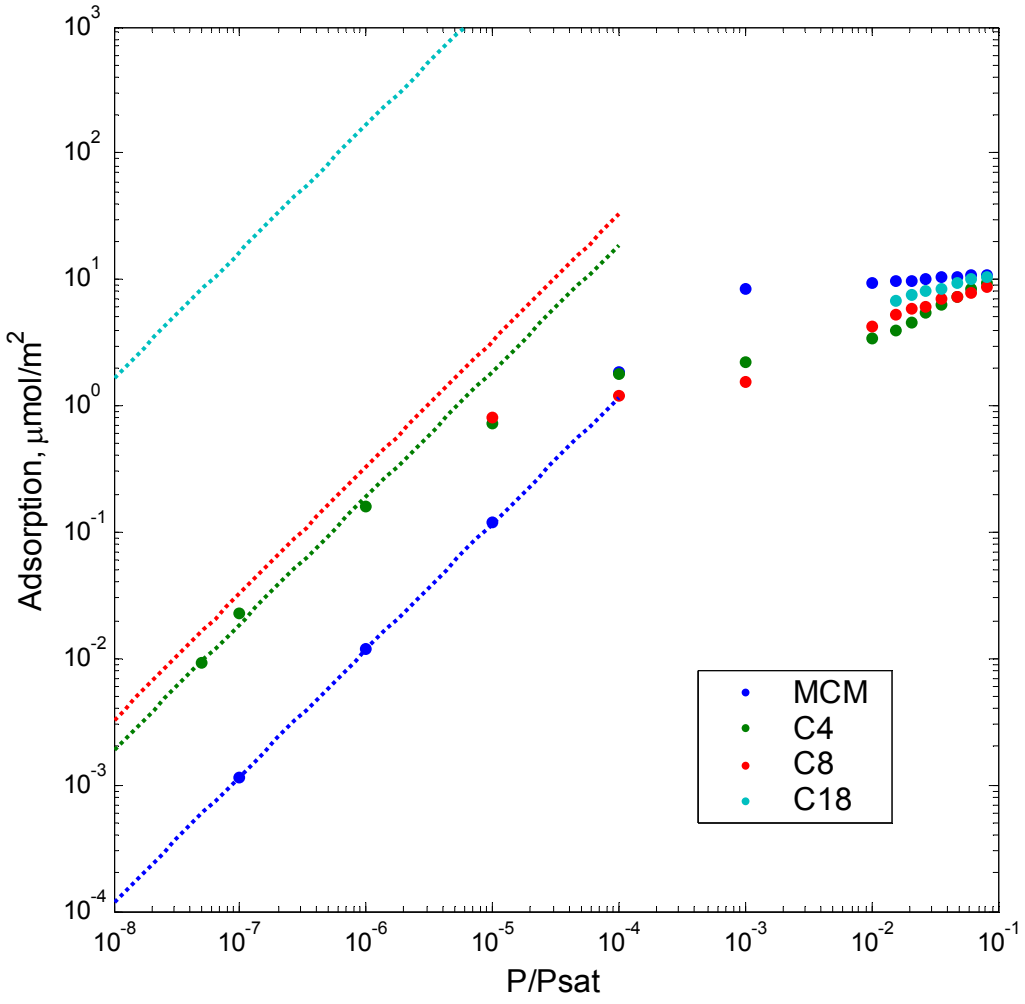

Figure 6.1 The simulation data and the slopes that are calculated from Widom approach for all model systems. The dots (.) and dashes (-) represent the simulation data and the slopes (Henry's constants) from Widom calculations, respectively.

6.3.2 Segmental Density Profiles

The local packing of the organic chains and the population of the nitrogen molecules along the width of the pore provide valuable information about the behavior of the adsorption isotherms. Therefore, the density profiles for the nitrogen molecules were measured as well as for the organic layers (chain segments) that were attached to the inorganic surface. The segmental density profile was measured for both the nitrogen and the chain molecules by the same approach described in section 4.4.4. The bin widths were taken as 0.33 Å for all the calculations.

6.3.3 Pore Size Calculations

The average pore size of the modified porous material models are estimated by analyzing the density profiles of the alkyl chains, and compared with the experimental results. The distance between the points on each side where the density of the chain segments reaches zero was taken as the new pore size after the modification of the materials.

6.4 Results

6.4.1 Nitrogen Adsorption

As it is mentioned earlier, this work represent semi-quantitative model of one of Jaroneic et al.'s experimental studies.[12] Therefore, first, the corresponding experimental results from their study are presented here for comparison. Nitrogen adsorption

isotherms for the unmodified and modified MCM-41 materials from this study are shown in Figure 6.2 and Figure 6.3, and the authors' interpretations about these results are summarized next.

- The unmodified MCM-41 exhibited a sharp step of capillary condensation at the relative pressure of ca. 0.5, indicating a narrow pore size distribution of the material.
- It was evident that there was no significant secondary mesoporosity, since the adsorption isotherm was very flat in the high-pressure region (above P/P_{sat} of about 0.6).
- Modification of the materials did not cause any changes on the overall shape of adsorption isotherms. It was indicated that ordering of the MCM-41 support was not affected by the modification because of the pronounced steps of capillary condensation in primary mesopores.
- The position of the capillary condensation steps gradually shifted to lower pressure values for the modified materials. This effect became more pronounced with the increase in size of the bonded ligands. A gradual disappearance of the hysteresis loop was observed with the shift.
- For the unmodified sample, a pronounced hysteresis loop was observed. The desorption branch was steeper in comparison to the adsorption branch, especially near its lower closure point (relative pressure of ca. 0.4).[15,90]

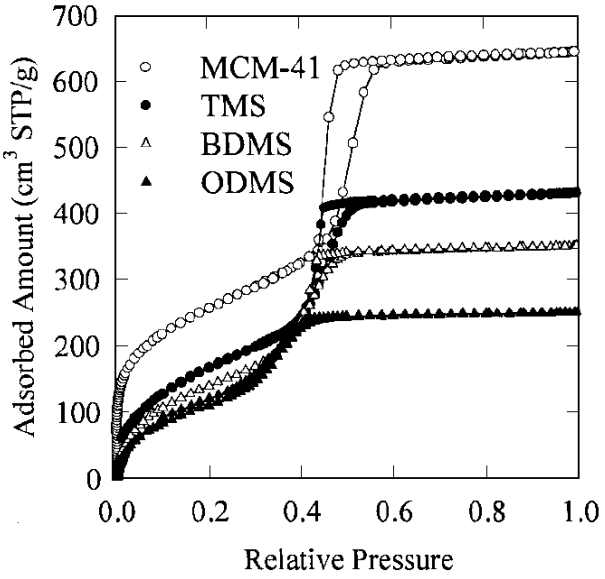

Figure 6.2 Nitrogen adsorption isotherms for the unmodified MCM-41 and for the samples with bonded trimethylsilyl, butydimethylsilyl, and octyldimethylsilyl groups from Jaroniec et al.[12]

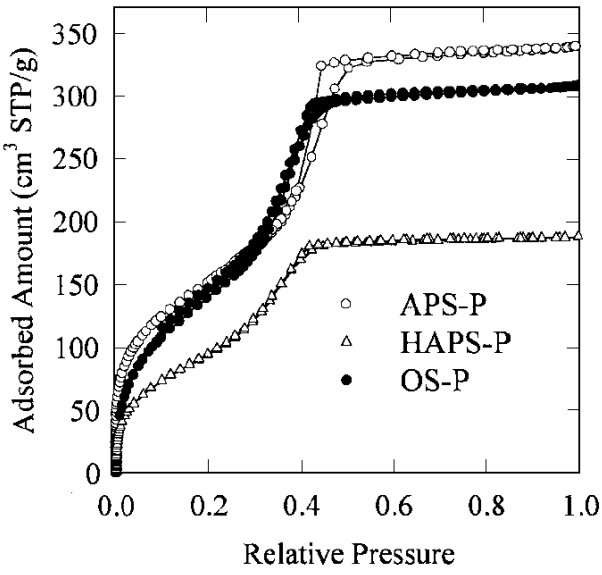

Figure 6.3 Nitrogen adsorption isotherms for the aminopropyl, hexanoyl-3-aminopropyl, and octyl polymeric bonded phases from Jaroniec et al.[12]

- In the case of TMS, BDMS, and APS-P, there were triangular hysteresis loops with very steep desorption branches. However, HAPS-P exhibited a very narrow hysteresis loop at a relative pressure of ca. 0.4. The adsorption-desorption process was almost fully reversible.
- An interesting behavior of MCM-41-based octyl-bonded stationary phases (ODMS and OS-P) were noticed, their nitrogen adsorption isotherms showed a low-pressure hysteresis at relative pressures below 0.4.

This is an interesting result, because based on the experimental studies on unmodified MCM-41 materials with different pore sizes, it is very unusual to witness hysteresis at pressures below 0.4, which is a lower closure point for nitrogen adsorption. Hysteresis loops start appearing usually at or above 0.4, and generally for the materials with 4.0 nm or larger pore sizes.[90] For the materials with pore sizes between 2 and 3.5 nm, no hysteresis is observed.[92] Therefore, typically low-pressure hysteresis loops can be attributed to the presence of constrictions in porous structures or to swelling of the adsorbent during the adsorption process.[15] In the present case, the authors eliminated these two factors by the following interpretations/discussions:

1. There is no low-pressure hysteresis for HAPS-P, which has the largest ligands among the modified samples considered. Therefore, the influence of constrictions in porous structure can probably be precluded.

2. If there were swelling, it is not likely that it would affect only the octyl-modified materials and would not take place for the other bonded phases.

Jaroneic et al.[12] attributed the low-pressure hysteresis for these materials to very weak interactions between nitrogen and long aliphatic chains. They speculated that "the formation of nitrogen film on the surface may cause changes in the configuration of octyl-bonded groups in order to diminish unfavorable interactions. Alternatively, during the adsorption-desorption process some nitrogen molecules may cross the layer of bonded octyl groups and reach high-energy adsorption sites of the silica surface (or possibly side silanols and/or cross-linking siloxane groups in the case of the bonded polymeric phases OS-P). These higher energy sites might also become accessible as a result of the aforementioned hypothetical change in configuration of octyl groups.".[12]

It was also stated in a review[93] that these low-pressure hysteresis are generally due to either the slow penetration of the adsorbate molecules into very narrow pores or a slow expansion of the pore structure.[15] The explanation for this interesting phenomenon is still not entirely clear.

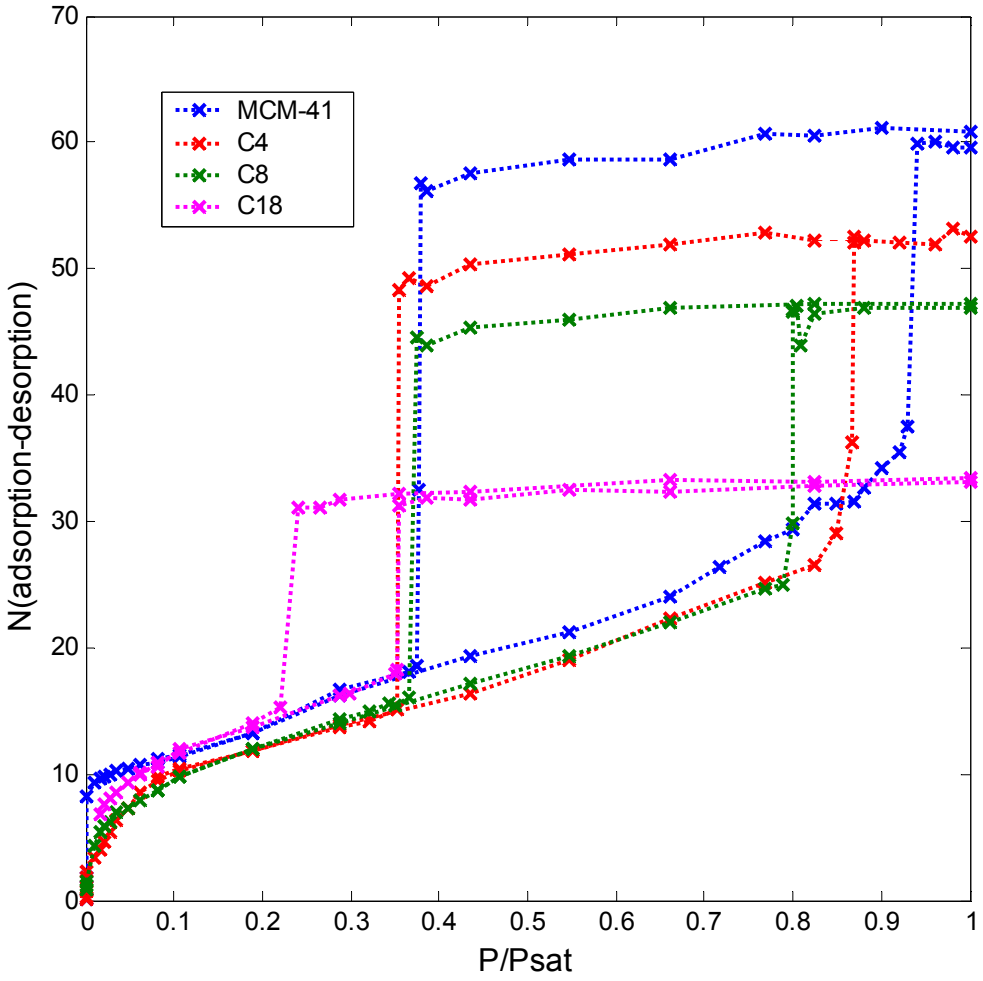

Figure 6.4 Nitrogen adsorption isotherms for the unmodified and C4, C8, C18 modified model materials from the simulations.

The simulation results for nitrogen adsorption in unmodified and modified MCM-41 model materials at different relative pressures are presented in Figure 6.4. The capillary condensations are observed at higher pressures, and consequently the widths of the hysteresis loops are larger in comparison to the experimental results, due to the fact that the pore models in the simulations are slit-shaped.[106,137,140] However, very similar trends as in the experimental results are observed with the increase in size of the bonded ligands: the position of the capillary condensation steps gradually shifted to lower pressure values, and this shift was accompanied by a gradual disappearance of the hysteresis loop. The hysteresis loops exhibit triangular-shape with very steep desorption branches in comparison to the adsorption branches. All of them, but one, appear above the relative pressure of ca. 0.4. The C18-modified-pore model shows a low-pressure hysteresis loop between the relative pressure of ca. 0.22 and 0.4, which is comparable to the case of MCM-41-based octyl-bonded stationary phases (ODMS and OS-P) in the experimental results. In order to understand the molecular behavior behind this interesting result, the local (segmental) density profiles are obtained for further analysis.

6.4.2 Density Profiles

First, the density profiles for unmodified MCM-41 model material at different relative pressures are shown in Figure 6.5 through Figure 6.8 to illustrate the adsorption mechanism in the bare MCM-41 materials. In addition, some of these profiles are collected in a 3D-plot in Figure 6.9. Based on the analysis of these profiles, one can clearly see that the multi-layer adsorption process occurs. The first adsorption layer of

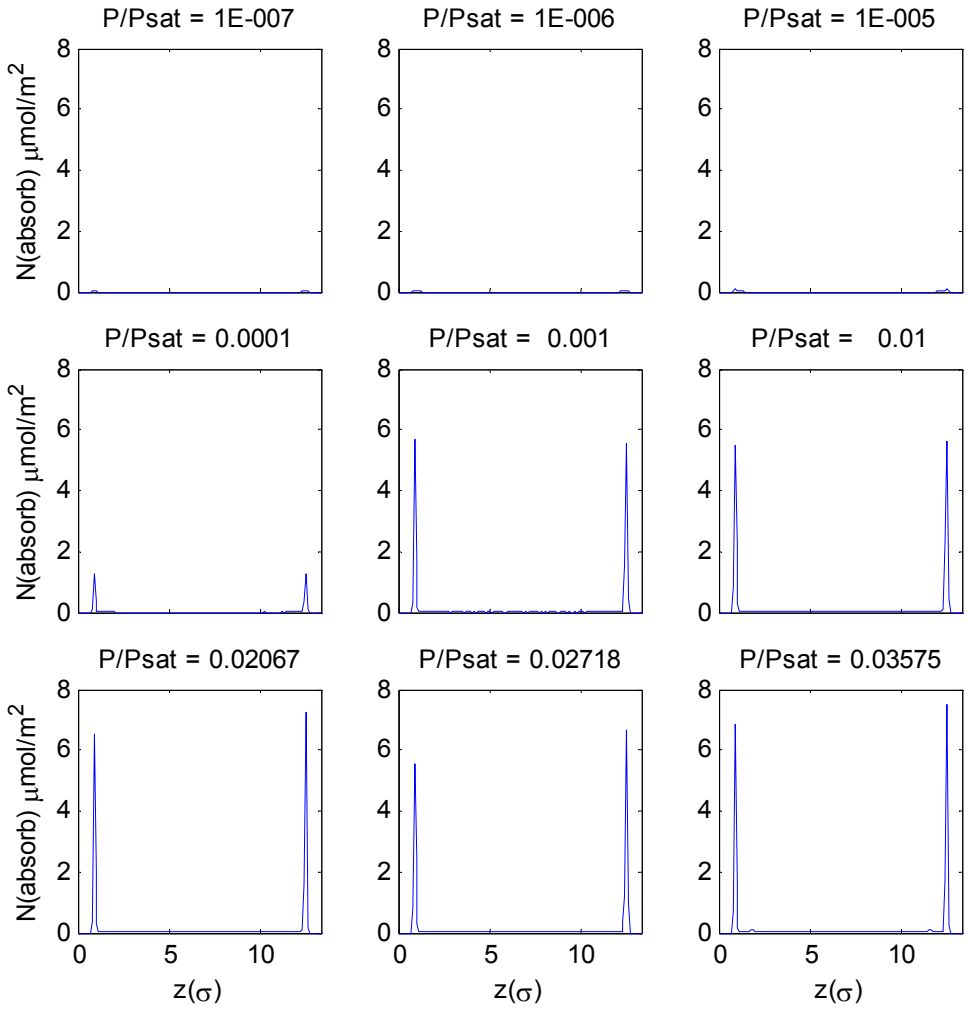

Figure 6.5 Density profiles for unmodified MCM-41 model material at different relative pressures from the simulation results. The relative pressure values are shown above each individual sub-figure (adsorption process from P/P_{sat} =1E-007 to P/P_{sat} =0.03575).

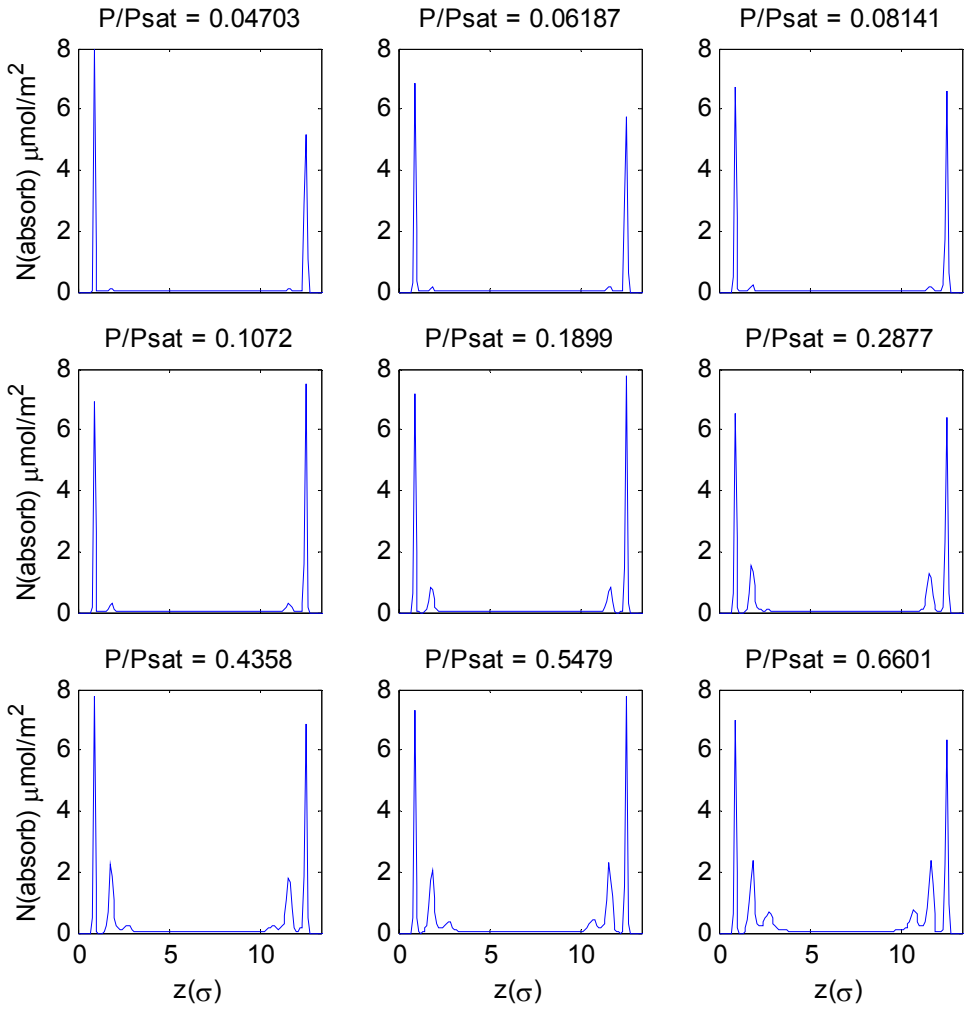

Figure 6.6 Density profiles for unmodified MCM-41 model material at different relative pressures from the simulation results. The relative pressure values are shown above each individual sub-figure (adsorption process from P/P_{sat} =0.04703 to P/P_{sat} =0.6601).

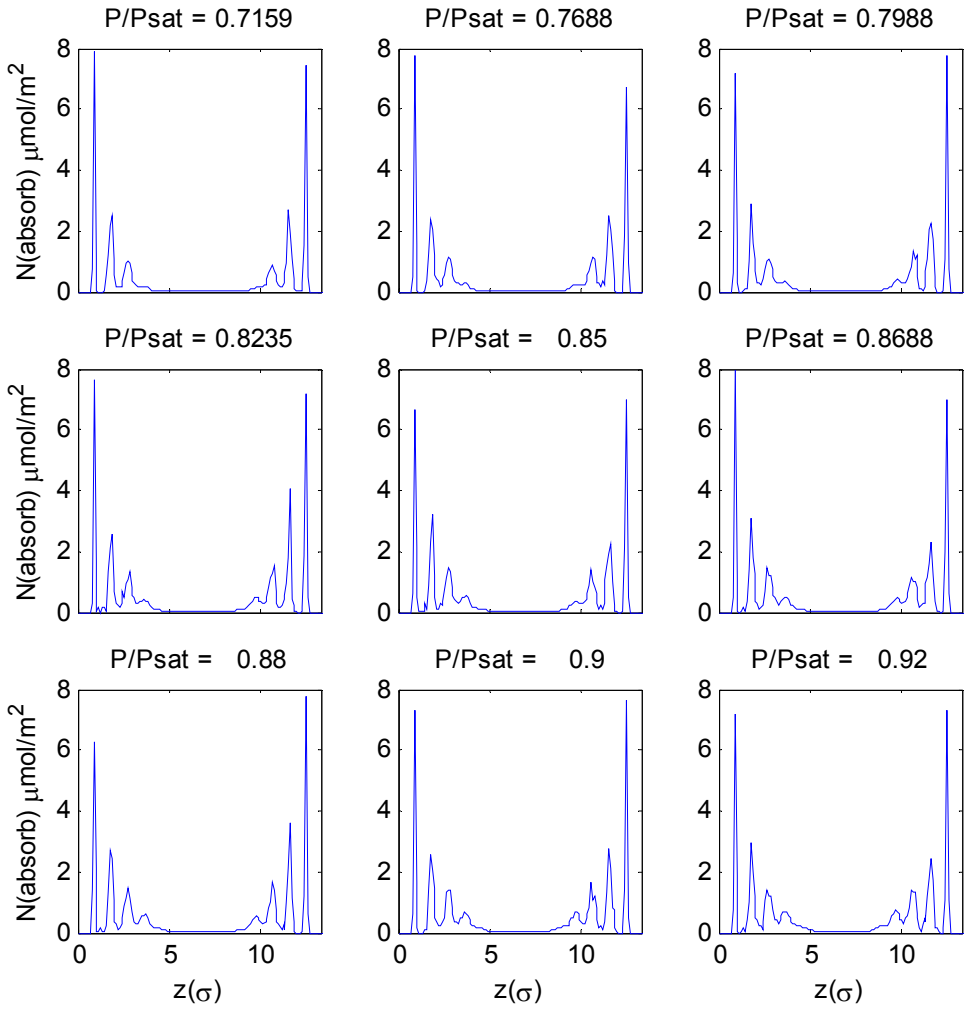

Figure 6.7 Density profiles for unmodified MCM-41 model material at different relative pressures from the simulation results. The relative pressure values are shown above each individual sub-figure (adsorption process from P/P_{sat} =0.7159 to P/P_{sat} =0.92).

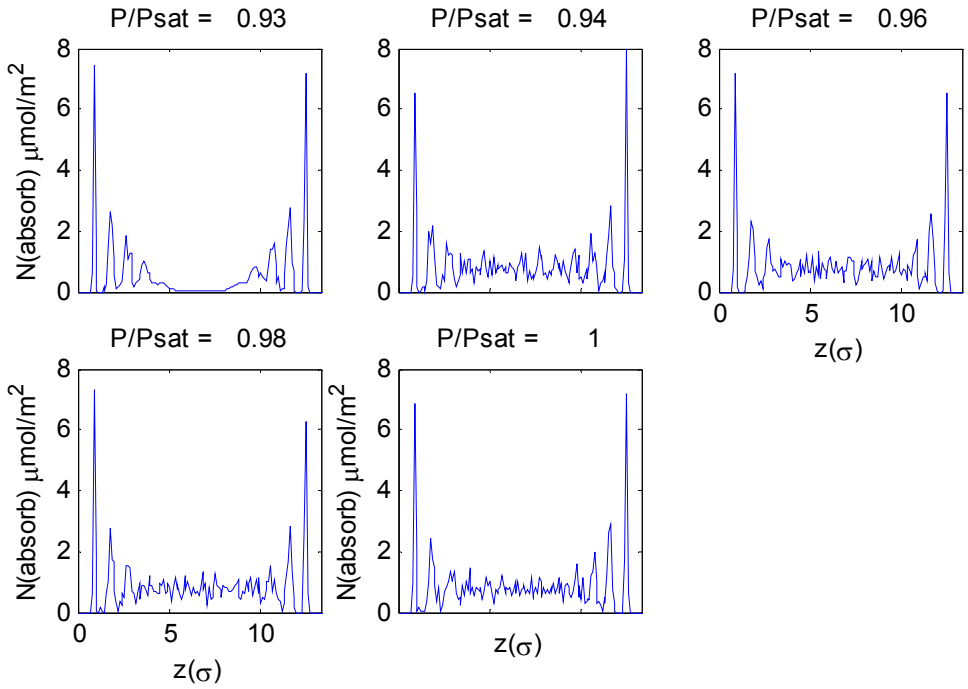

Figure 6.8 Density profiles for unmodified MCM-41 model material at different relative pressures from the simulation results. The relative pressure values are shown above each individual sub-figure (adsorption process from P/P_{sat} =0.93 to P/P_{sat} =1.0).

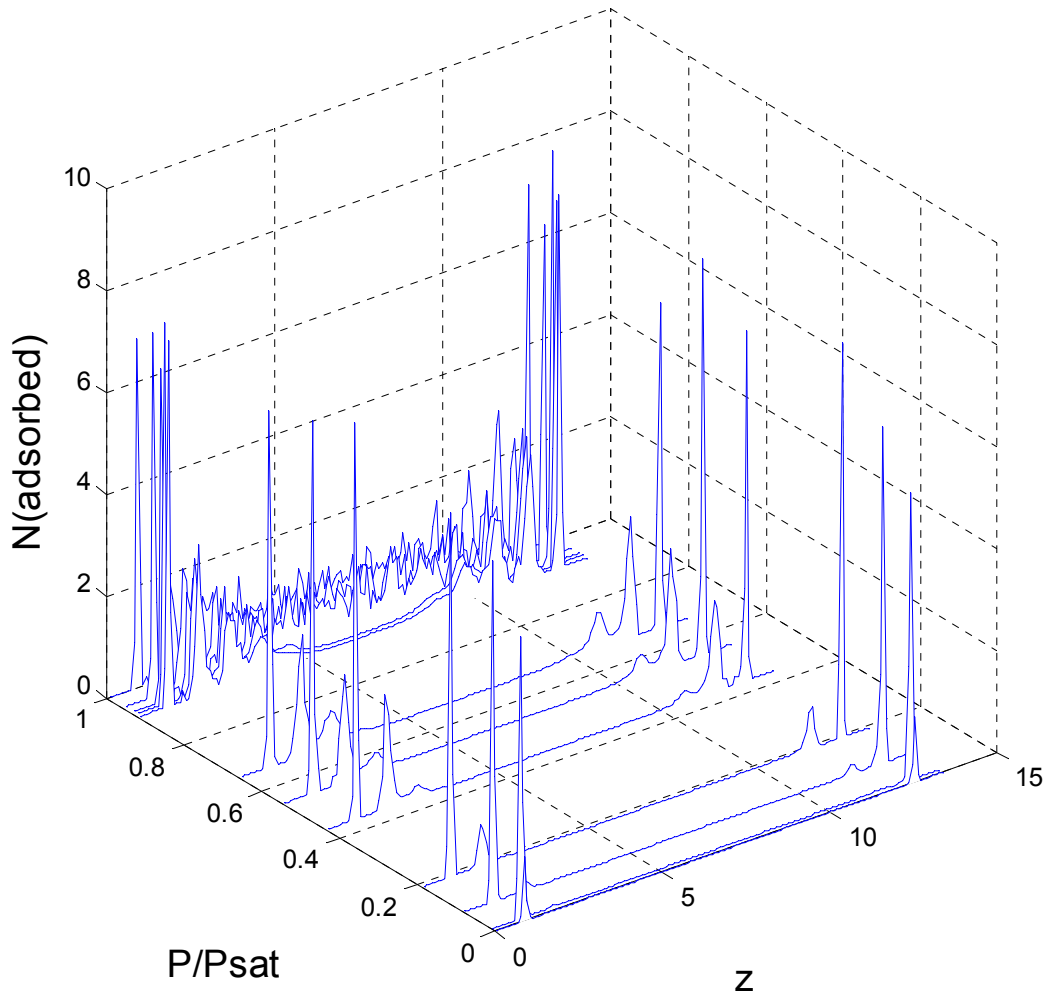

Figure 6.9 3-dimensional representation of density profiles for unmodified MCM-41 model material at different relative pressures from the simulation results.

nitrogen in MCM-41 is not complete until P/P_{sat}=0.02. As the pressure increases to the P/P_{sat}=0.1072, the second layer of adsorption becomes clearly visible. Continuing to increase pressure to P/P_{sat}=0.4358, the third adsorption layer starts to build. Finally, the capillary condensation of nitrogen in MCM-41 appears at the relative pressure of ca. 0.94. The simulation results that confirm the same adsorption mechanisms described above in the MCM-41 materials are also found in a recent work[103], with a cylindrical pore model.

Next, the density profiles for C18-modified MCM-41 model materials at different relative pressures throughout the adsorption process in Figure 6.10 through Figure 6.12 are analyzed to understand the adsorption mechanism in the presence of chains, and maybe the underlying reason for the low-pressure hysteresis. The blue and green colors represent the chain segments and nitrogen, respectively. In this case, the multi-layer adsorption is rather limited, due to the presence of the chains. The first three layers of nitrogen adsorption are very small in comparison to the unmodified MCM-41 model material. The bonded ligands limit the accessible areas for nitrogen adsorption on the silica surface. One conceptual picture is that the aggregation of the chains forms a network of interconnected micropore structure, which is accessible only through narrow channels (or pathways). First, the nitrogen molecules fill in these limited accessible-sites. Next, the open pore volume in the middle of the pore (effective pore size), which is considerably smaller than the unmodified materials, is completely filled resulting in a capillary condensation at the relative pressure of ca. 0.3557.

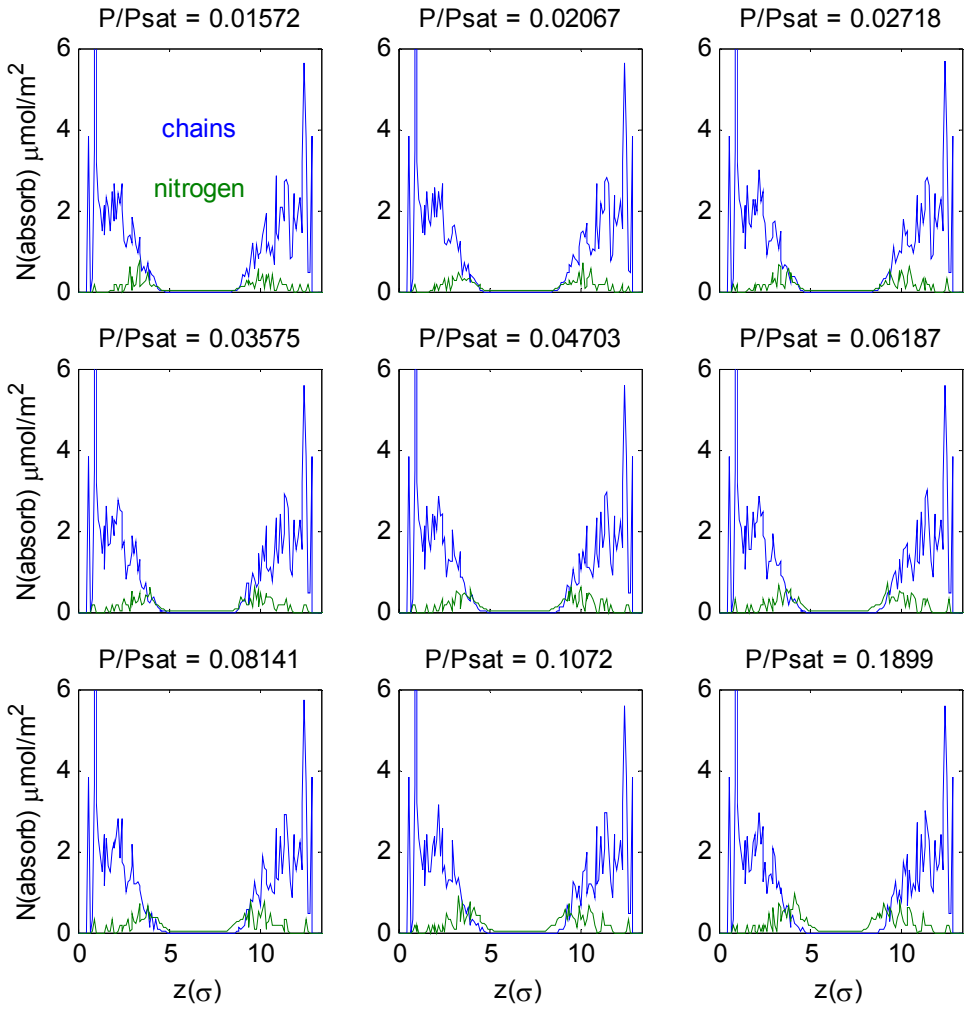

Figure 6.10 Density profiles of nitrogen and chain segments in C18-modified model materials at various relative pressures. The relative pressure values are shown above each individual sub-figure (adsorption process from P/P_{sat} =0.01572 to P/P_{sat} =0.1899).

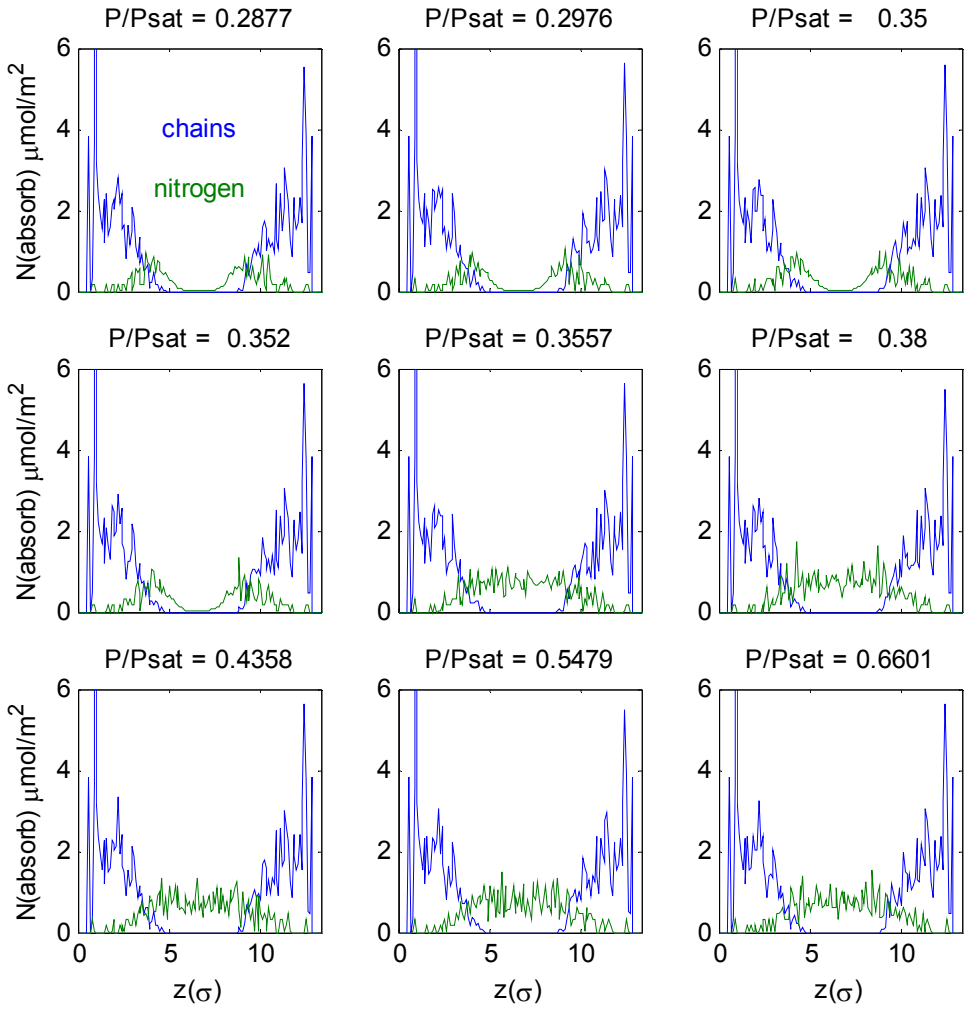

Figure 6.11 Density profiles of nitrogen and chain segments in C18-modified model materials at various relative pressures. The relative pressure values are shown above each individual sub-figure (adsorption process from P/P_{sat} =0.2877 to P/P_{sat} =0.6601).

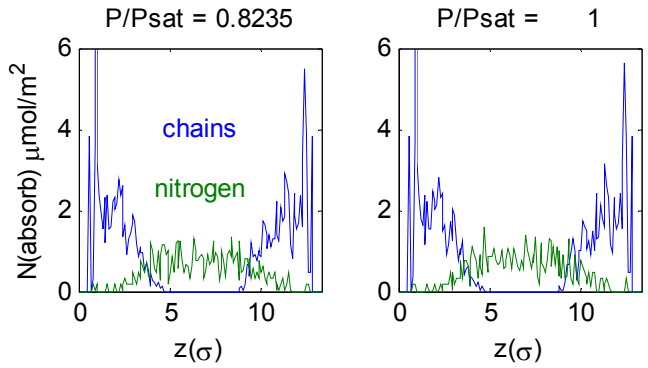

Figure 6.12 Density profiles of nitrogen and chain segments in C18-modified model materials at various relative pressures. The relative pressure values are shown above each individual sub-figure (adsorption process from P/P_{sat} =0.8235 to P/P_{sat} =1.0).

For the sake of comparison, the density profiles for 4 different (unmodified, C4, C8 and C18-modified MCM-41) model materials at the pressures where the capillary condensation (Figure 6.13) and evaporation (Figure 6.14) occur are presented.

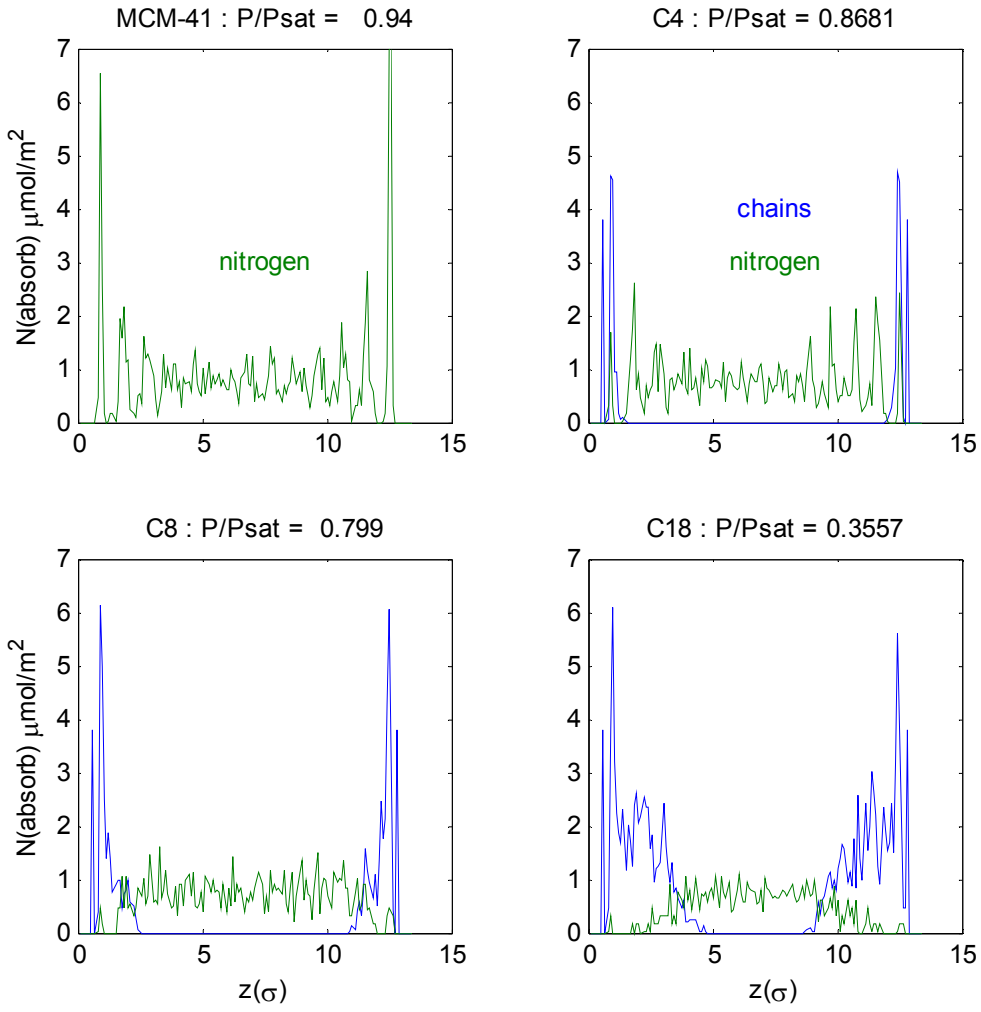

Figure 6.13 Comparison of density profiles for unmodified, C4, C8 and C18-modified MCM-41 model materials at the pressures where the capillary condensation occurs.

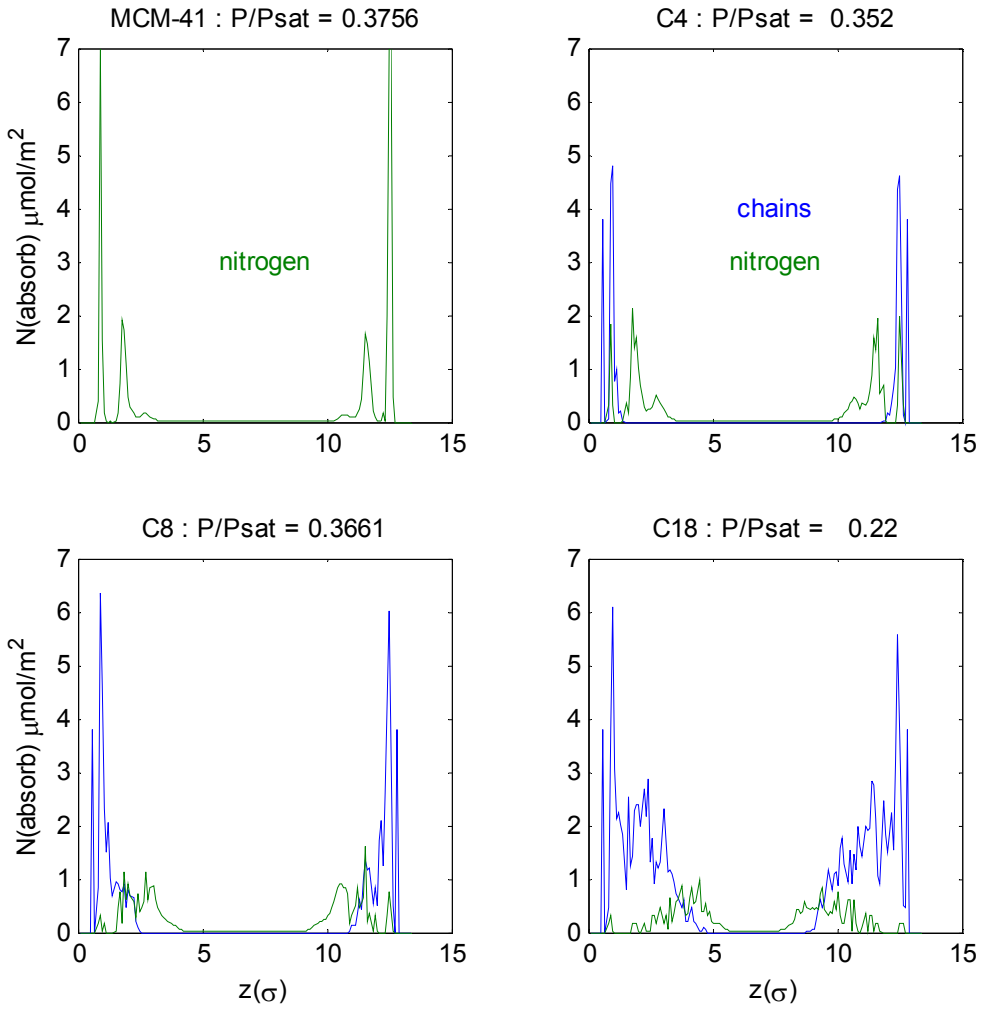

Figure 6.14 Comparison of density profiles for unmodified, C4, C8 and C18-modified MCM-41 model materials at the pressures where the capillary evaporation occurs.

As the length of the bonded ligands is increased, the multi-layer adsorption mechanism is suppressed. It becomes more like filling micropore structures. Although some of the first, and the complete of the second and third adsorption layers are still apparent in the C4-modified models, they start disappearing with the C8-modified model materials. Finally, the adsorption layers become unclear in the C18-modified models.

6.4.3 Low-Pressure Hysteresis

In order to examine the effects of the chains on the low-pressure hysteresis in C18-modified model material, the density profiles obtained during the adsorption process at various pressures are compared with the density profiles obtained during the desorption process at the same pressures. The results for both processes are presented in Figure 6.15. The sub-figures in Figure 6.16 just focus on the nitrogen density profiles of the same results. Except the P/P_{sat}=0.2877, which corresponds to approximately the middle point of the hysteresis loops, no substantial differences in the profiles are observed. The difference at this pressure appears mostly in the middle of the pore where there are no chains (effective pore volume). The density profiles close to the surfaces, where the chains are mostly present, are not very different for the adsorption process than for the desorption process. As it is discussed in section 6.4.2, it is obvious that chains' being on the surface reduces the adsorption of nitrogen on the surface in comparison to unmodified model materials. However, there is no evidence whether or not that is the reason for the low-pressure hysteresis.

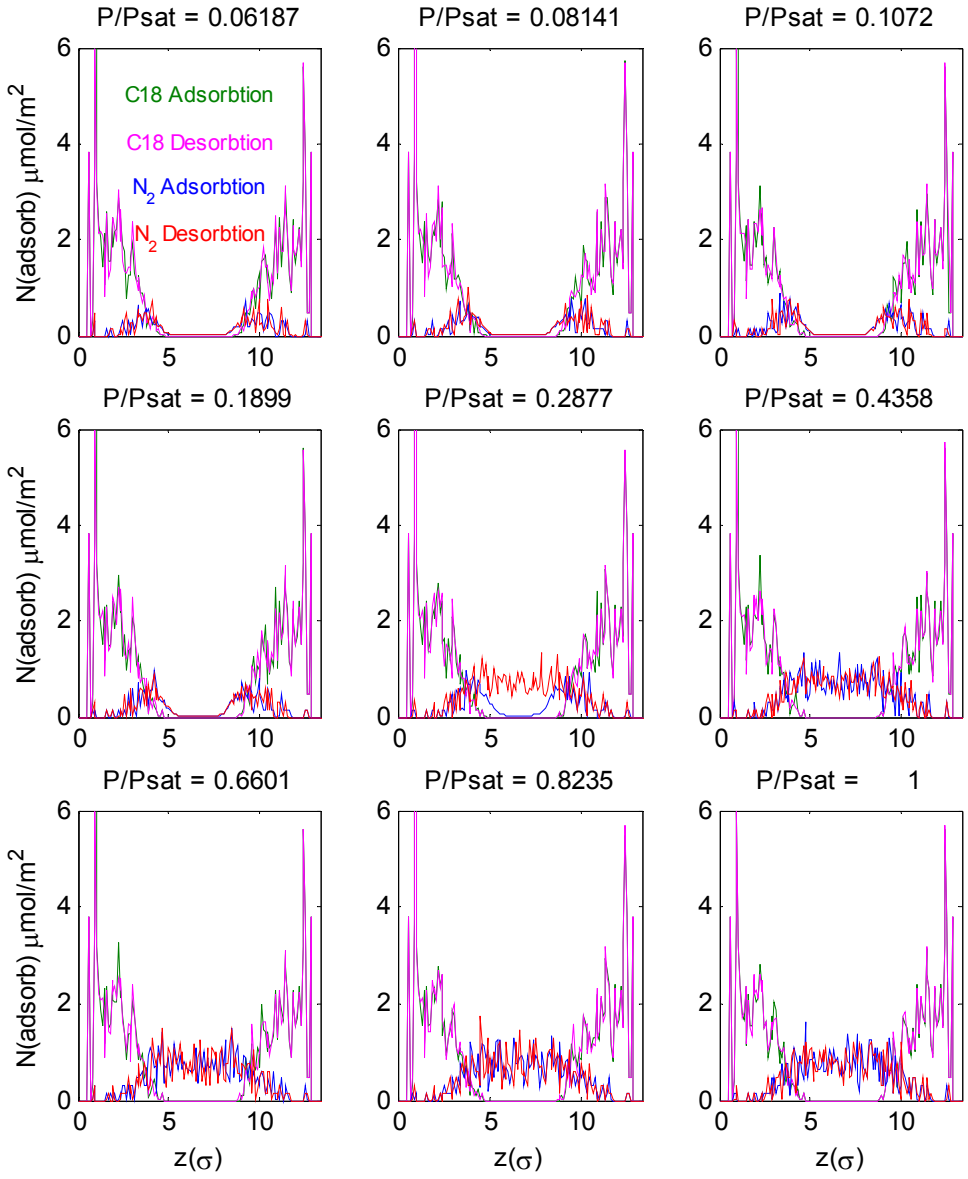

Figure 6.15 Comparison of density profiles of nitrogen and chain segments in adsorption process vs. desorption process (C18-modified model material).

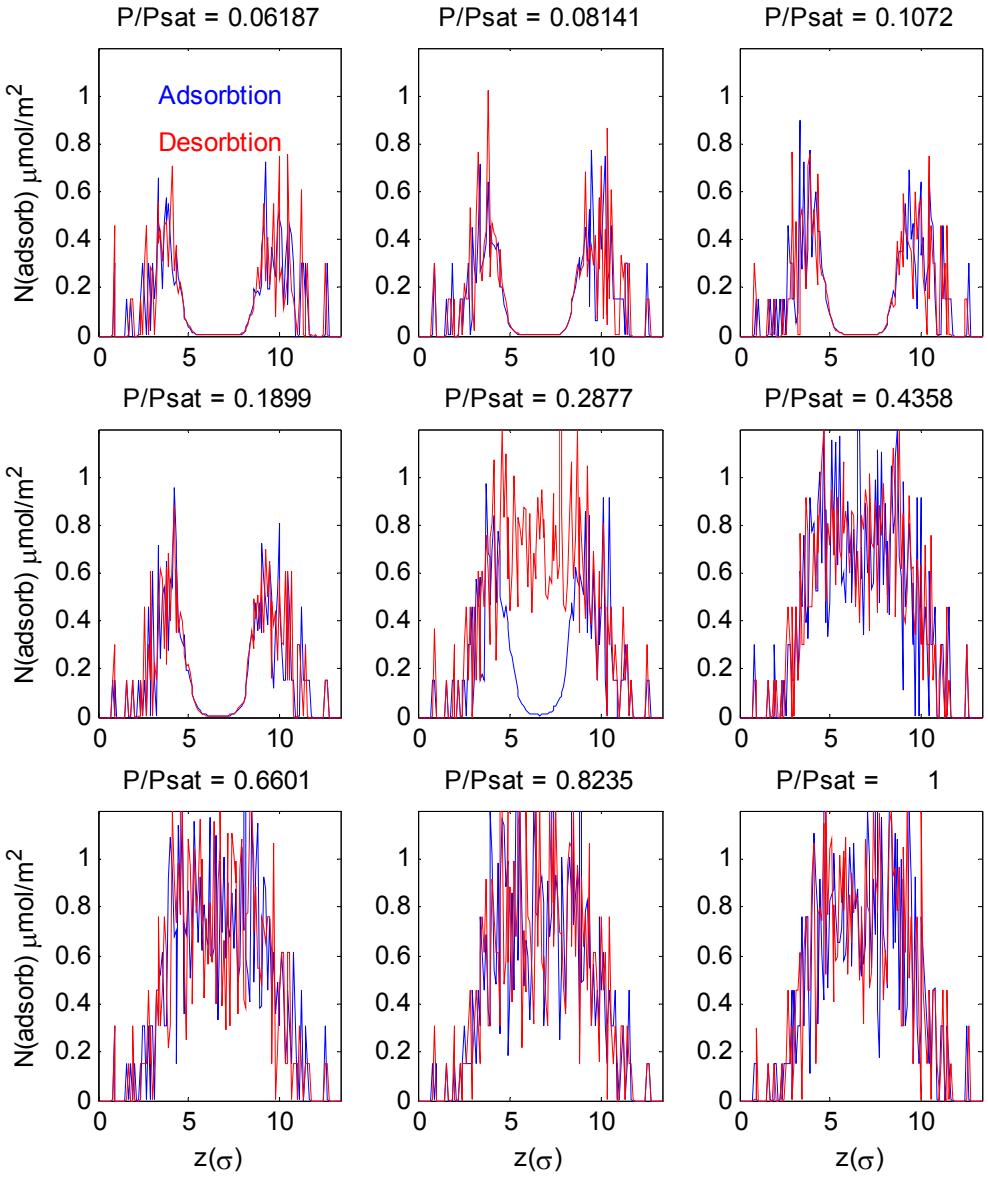

Figure 6.16 Comparison of density profiles of nitrogen in adsorption process vs. desorption process (C18-modified model material).

In fact, hysteresis loops in different pore sizes and different pore structures have been subject to several simulation studies[103-106] in the past. Most of the studies showed that it is more common to see low-pressure hysteresis in simulation results for mesoporous materials (carbon with slit-like or silica with cylindrical pore) with pore sizes below 5 nm.[103-106] In addition, Maddox et al. suggested that the critical pore diameter below which the nitrogen adsorption isotherm is reversible is between 2.8 and 3.2 nm.[105] However, at this stage, the reason or reasons for the low-pressure hysteresis observed in our results are not completely clear, because the contributions of many effects are unknown, such as, the effect of the choice of model surface material and model pore geometry – slit vs. cylindrical. Further studies should be taken to clarify/eliminate these effects.

6.4.4 Nitrogen Adsorption at Low Pressures

The low pressure results for the particular experimental work[12] are shown in Figure 6.17. Although, the TMS-modified sample still exhibits appreciable low-pressure adsorption, it is dramatically reduced in the presence of organic ligands. The slopes of the low pressure adsorption data from the simulations for all the model materials are presented in Figure 6.1, and their exact values are given in Table 6.2.

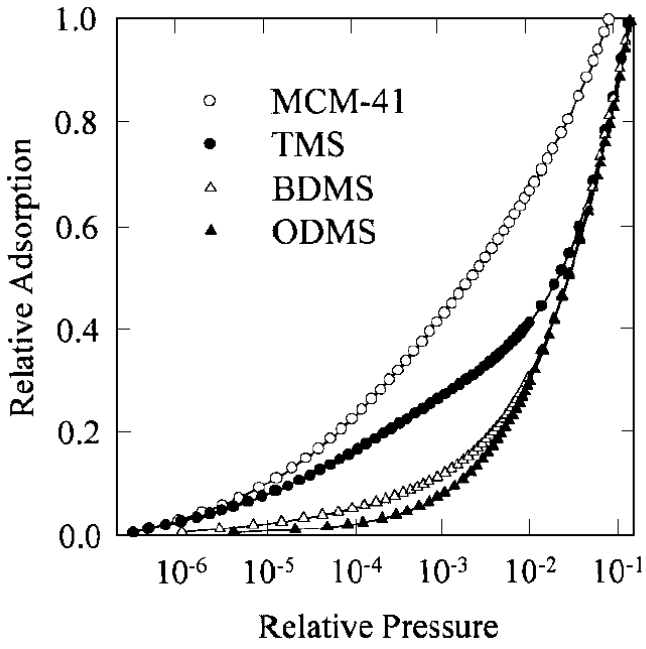

Figure 6.17 Low-pressure parts of relative adsorption curves for the unmodified MCM-41 and for the samples modified with TMS, BMS and ODMS groups.[12]

Table 6.2 The slope values of the low pressure adsorption data from the simulations for all the model materials.

	Unmodified	C4-modified	C8-modified	C18-modified
Slope x 10^4	1.37	17.8	32.9	16700

According to the data from the simulations, the low-pressure adsorption increases as the chain length of the organic ligands is increased, in contrast to the experimental results. Especially, the increase for the C18-modified model materials is remarkable. This difference between the modeling and experiment may be attributed to the heterogeneity of the real samples. The actual surface of siliceous materials is strongly heterogeneous because of its non-crystalline character and the presence of different surface groups, such as silanols and siloxanes.[92,98] In fact, in a recent molecular simulation study of the adsorption of nitrogen by MCM-41, Maddox et al.[105] have explored the effects of the surface energetic heterogeneity. They showed that the models in which the solid-fluid interaction potential is assumed homogeneous are incapable of reproducing an experimental isotherm, particularly at low pressures (at P/P_{sat} down to 2.7×10^{-6}). In the same study, a heterogeneous surface model is shown to give very good agreement with the low-pressure adsorption isotherm data. Since the interaction of the adsorptive with the pore wall is short-ranged, the first adsorbed layer is affected more by the MCM-41 surface in comparison to the subsequent layers. Thus, modeling the low-pressure region does require a detailed description of the adsorbent. Although our results at low-pressures are not in an agreement with the experimental results, they are consistent with the model (homogeneous surface) we used.

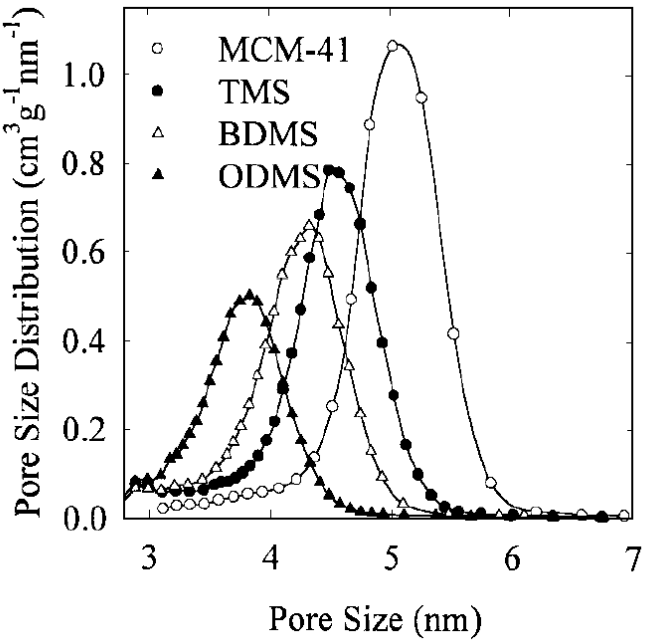

Figure 6.18 Pore size distributions for the unmodified MCM-41 and for the samples modified with TMS (C1), BMS (C4) and ODMS (C8) groups.[12]

Table 6.3 Pore size values from the literature and simulations for unmodified and modified MCM-41 materials.

Pore Size (nm)	MCM-41	C1	C4	C8	C18
literature	5.0	4.5	4.3	3.8	N/A
simulation	5.0	N/A	3.9	3.2	1.5

6.4.5 Pore Size Estimations

Pore size distributions in the experimental work were calculated from adsorption branches of nitrogen isotherms applying the BJH method[141] with the corrected form of the Kelvin equation for capillary condensation in cylindrical pores.[90] These distributions are shown in Figure 6.18 and the resulting pore sizes are listed in Table 6.3 with our simulation results for the comparison. As it is seen from both results, a systematic decrease in the pore diameter with the increase in size of bonded ligands was observed. Although the pore sizes that we estimated do not have an exact quantitative agreement with their average pore sizes, they are still within the pore size distribution limits given in Figure 6.18. Moreover, Jaroniec et al.[12] note that their calculated pore sizes may be slightly overestimated because of limitations in their interpretive model.

6.5 Conclusions

The nitrogen adsorption technique is found to be very useful tool for characterization of the unmodified and organic-modified MCM-41 materials. The current study showed a qualitative agreement with the trends in the adsorption isotherms observed in the experiments, even though the models were simplified adaptation of the real systems. However, low-pressure adsorption data did not have an agreement because of the surface heterogeneity effects. The density profiles of alkyl chains and nitrogen molecules are analyzed to bring some molecular insight to the adsorption mechanism in the materials. In addition, pore sizes for all the materials are estimated by examining the density profiles of alkyl chains.

CHAPTER VII

SUMMARY AND FUTURE DIRECTIONS

Self-assembled monolayers (SAMs) have become a rich area of research and applications. The capability of altering and controlling the chemical nature of surfaces allows SAMs to be used to construct novel materials for various applications. Although numerous experimental studies[12-13,16-26] have been carried out to gain understanding of SAMs behavior at the molecular level, the link between the nanoscale characteristics of a surface film and its macroscopic behavior in many applications still remains unclear. Therefore, this work aimed to further extend the understanding of SAMs by using molecular simulations as a tool. Molecular simulations have the advantage of following a model system in complete atomic-level detail. This quality makes them ideal tool for our studies. In particular, the studies focused on three different applications of SAMs, organic-inorganic composite membranes for gas separations[1-3], surfaces of micro-electro-mechanical systems (MEMS)[8-10] and ordered mesoporous materials (OMMs) such as MCM-41[11-15].

7.1 Organic-Inorganic Composite Membranes

Molecular simulations were used to examine the effects of pore size, organic group size, and organic surface density on the performance of an organic-inorganic composite membrane in a prototype solubility-based separation. The modeling studies paralleled experimental work from the literature.[1]

The model systems for the experimentally realized nanocomposite membranes of Javaid et al.[1] were studied. In particular, the diffusivity and solubility of propane and nitrogen in the model composite materials were predicted by using canonical MD; the permeability was obtained as the product of diffusivity and solubility. The effects of pore size, chain length and surface density for these composite gas separation materials were investigated and compared with experiment.

Good qualitative agreement is achieved with experiment in several respects, including the improvement in the overall selectivity of the membrane and decrease in the permeance when increasing the chain length. The best improvement in the overall solubility selectivity is reached when the chains span throughout the pore. On the other hand, it is concluded that if the surface density is too high, the permeance of the penetrants drops significantly, which is not very preferable for a membrane performance.

In the future directions, one may examine the optimum surface coverage for a better membrane performance by calculating the selectivity vs. surface coverage profiles. Also, the effects of different organic groups on the membrane performance may be investigated.

7.2 MEMS

Alkylsilane-SAMs are used as coatings for Si-based MEMs which suffer from adhesion and friction problems. The adhesion forces between the surfaces are computed by using canonical MD simulations. The effects of different chain lengths (C4, C8 and C18) on adhesion are investigated. It was shown that as the chain length is increased

from 4 to 18 carbon atoms, the adhesion forces between two monolayers at the same separations decreases. Tilting and gauche defects are observed in molecular images for *n*=18 SAMs.

Future work can involve studying the effects of chain lengths on friction, plus the effects of different organic chemistries on both adhesion and friction issues on MEMs.

7.3 Organic-Modified Ordered Mesoporous Materials

A molecular study of structural and surface properties of a silica material (MCM-41) modified via chemical bonding of organosilanes with a range of sizes (C4, C8 and C18) is presented. Model systems similar to experimental systems in the literature are studied. For simplicity, the pores of the MCM-41 inorganic materials are modeled as slit-shaped pores, instead of cylindrical pores. The grand canonical MC simulations are employed to obtain nitrogen adsorption isotherms for unmodified and modified MCM-41 material models. These adsorption isotherms are utilized for characterization of the materials. Furthermore, the density profiles of nitrogen and the organic layer (chains) are generated. The average pore size is estimated for each organic-modified OMMs, and compared with the experimental results.

The nitrogen adsorption technique is found to be very useful tool for characterization of the unmodified and organic-modified MCM-41 materials. Since the models are a geometrically simplified adaptation of the real systems (slit-shaped pore model), the adsorption isotherms are wider than the ones obtained in the experiments. However, they show similar trends, with the exception of very low-pressure adsorption

data. The disagreement between the simulation and experimental data for the low-pressure adsorptions is related to surface heterogeneity effects. The density profiles of alkyl chains and nitrogen molecules are analyzed to clarify the differences in the adsorption mechanisms in unmodified and modified materials. A systematic decrease in the pore diameter with the increase in size of bonded ligands is observed.

In future studies, the pore model can be improved to a cylindrical-shaped model, and the surface heterogeneity, pore size and surface density effects may be included. More attention should be given to low-pressure adsorption measurements. Enhanced models, including the surface heterogeneity, may be helpful for this purpose. In addition to monomeric-type organic ligands, polymeric-type ligands on OMMs surfaces can be investigated.

REFERENCES

(1) Javaid, A.; Hughey, M.P.; Varutbangkul, V.; Ford, D.M. *J. Membrane Sci.* **2001**, 187, 141.

(2) Randon, J.; and Paterson, R. *J. Membrane Sci.* **1997**, 134, 219.

(3) Moaddeb, M.; Koros, W.J. *J. Membrane Sci.* **1996**, 111, 283.

(4) Joseph, T.S.; Mountain, R.D. *J. Phys. Chem. B* **1999**, 103, 1354.

(5) Klatte, S.J.; Beck, T.L. **1996**, 100, 5931.

(6) Wheeler, J.F.; Beck, T.L.; Klatte, S.J.; Cole, L.A.; Dorsey, J.G. *J. Chromatography A* **1993**, 656, 317.

(7) Klatte, S.J.; Beck, T.L. *J. Phys. Chem.* **1993**, 97, 5727.

(8) Maboudian, R.; Ashurst, W.R.; Carraro, C. *Sensors and Actuators* **2000,** 82, 219.

(9) Maboudian, R.; Howe, R.T. *J. Vac. Sci. Technol. B* **1997,** 15(1), 1.

(10) Hornbeck, L., U.S. Patent Nos. 5,331,454 and 5,411,769, both continuances of Series No. 07/612,946 filed 13 November 1990.

(11) Antochshuk, V.; Jaroniec, M. Chem. Commun. **1999**, 2373.

(12) Jaroniec, C. P.; Kruk, M.; Jaroniec, M. *J. Phys. Chem. B* **1998,** 102, 5503.

(13) Kruk, M.; Jaroniec, M. *Chem. Mater.* **2001,** 13, 3169.

(14) Rouquerol, F.; Rouquerol, J.; Sing K. S. W. *Adsorption by Powders and Porous Solids;* Academic Press: London, 1999.

(15) Gregg, S.J.; Sing, K. S. W. *Adsorption, Surface Area and Porosity;* Academic Press: London, 1982.

(16) Kruk, M.; Antochshuk, V.; Jaroniec, M. *J. Phys. Chem. B* **1999,** 103, 10670.

(17) Jaroniec, M.; Kruk, M.; Jaroniec, C. P.; Sayari, A. *Adsorption* **1999,** 5, 39.

(18) Jaroniec, C. P.; Gilpin, R. K.; Jaroniec, M. *J. Phys. Chem. B* **1997,** 101, 6861.

(19) Kruk, M.; Jaroniec, M.; Gilpin, R. K.; Zhou, Y. W. *Langmuir* **1997,** 13, 545.

(20) Sander, L.C.; Callis, J.B.; Field, L.R. *Anal. Chem.* **1983,** 55(7), 1068.

(21) Zeigler, R.C.; Maciel, G.E.; *J. Am. Chem. Soc.* **1991,** 113(17), 6349.

(22) Montgomery, M.E.; Wirth, M.J. *Anal. Chem.* **1992,** 64(21), 2566.

(23) Clear, S.C.; Nealey, P.F. *J. Chem. Phys.* **2001**, 114(6), 2802.

(24) Brewer, N.J.; Beake, B.D.; Leggett, G.J. *Langmuir* **2001,** 17, 1970.

(25) Carlo, S.R.; Wagner, A.J.; Fairbrother, D.H. *J. Phys. Chem. B* **2000,** 104, 6633.

(26) Yamada, Y.; Yamada, T.; Tasaka, S.; Inagaki, N. *Macromolecules* **1996,** 29, 4331.

(27) Gabriel, K.J. *Sci. Am.* **1995,** 273(3), 150.

(28) Core, T.A.; Tsang, W.K.; Sherman, S.J. *Solid State Technol.* **1995**, 36(10), 39.

(29) Cagin, T.; Che, J.; Gardos, M.N.; Fijany, A.; Goddard W.A. *Nanotechnology* **1999,** 10, 278.

(30) Stevens, M.J. *Macromolecules* **2001,** 34, 2710.

(31) Stevens, M.J. *Macromolecules* **2001,** 34, 1411.

(32) Leng, Y.; Jiang, S. *J. Chem. Phys.* **2000,** 113(19), 8800.

(33) Hayashi, K.; Maeda, A.; Terayama, T.; Sakudo, N. *Computational Materials Sci.* **2000,** 17, 356.

(34) Stevens, M.J. *Langmuir* **1999,** 15, 2773.

(35) Sham, T.L.; Tichy, J. *Wear* **1997**, 207, 100.

(36) Depondt, P.; Ghazali, A.; Lévy, J.-C.S. *Surface Science* **1998,** 419, 29.

(37) Shimizu, J.; Eda, H.; Yoritsune, M.; Ohmura, E. *Nanotechnology* **1998,** 9, 118.

(38) Beck, J.S.; Vartuli, J. C.; Roth, W. J.; Leonowicz, M. E.; Kresge, C. T.; Schmitt, K. D.; Chu, C. T.-W.; Olson, D. H.; Sheppard, E. W.; McCullen, S. B.; Higgins, J. B.; Schlenker, J. L. *J. Am. Chem. Soc.* **1992,** 114, 10834.

(39) Macquarrie, D. J.; Jackson, D. B. *Chem. Commun.* **1997,** 1781.

(40) Liu, C.-J.; Li, S.-G.; Pang, W.-Q.; Che, C.-M. *Chem. Commun.* **1997,** 65.

(41) Koyano, K. A.; Tatsumi, T.; Tanaka, Y.; Nakata, S. *J. Phys. Chem. B* **1997,** 101, 9436.

(42) Liu, J.; Feng, X.; Fryxell, G. E.; Wang, L.-Q.; Kim, A. Y.; Gong, M. *Adv. Mater.* **1998,** 10 (2), 161.

(43) Feng, X.; Fryxell, G.E.; Wang, L.-Q; Kim, A. Y.; Liu, J.; Kemner, K.M. *Science* **1997,** 276, 923.

(44) Shevade, A. V.; Zhou, J.; Zin, M. T.; Jiang, S. *Langmuir* **2001,** 17, 7566.

(45) Kesting, R.E.; Fritzsche, A.K. *Polymeric Gas Separation Membranes*; John Wiley & Sons, Inc.: New York, 1993.

(46) Koros, W.J.; Fleming, G.K. *J. Membrane Sci.* **1993,** 83, 1.

(47) Stern, S.A., *J. Membrane Sci.* **1994,** 94, 1.

(48) Freeman, B.; Pinnau, I. *Trends in Polymer Science* **1997,** 5(5), 167.

(49) Baker, R.W.; Yoshioka, N.; Mohr, J.M.; Khan, A.J. *J. Membrane Sci.* **1987,** 31, 259.

(50) Schultz, J.; Peinemann, K.-V. *J. Membrane Sci.* **1996,** 110, 37.

(51) Rao, M.B.; Sircar, S. *J. Membrane Sci*. **1996,** 110, 109.

(52) Javaid, A.; Ford, D. M. *J. Membrane Sci.* **2003,** 215, 157.

(53) Javaid, A.; Krapchetov, D. A.; Ford, D. M. *J. Membrane Sci.* **2004,** submitted.

(54) Randon, J.; Blanc, P.; Paterson, R. *J. Membrane Sci.* **1995,** 98, 119.

(55) Leger, C.; Lira, H. D. L.; Paterson, R. *J. Membrane Sci.* **1996,** 120, 135.

(56) Leger, C.; Lira, H. D. L.; Paterson, R. *J. Membrane Sci.* **1996,** 120, 187.

(57) McCarley, K.C.; Way, J.D. *Separation and Purification Technology* **2001,** 25, 195.

(58) Miller, J.R.; Koros, W.J. *Sep. Sci Technol.* **1990,** 1257.

(59) Alami-Younssi, S.; Kiefer, C.; Larbot, A.; Persin, M.; Sarrazin, J. *J. Membrane Sci.* **1998,** 143, 27.

(60) Younssi, S.A.; Iraqi, M.; Persin, M.; Larbot, A.; Sarrazin, J. *Separation and Purification Technology* **2003,** 32, 175.

(61) Van Gestel, T.; Van der Bruggen, B.; Buekenhoudt, A.; Dotremont, C.; Luyten, J.; Vandecasteele, C.; Maes, G. *J. Membrane Sci.* **2003,** 224, 3.

(62) Dafinov, A.; Garcia-Valls, R.; Font, J. *J. Membrane Sci.* **2002,** 196, 69.

(63) Hulteen, J.C.; Jirage, K.B.; Martin, C.R. *J. Am. Chem. Soc.* **1998,** 120, 6603.

(64) Jirage, K.B.; Hulteen, J.C.; Martin, C.R. *Analy. Chem.* **1999,** 71, 4913.

(65) Lee, S.B.; Martin, C.R. *Chem. Mater.* **2001,** 13, 3236.

(66) Lee, S.B.; Mitchell, D.T.; Trofin, L.; Nevanen, T.K.; Soderlund, H.; Martin, C.R. *Science* **2002,** 2002, 2198.

(67) Castro, R.P.; Cohen, Y.; Monbouquette, H.G. *J. Membrane Sci.* **1993,** 84, 151.

(68) Liu, C.; Chen, W.J.; Martin, C.R. *J. Membrane Sci.* **1992,** 65, 113.

(69) Nagale, M.; Kim, B.Y.; Bruening, M.L. *J. Am. Chem. Soc.* **2000,** 122, 11670.

(70) Xiao, K.P.; Harris, J.J.; Park, A.; Martin, C.M.; Pradeep, V.; Bruening, M.L. *Langmuir* **2001,** 17, 8236.

(71) Liu, C.; Martin, C.R. *Nature* **1991,** 352, 50.

(72) Wang, H.; Tanaka, K.; Kita, H.; Okamoto, K. *J. Membrane Sci.* **1999,** 154, 221.

(73) Yamaguchi, T.; Suzuki, T.; Kai, T.; Nakao, S. *J. Membrane Sci.* **2001,** 194, 217.

(74) Yanagishita, H.; Kitamoto, D.; Ikegami T.; Negishi H.; Endo, A.; Haraya, K.; Nakane, T.; Hanai, N.; Arai, J.; Matsuda, H.; Idemoto, Y.; Koura, N. *J. Membrane Sci.* **2002,** 203, 191.

(75) Fowler, C.E.; Burkett, S.L.; Mann, S. *Chem. Commun.* **1997,** 1997, 1769.

(76) Macquarrie, D.J.; Jackson, D.B.; Mdoe, J.E.G.; Clark, J.H. *New J. Chem.* **1999,** 23, 539.

(77) Mercier, L.; Pinnavaia, T.J. *Adv. Mater.* **1997,** 9, 500.

(78) Peterson, B.K.; Gubbins. K.E.; Heffelfinger, G.S.; Marini Bettolo Marconi, U.; van Swol, F. *J. Chem., Phys.* **1988,** 88, 6487.

(79) Heffelfinger, G.S.; van Swol, F.; Gubbins, K.E. *Mol. Phys.* **1987,** 61, 1381.

(80) Jiang, S.; Rhykerd, C.L.; Gubbins, K.E. *Mol. Phys.* **1993,** 79(2), 373.

(81) Maddox, M.; Ulberg, D.; Gubbins, K.E. *Fluid Phase Equilibria* **1995,** 104, 145.

(82) Sandia National Laboratories; http://www.sandia.gov/mstc/technologies/micromachines/tech-info/index.html 1998.

(83) Mastrangelo, C.H. *Tribol. Lett.* **1997,** 3, 223.

(84) Tas, N.; Sonnenberg, T.; Jansen, H.; Legtenberg, R.; Elwenspoek, M. *J. Micromech. Microeng.* **1996,** 6, 385.

(85) Rymuza, Z. *Microsystem Technologies* **1999,** 5, 173.

(86) Maboudian, R. *Surf. Sci. Rep.* **1998,** 30, 209.

(87) Maboudian, R.; Howe, R.T. *Tribol. Lett.* **1997,** 3, 215.

(88) Lio, A.; Charych, D.H.; Salmeron, M. *J. Phys. Chem. B* **1997,** 101, 3800.

(89) Unger, K.K. *Packing and Stationary Phases in Chromatographic Techniques;* Marcel Dekker: New York, 1990.

(90) Kruk, M.; Jaroniec, M.; Sayari, A. *Langmuir* **1997,** 13, 6267.

(91) Kruk, M.; Jaroniec, M.; Sakamoto, Y.; Terasaki, O.; Ryoo, R.; Chang, H.K. *J. Phys. Chem. B* **2000,** 104, 292.

(92) Kruk, M.; Jaroniec, M.; Sayari, A. *J. Phys. Chem. B* **1997,** 101, 583.

(93) Sing, K. *Colloids Surf. A: Phys. Eng. Asp.* **2001,** 187-188, 3.

(94) Barton, T.J.; Bull, L.M.; Klemperer, W.G.; Loy, D.A.; McEnaney, B.; Misono, M.; Monson, P.A.; Pez, G.; Scherer, G.W.; Vartuli, J.C.; Yaghi, O.M. *Chem. Mater.* **1999,** 11, 2633.

(95) Gelb, L.D.; Gubbins, K.E.; Radhakrishnan, R.; Sliwinska-Bartkowiak, M. *Rep. Prog. Phys.* **1999,** 62, 1573.

(96) Balbuena, P.B.; Gubbins, K.E. *Fluid Phase Equilibria* **1992,** 76, 21.

(97) Evans, R.; Marconi, U.M.B. *J. Chem. Phys.* **1986,** 84 (4), 2376.

(98) Bereznitski, Y.; Jaroniec, M.; Kruk, M.; Buszewski, B. *J. Liquid Chromatogr.* **1996,** 19, 2767.

(99) Allen, M.P.; Tildesley, D.J. *Computer Simulation of Liquids*; Clarendon Press: Oxford, 1987.

(100) Mcquarrie, D.A. *Statistical Mechanics;* Harper Collins Publishers: New York, 1976.

(101) Hill, T.L. *An Introduction to Statistical Thermodynamics;* Dover Publications: New York, 1986.

(102) Deem, M.W. *AICHE Journal* **1998,** 44(12), 2569.

(103) Cao, D.; Shen, Z.; Chen, J.; Zhang, X. *Microp. Mesop. Mater.* **2004,** 67, 159.

(104) Maddox, M.W.; Gubbins, K.E. *Int. J. Thermophys.* **1994,** 15 (6), 1115.

(105) Maddox, M.W.; Oliver, J.P.; Gubbins K.E. *Langmuir* **1997,** 13, 1737.

(106) Ravikovitch, P.I.; Vishnyakov, A.; Neimark, A.V. *Phys. Rev. E* **2001,** 64, 011602.

(107) Plimpton, S. *J. Comp. Phys.* **1995,** 117, 1.

(108) Frenkel, D.; Smit B. *Understanding Molecular Simulation;* Academic Press: San Diego, 1996.

(109) Deem, M.W. *AICHE Journal* **1998,** 44 (12), 2569.

(110) Panagiotopoulos, A.Z. *Fluid Phase Equilib.* **1996,** 116, 257.

(111) Wick, C.D.; Siepmann, J.I. *Macromolecules* **2000,** 33, 7207.

(112) Rosenbluth, M.N.; Rosenbluth, A.W. *J. Chem. Phys.* **1955,** 23, 356.

(113) Martin, M.G.; Siepmann, J.I. *J. Phys. Chem. B* **1999,** 103, 4508.

(114) Flory, P.J. *Macromolecules* **1974,** 7(3), 381.

(115) Theodorou, D.N.; Suter, U.W. *Macromolecules* **1985,** 18, 1467.

(116) Muller-Plathe, F. *Acta Polymer* **1994,** 45, 259.

(117) Widom, B. *J. Chem. Phys.* **1963,** 39, 2808.

(118) van der Vegt, N.F.A.; Briels, W.J. *J. Chem. Phys.* **1996,** 105(19), 8849.

(119) Steele, W.A. *Surface Sci.* **1973,** 36, 317.

(120) Gallaher, G.R., Liu P.K.T. *J. Membrane Sci.* **1994,** 92, 29.

(121) Krishna Pant, P.V.; Boyd, R.H. *Macromolecules* **1991,** 24, 6325.

(122) Krishna Pant, P.V.; Boyd, R.H. *Macromolecules* **1993,** 26, 679.

(123) Dorsey, J.G.; Dill, K.A. *Chem. Rev.* **1989,** 331.

(124) Svehla, R.A. *NASA Tech. Rep.* **1962,** R-132.

(125) Travis, K.P.; Gubbins, K.E. *Langmuir* **1999,** 15, 6050.

(126) Kärger, J.; Ruthven, D.M. *Diffusion in Zeolites;* John Wiley & Sons: New York, 1992.

(127) Stern, S.A.; Shah, V.M.; Hardy, B.J. *J. Polym. Sci.:Part B: Polym. Phys.* **1987,** 25, 1263.

(128) Maboudian, R.; Ashurst W.R.; Carraro, C. *Tribol. Lett.* **2002,** 12, 95.

(129) Lio, A.; Morant, C.; Ogletree, D.F.; Salmeron, M. *J. Phys. Chem. B* **1997,** 101, 4767.

(130) Srinivasan, U.; Houston M.R.; Howe, R.T.; Maboudian, R. *J. Microelectromech. Sys.* **1998,** 7(2), 252.

(131) Sun, H.; Rigby, D. *Spectrochimica Acta Part A* **1997,** 53, 1301.

(132) Sun, H. *Macromolecules* **1995,** 28, 701.

(133) Tuckerman, M.; Berne, B.J.; Martyna, G.J. *J. Chem. Phys.* **1992,** 97, 1990.

(134) Burns, A.R.; Houston, J.E.; Carpick, R.W.; Michalske, T.A. *Langmuir* **1999,** 15, 2922.

(135) Chandross, M.; Grest, G.S.; Stevens, M.J. *Langmuir* **2002,** 18, 8392.

(136) Evans, R.; Marini Bettolo Marconi, U.; Tarazona, P.J. *Chem. Soc., Faraday Trans. 2* **1986,** 82, 1763.

(137) Ravikovitch, P.I.; Wei, D.; Chueh, W.T.; Haller, G.L.; Neimark, A.V. *J. Phys. Chem. B* **1997,** 101, 3671.

(138) Gelb, L.D.; Gubbins, K.E. *Mol. Phys.* **1999,** 96(12), 1795.

(139) Johnson, J.K.; Zollweg J.A.; Gubbins, K.E. *Mol. Phys.* **1993,** 78(3), 591.

(140) Vishnyakov, A.; Debenedetti, P.G.; Neimark, A.V. *Phys. Rev. E* **2000,** 62(1), 538.

(141) Barrett, E.P.; Joyner, L.G.; Halenda, P.P. *J. Am. Chem. Soc.* **1951,** 73, 373.

APPENDIX A

- Movie 4.1

  It shows the simulation of nitrogen molecules in C18-modified (4 μmol/m^2), 5 nm model membranes.

- Movie 4.2

  It shows the simulation of nitrogen molecules in C18-modified (4 μmol/m^2), 3 nm model membranes.

- Movie 6.1

  It shows the simulation of the adsorption of nitrogen in unmodified mesoporous model materials (MCM-41, 5 nm) at various relative pressures (from P/P_{sat}=1E-002 to P/P_{sat}=0.96).

- Movie 6.2.a

  It shows the simulation of the adsorption of nitrogen in C18-modified mesoporous model materials (5 nm) at various relative pressures (from P/P_{sat}=0.01572 to P/P_{sat}=1.0).

- Movie 6.2.b

  It shows the simulation of the same adsorption process of nitrogen in C18-modified mesoporous model materials (5 nm) at various relative pressures (from P/P_{sat}=0.01572 to P/P_{sat}=1.0) as in Movie 6.2.a. However, the visualization of the C18 chains is faded to make the location of the adsorbed nitrogen molecules more clear.

VITA

Turkan Aydogmus was born in Istanbul, Turkey, on 25 November 1971. She received her BS. degree in chemical engineering from Gazi University, in Ankara Turkey in July 1993.

She can be reached through Dr. David M. Ford, at

Department of Chemical Engineering

Texas A&M University

3122 TAMU

College Station, Texas, 77843-3122, USA